Topological insulator nanowires: growth, characterization and superconducting proximity effect

Inaugural-Dissertation

zur Erlangung des Doktorgrades
der Mathematisch-Naturwissenschaftlichen Fakultät
der Universität zu Köln

vorgelegt von

Felix Münning

aus Bonn

Köln, 2024

Diese Arbeit stellt eine von der
Mathematisch-Naturwissenschaftlichen Fakultät
der Universität zu Köln
angenommene Dissertation dar.

Abstract

Topological Insulator (TI) nanowires have attracted attention in recent years, not only because of the novel physics that are to be discovered in such systems, but also because they are a possible platform to realize Majorana fermions and topological quantum computation.

In this thesis, electronic transport in TI nanowires is investigated. Bulk-insulating nanowires are grown by the vapor-liquid-solid method from the ternary topological insulators $(Bi_{1-x}Sb_x)_2Te_3$ and $Bi_2(Te_xSe_{1-x})_3$. At cryogenic temperatures, the particular properties of their quantum-confined topological surface states are studied through electrostatic gating, which gives rise to characteristic restiance oscillations originating from their quantized sub-band structure. In magnetic fields, Aharonov-Bohm-like oscillations are measured, and their peculiar π-shift is observed.

Furthermore, superconductivity is induced by the proximity effect from Nb and V (in the structure TiVTiAl) in nanowire Josesephson junction devices. The proximitization is characterized and interplay with the topological surface states

is investigated. First attempts at tunneling spectroscopy on the proximitized TI nanowires are made.

Kurzzusammenfassung

Topological Insulator (TI) Nanodrähte haben in den letzten Jahren Aufmerksamkeit erregt, nicht nur wegen der neuartigen Physikalischen Phänomene, die kontinuierlich in diesen Systemen entdeckt werden, sondern auch, weil sie eine vielversprechende Plattform zur Realisierung von Majorana-Fermionen und topologischem Quanten-Computing darstellen.

In dieser Arbeit werden elektronische Transportphänomene in TI-Nanodrähten untersucht. Nanodrähte, die im inneren isolierend sind, werden mit der Vapor-Liquid-Solid-Methode aus den topologischen Isolatoren $(Bi_{1-x}Sb_x)_2Te_3$ und $Bi_2(Te_xSe_{1-x})_3$ gezüchtet. Bei kryogenen Temperaturen werden die besonderen Eigenschaften ihrer drehimpulszahlquantisierten topologischen Oberflächenzustände über den elektrostatischen Feldeffekt untersucht, was zu charakteristischen Widerstandsschwankungen führt, die aus ihrer quantisierten Subbandstruktur hervorgehen. In Magnetfeldern werden Aharonov-Bohm-verwandte Oszillationen gemessen und deren einzigartige π-Verschiebung beobachtet.

Des weiteren wird Supraleitung über den Proximity-Effekt von Nb und V (in

der Aufschichtung TiVTiAl) in lithografischen devices mit Nanodraht-Josephson-Kontakten induziert. Die Proximitisierung wird charakterisiert und das Zusammenspiel mit den topologischen Oberflächenzuständen untersucht. Es werden erste Versuche zur Tunnelspektroskopie an den proximitierten TI-Nanodrähten unternommen.

CONTENTS

CONTENTS

1

INTRODUCTION

Superconducting topological insulator and semiconductor nanowires have been a hot topic in recent years. In the constantly progressing back-and-forth between novel experiments and theory, important motors have been the rise of the field of quantum computing and the prospect of realizing Majorana fermions in these platforms [3–9]. Despite being the younger, less common and theoretically more complex platform of the two, TI nanowires may have key advantages for some of these applications [10].

At first, we knew only insulators and metals. Whether the filled valence band was separated from the empty conduction band, or they did overlap such that electrons could move freely, was the understanding of what determines whether or not matter could conduct electricity. Then, semiconductors came onto the stage, having a smaller band-gap and demonstrating, that with enough energy, the insulating gap could be overcome, for example nowadays, billions of times per second, in almost everyone's pocket.

But billions of times per second in almost everyone's pocket is not enough.

Obviously. The most complex computational tasks that science has come up with are practically unsolvable on classical computers, even on the super ones. And on the other side of the problem, we are approaching the end of Moore's law [11, 12]. Soon, the cirquits within our computers cannot be made smaller and smaller anymore. Quantum computers are the new hope for advancing in a world-changing manner in a number of fields, such as cryptography, drug design, materials science, protein folding, weather prediction, to name only a few [13]. Although sometimes considered a niche field, TI nanowires participate in the race to be the platform to make that happen [14, 15].

Topological insulators are a class of materials that harbor exotic electronic states on the surface, which are their main feature of interest. They originate from the topologically non-trivial band-gap of the bulk and are required to exist because it needs to be closed at the interface to ordinary insulators, in order to be transformed into a trivial gap. This necessity, and their special properties, protection from back-scattering, spin-momentum-locking and an almost linear dispersion makes them a unique platform for a broad spectrum of research topics and potential applications [4].

TI nanowires (TINW) are thin, rod-shaped microcrystals, with diameters of several tens of nanometers. They can be crafted or grown by a variety of methods [16], and are especially fragile experimental endeavors for nanofabrication. There have been many experimental advances in recent years across several fabricational concepts to make TI nanowires, among these are the etching or constriction of thin-films grown by molecular-beam epitaxy or exfoliated crystals [17–20], selective area growth [21–24] and by the vapor-liquid-solid growth process [25–29].

Superconductivity is one of the most fascinating states of matter, which is being continuously explored since its discovery over a century ago [30, 31]. What was initially about the complete disappearance of electrical resistance and expulsion of magnetic fields, is nowadays still puzzling scientists in much more complex ways. It can be induced into materials that are not superconducting by themselves by the proximity effect [32], which is one way to obtain toplogical superconduc-

tivity, for example, in topological insulators [17, 18, 20, 23, 33–38]. Such systems have attracted huge attention in the last decades because of the prospects to realize Majorana fermions. This elusive particle, which is its own antiparticle and therefore interesting per se, may arrise as exotic quasiparticle excitation in solid state systems, which is useful for topological quantum computation [39].

In this thesis, bulk-insulating TI nanowires are grown out of the TIs $(Bi_{1-x}Sb_x)_2Te_3$ and $Bi_2(Te_xSe_{1-x})_3$ by the vapor-liquid-solid (VLS) method, in which free-standing naowires are synthesized from evaporated source materials through liquid gold nanoparticles as catalysts. This is done in two kinds of two-zone tube-furnaces and three reproducible recipes are specifically provided. Lithographic devices are fabricated via electron-beam lithography, and electronic transport is studied at cryogenic temperatures.

In $(Bi_{1-x}Sb_x)_2Te_3$ nanowires, characteristic signatures of the quantum-confined topological surface states are measured upon changing the chemical potential through electrostatic gating, and their dependence on the density of states as well as on scattering are investigated in a collaborative publication [1].

Furthermore, superconductivity is induced in $(Bi_{1-x}Sb_x)_2Te_3$ nanowires by the superconductors niobium and vanadium, and the proximity effect is studied in Josephson junctions, as well as first attempts at resolving the density of states in tunneling spectroscopy are made.

This thesis is structured as follows. Chapter 2 conveys the theoretical concepts, that are required to understand the underlying physics of this work and the experimental data presented, addressing topological insulators and nanowires, their particular transport features, the superconducting proximity effect and Josephson junctions. Experimental methods and equipment are described in Chapter 3, including the growth characterization, lithographic fabrication and cryogenic transport measurements.

In Chapter 4, the nanowire growth is presented by explaining the VLS method, introducing the TI materials, reporting on technical parameters and the resulting outcome for $(Bi_{1-x}Sb_x)_2Te_3$ and $Bi_2(Te_xSe_{1-x})_3$ nanowires. Next, electronic transport of $(Bi_{1-x}Sb_x)_2Te_3$ nanowires in the normal state is shown in

Chapter 5, which consists of the publication *Quantum confinement of the Dirac surface states in topological-insulator nanowires* [1], treating characteristic resitance oscillations of the TSS in gating experiments.

In Chapter 6, measurement results on proximitized $(Bi_{1-x}Sb_x)_2Te_3$ nanowires with Nb and V (TiVTiAl) Josephson junctions are presented. Finally, first attempts at resolving the density of states in close to the superconducting Nb leads in proximitized $(Bi_{1-x}Sb_x)_2Te_3$ nanowires are shown. Chapter 7 summarizes this work and the conclusions as well as the open questions and promising follow-up experiments are discussed.

2

THEORETICAL BACKGROUND

In this chapter, the theoretical concepts required to understand the physics employed and investigated in this work are explained. The following sections are based on a number of publications ranging from review papers to experimental and theoretical reports [4, 6, 14, 16, 17, 19, 40–44].

2.1 TOPOLOGICAL INSULATORS

Topological insulators (TIs) are a class of material with unique electronic properties on their surface. Similar to ordinary insulators, they have an insulating band gap, which, however, is opened in a topologically non-trivial way. At the interface to an ordinary insulator, this gap cannot be smoothly transformed into a trivial one without being closed in between. This situation can be illustrated by one of the typical examples of topology, the branch of mathematics that classifies geometrical objects by their possibility to be smoothly transformed into each other. The Möbius strip cannot be smoothly transformed into a normally wound loop of

a ribbon, without being cut, untwisted and reconnected anew[42, 45, 46].
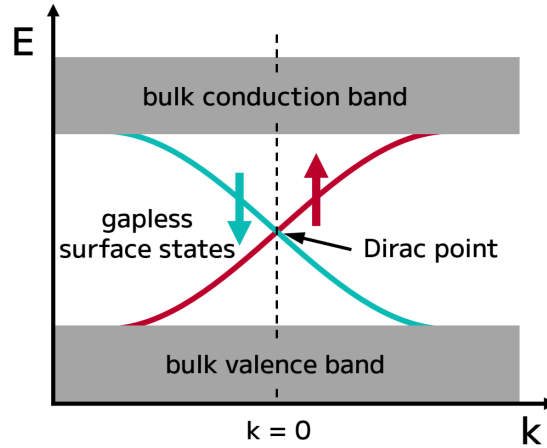
Figure 2.1: **Topological insulator band gap and surface states.** *The insulating band gap in TIs is opened in a topologically non-trivial way and must be closed at the surface in order to be transformed into a trivial gap. This gives rise to the gapless surface states with spin-momentum locking that are protected by time-reversal symmetry. Adapted from [4].*

This necessary transitory closing of the insulating band gap occurs at the boundary of TIs to trivial insulators, including vacuum, which is called bulk-boundary correspondence, and hence requires the formation of the surface states. They have an approximately linear dispersion, letting them behave like Dirac fermions, and back-scattering is suppressed. Furthermore, strong spin-orbit coupling locks the spin of these electrons parallel to the surface and perpendicular to their direction of motion.

On flat surfaces of three-dimensional TIs, these properties give rise to spin-polarized Dirac cones, as illustrated in Figure 2.2, left. On the surface of one-dimensional TI nanowires, these cones are sliced by size-quantization into doubly degenerate sub-bands of opposite spin, Figure 2.2, right.

2.2 TOPOLOGICAL INSULATOR NANOWIRES

Nanowires are thin rods of a material, ideally straight with a constant cross-section and diameters below 100 nm. In TI nanowires, the resulting circumference is what introduces important changes to the electronic states on the surface. Namely, with a small enough circumference, the circular direction of motion of the topological surface states around the nanowire becomes quantized. This hollow cylindrical shell of metallic states wrapped around the insulating bulk now consists of discrete bands instead of a continously wound Dirac cone on the two-dimensional surface of bulk 3D TIs.

bulk 3D TI surface (2D)   TI nanowire shell (1D)
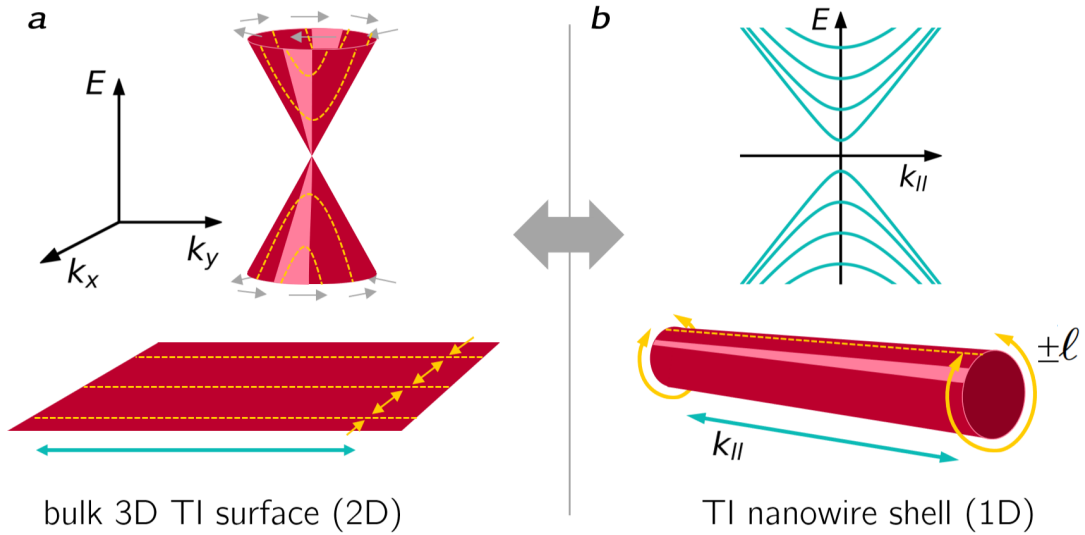
Figure 2.2: **Surface state sub-band spectrum of a TI nanowire in comparison to the Dirac cone of a two-dimensional TI surface.** *On an infinite two-dimensional surface of a TI, both momenta k_x and k_y are free and the gapless surface state forms a hourglass-like double cone due to the rotational symmetry. In the case of a TI nanowire, the small circumference causes the perpendicular direction (here k_x) to be quantized as angular momentum ℓ (Equation 2.1). The emerging discrete sub-band spectrum can be retraced by visualizing linecuts of the 2D Dirac cone at discrete values of k_y. The spectrum takes half-integer values due to the Berry phase arising from wrapping spin-momentum locked surface states around a cylinder.*

2.2.1 Topological surface states

In TI nanowires, the circular direction of motion $k_\perp$ of the topological surface states (TSS) around the cylinder mantle becomes quantized in angular momentum. The yellow dashed lines in Figure 2.2a illustrate the confinement of one direction (here x) from wrapping the two-dimensional surface around a cylinder. The resulting confinement in terms of angular momentum quantum number ℓ with respect to the nanowire circumference leads to the TSS sub-band spectrum

$$E_\ell(k_\parallel) = \pm \hbar v_\mathrm{F} |k| = \pm \hbar v_\mathrm{F} \sqrt{k_\parallel^2 + \left(\frac{\ell}{R_{nw}}\right)^2} \tag{2.1}$$

with nanowire R_nw and Fermi velocity v_F. Due to the linear dispersion of the gapless surface state prior to quantization, the subband bottoms occurring at $k_\parallel = 0$ are equally spaced in energy. The angular momentum quantum number ℓ takes half-integer values $\pm\frac{1}{2}, \pm\frac{3}{2}, \frac{5}{2}, \ldots$ due to the Berry phase arising from spin-momentum locking of the electrons confined to the cylindric surface wrapped around the nanowire by 2π. It is important to note, that this causes the famous gapless mode to disappear, and the subband spectrum is gapped at $E = 0$. Using the line cut at $k_\parallel = 0$ as a reference, at half integer values of their spacing $\Delta E = \hbar v_\mathrm{F}/R_\mathrm{w}$ two spin-non-degenerate subbands with opposite angular momenta lie exactly on top of each other. This degeneracy can be lifted, and also the gapless mode can be recovered with a magnetic field parallel to the nanowire axis, which is shown in Figure 2.3.

2.2.2 Magnetic field and AB-Like oscillations

When a magnetic field is applied along the nanowire axis, an effect similar to the Aharonov-Bohm (AB) effect [47, 48] comes into play. The surface electrons encircling the magnetic flux that pierces the nanowire cross-section acquire a phase. This lifts the degeneracy of the energetically coinciding spin-non-degenerate subbands of opposite angular momenta, and shifts them past each other, see Figure 2.3. The magnetic flux **B** through the cross-sectional area **A** of the nanowire
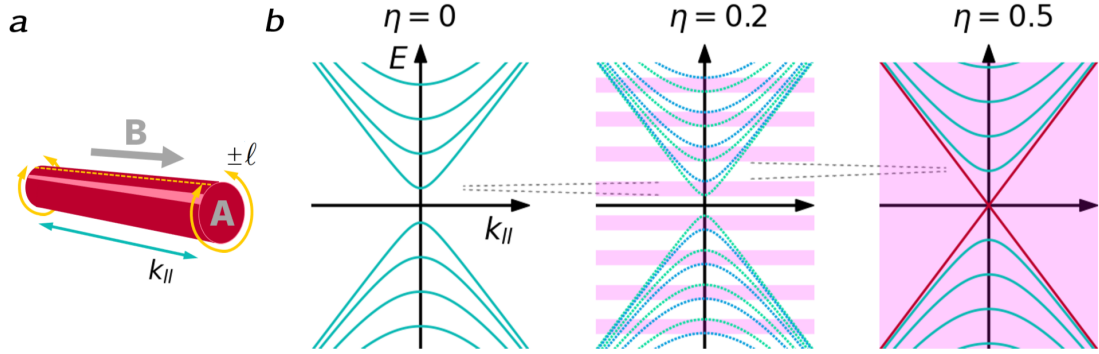
Figure 2.3: **Surface state sub-band spectrum of a TI nanowire in the presence of a longitudinal magnetic field. a** *Schematic of a TI nanowire in a magnetic field parallel to its axis. The surface state sub-bands couple to the magnetic field through their angular momentum $\pm\ell$.* **b** *Sub-band spectrum of the topological surface states, quantized in angular momentum $\pm\ell$ (Equation 2.2). Spin-degenerate sub-bands (solid lines, left) with positive and negative angular momenta acquire opposite phases in the magnetic field and are shifted apart (dashed lines, middle), shifting illustrated by grey dashed lines. When the magnetic flux through the nanowire cross-section amounts to half a flux quantum $\Phi_0 = hc/e$ (right), each single sub-band is shifted by half of their energy spacing at $k_\parallel = 0$. As a result, formerly adjacent sub-bands coincide and the gapless linear mode (red) is recovered. If the chemical potential is located inside the areas highlighted in pink, the number of Fermi points is odd and Majorana fermions are predicted to exist at the ends of the nanowire [3].*

$\Phi = \mathbf{B} \cdot \mathbf{A}$ inserted into the sub-band spectrum (Equation 2.1) yields

$$E_\ell(k_\parallel, \eta) = \pm\hbar v_\mathrm{F}\sqrt{k_\parallel^2 + \left(\frac{\ell - \eta}{R_\mathrm{nw}}\right)^2}, \quad \eta \equiv \Phi/\Phi_0. \tag{2.2}$$

When the magnetic flux through the nanowire cross-section amounts to multiples of half the flux quantum $\Phi_0/2 = hc/2e$, formerly adjacent subbands coincide and become degenerate again. However, a crucial difference occurs between integer multiples (1x, 2x, 3x, ...) and half integer multiples (0.5x, 1.5x, 2.5x, ...) of the flux quantum. In the former case, the original spectrum is restored. In the latter case, the gapless mode is recovered, and since all other subbands are degenerate again, there is an odd number of Fermi points — the number of sin-

gle bands crossing the Fermi energy — throughout the entire bulk band gap, as depicted in the rightmost spectrum in Figure 2.3. Between these two extreme scenarios, at intermediate fields, a stripe pattern of tunable width exists, hosting regions of odd and even number of fermi points, which is illustrated by the regions highlighted in green in Figure 2.3. Their importance becomes clear, when the superconducting proximity effect is taken into account. Within regions with an odd number of Fermi points, unpaired Majorana fermions are predicted to exist at the ends of the superconducting region or the nanowire (more to that in Section 2.3.4).
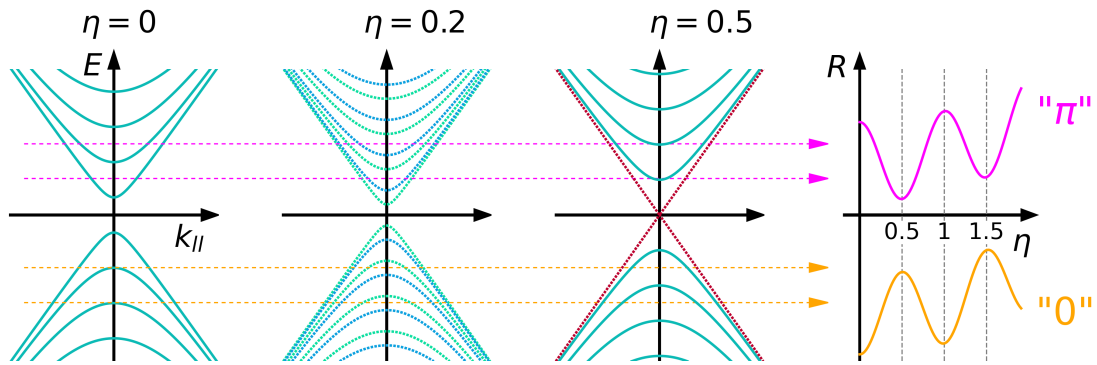
Figure 2.4: **AB-like oscillations.** *If the chemical potential lies between two sub-band bottom edges (magenta dashed lines), "π"-ABLO occur. Turning on the magnetic field shifts sub-bands from above and below towards it, reducing the resistance until $\Phi = 0.5\Phi_0$. At further increase, the same bands are shifted past the chemical potential and the resistance increases again, until $\Phi = \Phi_0$. The opposite "0"-ABLO occur, if the chemical potential matches a sub-band bottom-edge. Both types occur equally above and below the Dirac point, which was omitted for clarity.*

When sweeping the magnetic field over a range of multiple Φ_0 and the chemical potential is kept constant, the periodic pattern of sub-band shifting causes magnetoresistance oscillations, the so-called AB-like oscillations (ABLO). Depending on the precise location of the chemical potential with respect to the repetitive sub-band pattern, two distinct prototypical oscillations occur. The so-called 0-ABLO resemble the traditional Aharonov-Bohm effect and start with an

increase of resistance between $\Phi = 0$ and $\Phi = 0.5\Phi_0$, after which the resistance decreases again, until $\Phi = \Phi_0$, and so forth. This behavior is most pronounced if the chemical potential coincides with a sub-band bottom-edge energy. The opposite phase, the so-called π-ABLO occur when the chemical potential lies between two sub-band bottom-edges.

The counterintuitive peculiarity of π-ABLO is the occurrence of a resistive minimum at a flux of $\Phi = 0.5\Phi_0$, which is contrary to the usual Aharonov-Bohm effect picture. This, and the fact that π- and 0-ABLO can be measured in alternation when setting the chemical potential to the respective locations, are unique signatures of the surface state sub-bands in TI nanowires.

Another type of oscillation that can be observed in the nanowire resistance from interference effects of the TSS in magnetic field are the Altshuler-Aronov-Spivak (AAS) oscillations. They emerge from the quantum interference of two paths in both directions around a ring that encloses a magnetic field. That is, two complete circles, as in an interference at the original location of departure, e.g. from backscattering. Thus, the periodicity of AAS oscillations in magnetic flux through the ring is $h/2e$, half the periodicity of AB oscillations, which can in turn be visualized by the interference of two paths on the other side of the ring, thus, two half circles.

Both types of oscillations, AB and AAS can be observed in metal rings smaller than the phase coherence length, and equally in TI nanowires, in the magnetoresistance oscillations of the TSS in longitudinal magnetic field [17, 22, 24, 27, 29, 49–53].

The last magnetoresistance contribution that should be mentioned here is weak antilocalization. The π Berry phase causes time-reversed paths to interfere destructively, which enhances conductivity. This anti-localisation can be lifted with magnetic fields, adding a phase to such closed electron paths, disabling the destructive interference and causing a positive magnetoresistance [46, 54, 55]. At low magnetic fields, this causes the resistivity to increase with field, resulting in a significant dip around zero field in many TI nanowire magnetoresistance measurements [24, 56, 57].

2.2.3 EXPERIMENTAL SETTING

The presented phenomena are key characteristics of electronic transport in TI nanowires. To convey a practical picture, the orders of magnitude are briefly addressed in this section. Figure 2.5 shows the expected sub-band spacing energy at $k_{\parallel} = 0$ and magnetic field periodicity of AB-like oscillations in dependence of nanowire diameter. The estimation is calculated for $(Bi_{1-x}Sb_x)_2Te_3$ nanowires assuming a Fermi velocity of $v_F = 4.4 \times 10^5$ m/s [58] and a circular cross-section.

a   **b**
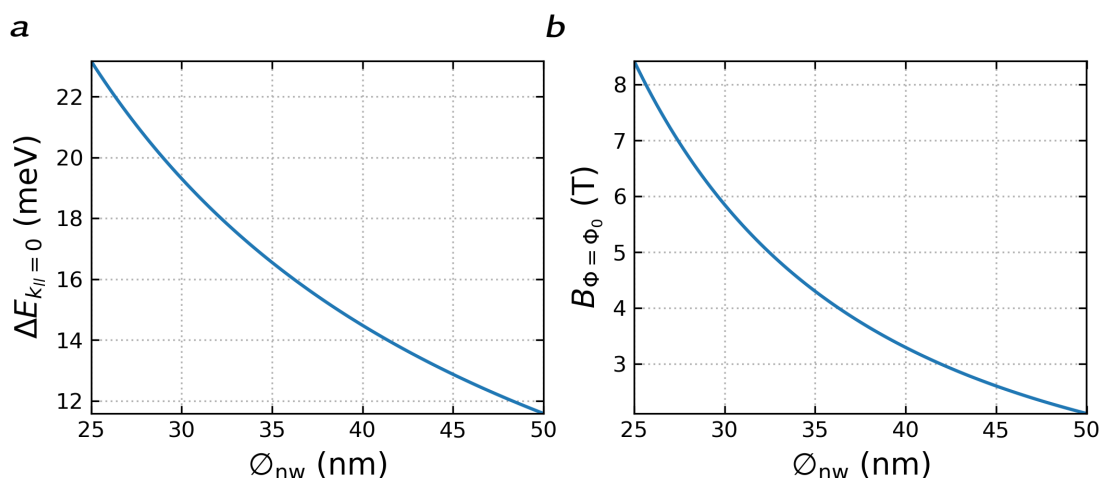
Figure 2.5: **Energy and magnetic field scales for $(Bi_{1-x}Sb_x)_2Te_3$ nanowires.** *a Approximate energy spacing of the sub-band bottom edges (at $k_{\parallel} = 0$) and b magnetic field periodicity of AB-like oscillations, in dependence of nanowire diameter, assuming a circular cross-section and $v_F = 4.4 \times 10^5$ m/s [58].*

It must be noted that the sub-bands do not appear linearly spaced in a measurement of resistance versus gate voltage. The required voltage for injecting (or withdrawing) charge carriers can be calculated as $V = Q/C_G + \mu/e$, with C_G the geometric (galvanic) capacitance and μ the chemical potential. In devices fabricated with a gate dielectric as thick as 300 nm (see Chapter 3.2), the bottleneck for injecting charge carriers is the geometric capacitance, being much smaller than the quantum capacitance of the sub-band structure. Thus, the expense of charging the nanowire is mainly the voltage $V = Q/C_G$, and since each sub-band, counting from the dirac point, hosts linearly more charge carriers, the sub-band bottom-edges appear quadratically spaced in gate voltage.

2.3 PROXIMITY-INDUCED SUPERCONDUCTIVITY IN TINW

Superconductivity is one of the most intriguing phenomena of quantum physics. Since its discovery in 1911 by Heike Kamerlingh-Onnes [59], it was an unexplained mystery for almost half a century. Its vanishing resistance allowing dissipationless currents that can perpetuate in closed superconducting circles, and the expulsion of magnetic fields from the inside of superconducting metals, the Meissner effect discovered in 1933 [60], were well known but poorly understood. In 1957, John Bardeen, Leon Neil Cooper and John Robert Schrieffer published their *Microscopic Theory of Superconductivity* [61], nowadays usually referred to as BCS theory, and could finally fill in the blanks between the macroscopic observations and the microscopic understanding of quantum physics.

The following sections are intended to convey a basic understanding of superconductivity, followed by the superconducting proximity effect in general and in the special case of TI nanowires.

2.3.1 SUPERCONDUCTIVITY

Electrons traveling through the positively charged lattice of a conductor create phonons, i.e. lattice vibrations, through which an attractive contribution of interaction with other electrons can arise. At very low temperatures, the resulting energies may exceed both the energetic difference of the electrons as well as the screened Coulomb repulsion. Electrons become correlated and the formation of a common superconducting phase is energetically favorable. Electrons pair up as Cooper pairs, which are in the same ground state and – in the absence of magnetic field – can now be described by the wavefunction

$$\Psi = n_{\mathrm{s}} e^{i\phi}, \tag{2.3}$$

with n_{s} the cooper pair density and ϕ the macroscopic superconducting phase, normalization omitted.

The energy gained through the pairing mechanism results in a forbidden energy gap around the Fermi energy, because Cooper pairs can only be split up
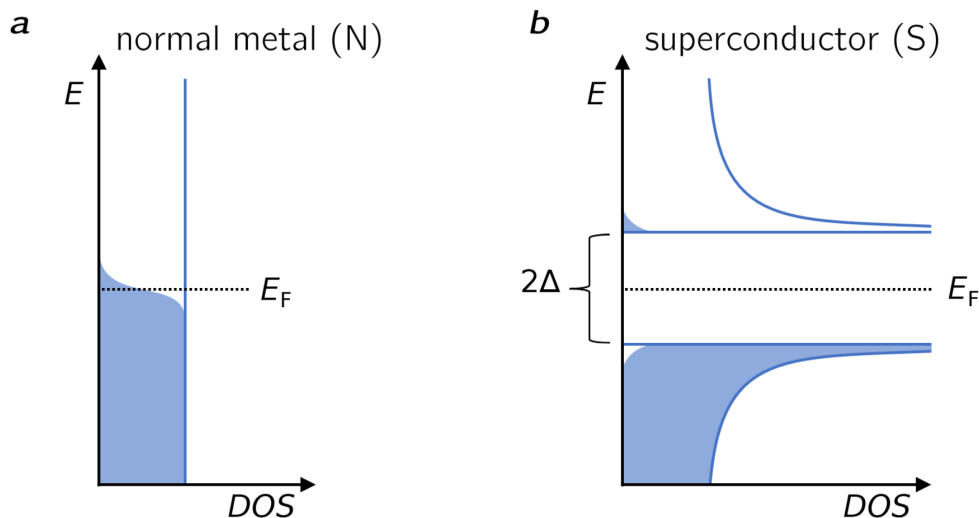
Figure 2.6: **Density of states in metal and superconductor. a** *In a normal metal, the density of states around Fermi energy E_F is assumed as constant, and the states are filled up to that level according to the Fermi-Dirac distribution.* **b** *In the superconducting state, electrons pair up as Cooper pairs with an energy of Δ. Thus, all electronic states within an energy band of 2Δ around E_F are displaced and accumulated above and below this gap, which is the energy it would cost to separate a Cooper pair.*

by excitations with higher amounts of energy (see Figure 2.6). Hence, small disturbances and excitations with energies below the pairing potential are forbidden, and supercurrent flows without any resistance.

In the simplest case of the so-called s-wave superconductivity, the lowest-energy state of a Cooper pair consists of electrons with zero net momentum and a singlet spin function $(\vec{k}\uparrow, -\vec{k}\downarrow)$, allowing for a relative angular momentum of zero [62]. Under special conditions, more peculiar types of pairing are possible, such as p-wave superconductivity, where electrons pair with parallel spins, which is a crucial ingredient for the realization of Majorana fermions in TI nanowires.

In the absence of magnetic fields, the transition between the normal to the superconducting state occurs at a material-specific temperature, which in practice may change drastically depending on the precise properties of a deposited metal film. BCS theory provides a relation between this temperature T_c and the

magnitude of the superconducting energy gap at zero temperature and magnetic field $\Delta(0)$

$$\Delta(0) = 1.76 k_B T_c, \tag{2.4}$$

which can be used to estimate the superconducting energy gap in an experimental setting based on the measured transition temperature.

2.3.2   SUPERCONDUCTIVITY IN MAGNETIC FIELD

Superconductors repel magnetic fields, which is called the Meissner effect. When a superconductor is exposed to a magnetic field, compensating supercurrents form, such that within the superconductor the net field is zero. These supercurrents are located close to the surface of the superconductor, which allows for a small but finite penetration depth of the magnetic field. This property is described by the London penetration depth $\lambda_{\mathrm{London}}$ as the length scale of an exponential decay into the superconducting material. This parameter depends on the superconductor, the temperature, as well as on the physical properties of a superconducting film, such as its thickness.

   With increasing magnetic field, two distinct behaviors within the Meissner effect arise. Type I superconductors expel the magnetic field completely until it forces the superconductor to return to its normal state. This upper critical field is denoted as H_c, and its value is temperature dependent. The higher the temperature, the lower H_c, until it becomes zero at $T = T_c$. The behavior of Type II superconductors however is described by two of such upper critical field boundaries. Above a certain threshold, H_{c1}, the magnetic field can partly penetrate a Type II superconductor. So-called vortices form, through which quantized amounts of magnetic flux may pierce through the material. At the cylindrical walls of such a vortex, compensating currents flow, in order to compensate the magnetic field again. Above the higher, second threshold, H_{c2}, Type II superconductors are then forced entirely into the normal state. H_{c1} and H_{c2} are temperature dependent in a very similar manner as H_c of Type I superconductors.

   Another important consequence of the Meissner effect is flux focusing. Any magnetic field expelled by a superconductor is in fact diverted. Hence, the field

strength around the superconductor increases in general, which must be taken into account when exposing superconducting devices to magnetic fields. As a result, the effective magnetic field within the narrow N-part of a Josephson junction (see Figure 2.7) with much larger superconducting contact leads can be significantly increased by the flux-focusing effect. Furthermore, in the case of Type II super-conductors, the formation of vortices occurs suddenly and may cause flux jumps, sudden jumps of the effective field, and aberrations from the initially applied field values.

Both superconductors used in this work, Nb and V, are type II supercon-ductors and hence allow for vortices to form within the superconducting contact leads of the devices. As a result, flux focusing, jumps and shifts are expected to occur and are taken into account in experimental discussion.

2.3.3 SUPERCONDUCTING PROXIMITY EFFECT

When a superconductor (S) and a normal metal (N) are put into direct contact, the superconducting properties can change the physics of the normal metal. Not only both their electronic properties leak into the other over a certain distance, but also new quantum states emerge. This interplay strongly depends on the properties of their interface [32, 63].

Even though normal metals and superconductors are both expected to be very good conductors, when comparing their densities of states, one may find that there is a fundamental mismatch when it comes to electronic conduction between them. Figure 2.6 sketches an idealized version of an N-S contact with their respective density of states. The energy spectrum of the normal metal is continuous, and conduction is provided by electrons with energies close to the Fermi level. Inside the superconductor, within an energy band of size 2Δ around the Fermi energy, all quasiparticle states vanish and only Cooper pairs are allowed to exist. Thus, the transmission of single quasiparticles from N to S is suppressed, if the driving voltage lies below the superconducting gap $eV < \Delta$.

At energies within the superconducting gap, the fundamental process of transmission through an N-S interface is Andreev reflection. An incoming elec-

tron from the normal metal side is retroreflected (along the same path but in the opposite direction) at the interface as a hole with inverse momentum, negative energy and opposite spin. This creates an outbound Cooper pair on the superconductor side. The reversed process is also possible, a hole being retroreflected as an electron at the N-S interface, which costs the superconductor one Cooper pair.

2.3.4 TOPOLOGICAL SUPERCONDUCTIVITY IN TI NANOWIRES

When superconductivity is induced from an ordinary s-wave superconductor into the Dirac surface states of a strong TI, the resulting state of matter is topological superconductivity [5, 6, 14]. In the case of the surface states of TI nanowires, upon simplification, such as considering the locked spin as spinless, and together with the particle-hole symmetry established by the induced superconductivity, a single subband can be modeled by the 1D Kitaev chain [64]. In this model, after reconstructing the electron creation and annihilation operators with two Majorana operators, it can be shown that unpaired Majorana fermions may exist at both ends of the chain at zero energy cost [40]. If the number of contributing subbands is even, the Majorana fermions can pair up again. However with an uneven number, unpaired Majorana fermions will be left at the ends of the superconducting part of the nanowire.

Interestingly, if a TI nanowire is exposed to a longitudinal magnetic field such that its cross section is pierced by half a flux quantum, the gapless non-degenerate mode is restored, and all other sub bands become degenerate again. Hence, at all locations of the chemical potential within the bulk band gap, the number of Fermi points will always be odd, and Majorana fermions are predicted to exist within the entire band gap [10]. In the case of Bi_2Se_3, it can be as large as $0.3\,eV$ [4, 10].

2.3.5 MAJORANA FERMIONS IN TI NANOWIRES

TI nanowires are a promising platform for Majorana fermion research. The key proposal that substantially inspired the work in this thesis was made by Cook

et. al in 2011 [3, 10]. It proposes a comparably simple device, which consists of a TI nanowire and an s-wave superconductor, which are exposed to a magnetic field along the nanowire axis. Depending on the magnetic flux through the cross sectional area of the nanowire, single unpaired Majorana fermions are predicted to exist at each end of the nanowire.

In TI nanowires, the protected spin-non-degenerate gapless surface state which is characteristic to TIs becomes quantized, the gapless mode disappears and a spectrum of spin-degenerate sub-bands forms (described in more detail in Sections 2.2.1 and 2.2.2). Each sub-band may host unpaired Majorana fermions at its ends as in the Kitaev chain [64], if superconductivity is induced introducing particle-hole symmetry. The magnetic field piercing through the nanowire cross section shifts the spin-degenerate bands in energy and lifts the degeneracy, and odd numbers of fermi points become possible. That is, if the chemical potential cuts through odd numbers of single sub-bands, unpaired Majorana fermions are predicted to exist at the end of the TI nanowire. With half-integer multiples of the flux quantum piercing the nanowire cross section, the number of fermi points is odd across the entire band gap.

2.4 Characterizations of proximity-induced super-conductivity: Josephson junctions

Josephson junctions are very important device architectures for investigating proximity induced superconductivity. Not only can a dissipationless current show the successful proximitization, because the current must flow through the nanowire segment connecting the two juntion electrodes, but there are many more parameters that become accessible through various types of measurements. For example, interface transparency, the magnitude of the induced gap and the current distribution inside the TI material can be investigated in transport experiments [34].
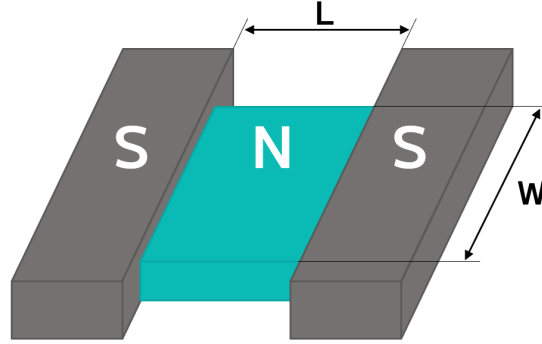
Figure 2.7: **Sketch of an S-N-S Josephson junction.** *Two pieces of superconductor (S) connected by a normal metal (N) of length L and width W.*

2.4.1 DC AND AC JOSEPHSON EFFECTS

In 1962, Brian Josephson changed the consensual belief that the tunneling probability of a Cooper pair through an insulating barrier should be proportional to the square of the individual electron tunneling probability, and thus, vanishingly small. Instead, he considered the wave function of the superconducting ensemble for the tunneling process, and predicted mathematical relationships for the current and the voltage across weak links [65]. Named after him, the DC and AC Josephson effects on the one hand may allow a supercurrent to flow across an insulating barrier without any voltage needed, and on the other hand create a high frequency oscillation of current when a finite voltage is applied [66].

The DC Josephson effect,

$$I = I_c \sin \phi, \tag{2.5}$$

consists of a direct current between two superconducting islands that depends only on their superconducting phase difference ϕ and the critical current I_c of the junction, the maximal supercurrent that it can endure. The AC Josephson effect is an expression for the voltage,

$$V = \frac{\Phi_0}{2\pi} \frac{\partial \phi}{\partial t}, \tag{2.6}$$

that is proportional to the time derivative of the phase difference $\partial \phi / \partial t$ across the junction. Since the experiments conducted for our work are based on low frequency

lock-in measurements, and the Josephson junctions are measured in current biased setups, the AC Josephson effect is less relevant and the DC Josephson effect is in focus. While the phase difference between the two superconducting islands is not a directly measurable parameter, it defines the physics of the Josephson junction in perpendicular magnetic field, which will be described in the next section.

Another quantity to be considered is the Josephson coupling energy. Although in the superconducting state no energy is dissipated in a junction, an energy is stored within if a nonzero current is flowing. This can be understood by considering the fact that an increase in current requires a phase change (Equation 2.5), and a phase change requires a nonzero voltage (Equation 2.6). Upon integrating the product of current and voltage, one may find the Josephson coupling energy $E_J = \frac{\Phi_0 I_c}{2\pi}(1 - cos(\phi))$ [66]. For junctions with very small critical currents, if its magnitude is comparable to thermal energy $k_B T$, thermal broadening may smear the measurements. As an example, the Josephson coupling energy at the critical current ($\phi = \pi$) of $I_c = 1\,\text{nA}$ in units of k_B amounts to

$$E_J(1\,\text{nA})/k_B = 23.8\,\text{mK},\tag{2.7}$$

which is of the order of the base temperature of the cryostats used for the Josephson junction measurements.

2.4.2   THE FRAUNHOFER PATTERN

When a Josephson junction is exposed to magnetic field, the superconducting electrodes expel the field but the normal metal part does not, and therefore electrons travelling through acquire a phase, depending on their path. Based on the DC Josephson effect, this interference manifests itself as a sinusoidal variation of forward and backward flowing currents, distributed along the junction's width, see Figure 2.8a-d. The sum of this distribution yields the net current, resulting in a reduction of the total critical current, which has a field dependence

$$I_c(\Phi) = I_c(0)\left|\frac{\sin\frac{\pi\Phi}{\Phi_0}}{\frac{\pi\Phi}{\Phi_0}}\right|,\tag{2.8}$$

see Figure 2.8e. Key parameter is the projected area of the junction, because the current interference is periodic in magnetic flux through the junction area $\Phi = \mathbf{B} \cdot \mathbf{A}$ in units of $\Phi_0 = h/2e$. The pattern consists of a central lobe and a series of adjacent side-lobes of decaying height which meet their neighbor at zero at every multiple of Φ_0 (except for the zeroth at $\Phi = 0$ where no interference takes place in the absence of field).
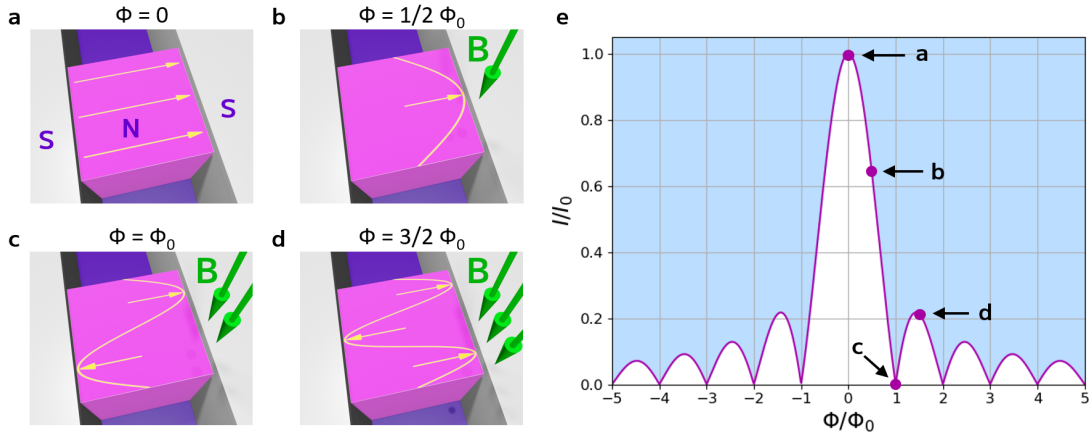
Figure 2.8: **Fraunhofer pattern in perpendicular magnetic field.** **a-d** *Electrons crossing the N part of the junction acquire a phase which leads to a local variation in Josephson current. With increasing field, the sinusoidal distribution becomes narrower, given its periodicity in $\Phi = \mathbf{B} \cdot \mathbf{A}$ in units of Φ_0. The sum over the current distribution yields the net current shown in **e**. The purple line shows the expected field-dependent switching current, white and blue areas are superconducting and dissipative ranges, respectively. Images inspired from [66].*

Deviations from the prototypical Fraunhofer pattern shown in Figure 2.8e can provide insights into a non-uniform current distribution along the junction width. Irregular patterns, such as missing side-lobes have been shown to arise from non-homogeneous current distributions [34], or computed based on inhomogeneous magnetic field profiles [67]. Edge-channel-dominated transport is expected to enhance the side-lobes towards a SQUID-like pattern [68, 69]. The opposite case, a Fraunhofer pattern with smaller or no side-lobes at all, can emerge from specially taylored junctions with Gaussian [70] or quartic shapes [71], or in the case of very narrow but diffusive junctions [72–74], or applying the magnetic field

in-plane to a thin junction [75]. A key signature of these patterns is a slowly decaying supercurrent at higher fields, as in a Gaussian curve. This field dependence, although with faint but remaining side-lobes has been observed in Nb Josephson junctions on $(Bi_{1-x}Sb_x)_2Te_3$ nanoribbons [23] and on InAs nanowires [76].

In the 1D-limit, e.g. in the case of proximitized quantum confined surface states of TI nanowires, a monotonous decay of the critical current in magnetic field is expected instead of a Fraunhofer [77], as it has been observed in etched TI nanowire Nb Josephson junctions by Rössler *et al.* [17].

2.4.3 THE S-N-S JUNCTION

The nanowire Josephson junctions in this work are analyzed within the S-N-S (or S-I-N-I-S) picture drawn by Blonder, Tinkham and Klapwijk (BTK), see Section 2.4.6, which takes into account arbitrary barriers at the S-N interfaces [78]. To be more precise, the full picture could be sketched as a S-I-S'-I'-N-I'-S'-I-S constriction [23, 79], as illustrated in Figure 2.9. While the S elements are the superconductor leads to the nanowire, including the junction electrodes, the S' notation describes the TI parts which are directly under the superconductor leads and are fully proximitized. Then, N denotes the nanowire part linking both S' segments. The insulating layer I between S and S' is then the interface between nanowire and superconductor, which is largely affected by the precise details of nanofabrication and metallization.

The barrier I' in between S and S' however is a more subtle concept. The tunnel coupling between the superconductor and the TI nanowire (thus the S-I-S' parts) and the fermi level mismatch induce changes in the proximitized TI segment, e.g. shifting and splitting the surface subbands, enhancing *n* type doping [18, 44]. Hence, the S' and N parts have different properties, justifying taking another barrier into consideration, I', in between S' and N. This can limit the success in making the 'perfectly transparent' TI Josephson junction device, and what is characterized when determining the OTBK-transparency, see Section 2.4.6.
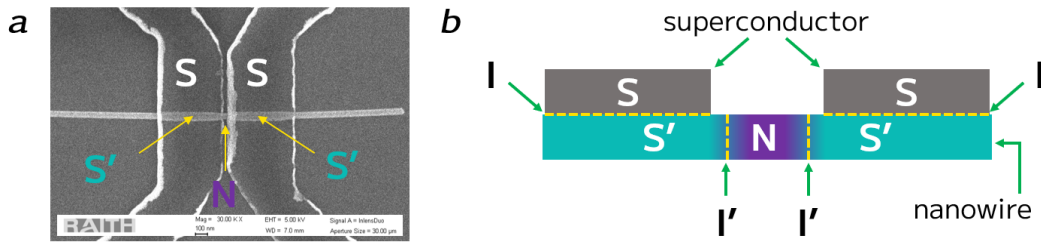
Figure 2.9: **Sketch of the S-I-S′-I′-N-I′-S′-I-S junction picture.** *The nanowire segments below the superconducting leads (S) are proximitized and denoted as (S') and connected by the normally conducting nanowire link (N). I and I' denote the interfaces or barriers between these segments.* **a** *Top view based on an SEM picture.* **b** *Side view as sketch.*
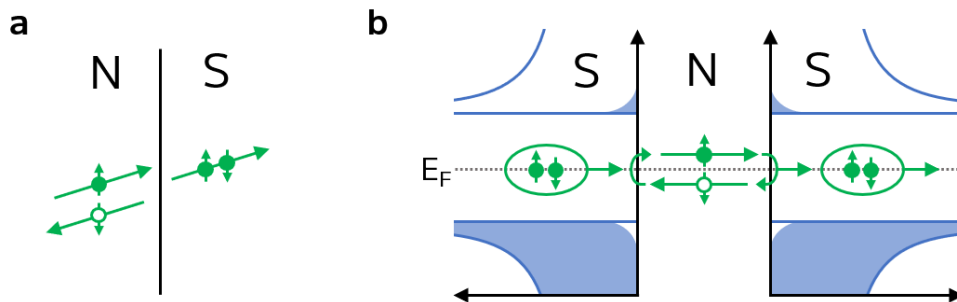
Figure 2.10: **Schematics of Andreev reflection and Andreev bound states. a** *At an N-S interface, an incoming electron from N cannot simply enter S, but it can be Andreev reflected as a hole with opposite momentum and energy, generating an outbound Cooper pair in S.* **b** *The constriction of a short S-N-S junction gives rise to Andreev bound states. Cooper pairs can be passed through by performing two mutually reversed Andreev reflections at both interfaces.*

2.4.4 ANDREEV BOUND STATES

Inside as shortly stacked S-N-S structure, the confined Andreev reflection processes on both interfaces may lead to the formation of Andreev bound states. This excitation spectrum in the N part for energies within the superconducting gap is the key conductance mechanism for the Josephson current. This steady paddling mechanism can now transfer Cooper pairs from one S to the other S side. An incoming Cooper pair from the left superconductor is transmitted as an elec-

tron and an Andreev-reflected counterpropagating hole, and by the same reversed process on the right interface, a Cooper pair leaves into the right superconductor, as illustrated in Figure 2.10b.

2.4.5 MULTIPLE ANDREEV REFLECTIONS
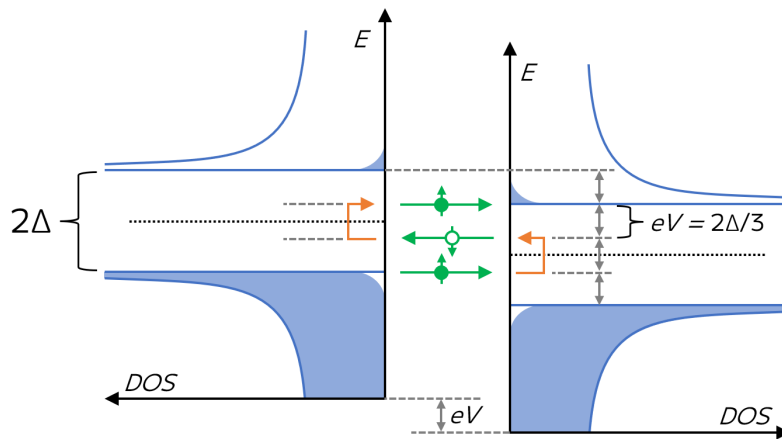
Figure 2.11: **Schematic of multiple Andreev reflections in an SNS junction.** *If a finite voltage is applied to an SNS junction, electrons and Andreev-reflected holes gain energy upon crossing the N part. For $eV_n = 2\Delta/n$, $n = 1, 2, 3, ...$, meaning that the applied voltage is an integer fraction of the pairing energy, conductive resonances appear, because the energy gap can be overcome by performing a sequence of such Andreev reflections.*

In the finite voltage state, successive Andreev reflections at both interfaces can also play a role in charge transfer across the junction, if the voltage difference amounts to an integer fraction of twice the superconducting energy gap. Through these multiple back-and-forth reflections, which mirror the quasiparticle's energy each time at the respective superconductor's Fermi energy, a path between the accumulated densities of states outside the pairing gap of the two superconductors emerges, see Figure 2.11. At high enough interface transparencies, these paths can significantly contribute to charge transfer and show as features in the I-V curve, located at voltages $eV_n = 2\Delta/n$, $n = 1, 2, 3, ...$ [79–82].

2.4.6 INTERFACE TRANSPARENCY

When quantifying how well nanowires are proximitized in a Josephson junction device, there are two key parameters that can be extracted and calculated from I-V curves. On the one hand, the magnitude of the induced gap $\Delta_{induced}$, and on the other hand, the OTBK-transparency T.

In 1982, Blonder, Tinkham and Klapwijk (BTK) [83] numerically calculated I-V curves for N-S interfaces with arbitrary barrier heights, and develop a relationship between the fraction $\frac{eI_{exc}R_N}{\Delta_{induced}}$ and the barrier height Z, with the excess current I_{exc}, and the normal state resitance R_N. A year later, Octavio, Tinkham, Blonder and Klapwijk (OTBK) [84] refine the model and extend it to S-N-S junctions, to which Flensberg and Hansen make corrections in 1988 [80], bringing theory to very good agreement with experimental data. In 2009, Niebler *et al* [85] derive the analytic relation

$$\frac{eI_{exc}R_N}{\Delta_{induced}} = \frac{2(1+2Z^2)\tanh^{-1}(2Z\sqrt{A/B})}{Z\sqrt{AB}} - \frac{4}{3}. \tag{2.9}$$

with $A = (1 + Z^2)$ and $B = (1 + 6Z^2 + 4Z^4)$. From the barrier height, the transparency computes as

$$T = \frac{1}{1+Z^2}. \tag{2.10}$$

For the calculation of the OTBK transparency, the following parameters need to be extracted from an I-V curve. The normal resistance R_N manifests itself as the slope of the I-V curve at high voltages in its linear regime. In this work, I_{exc} is determined by fitting a straight line to the linear regime of the I-V curve, extrapolating it to $V = 0$ and taking the current axis intercept. Finally, the voltage, at which the first order multiple Andreev reflection is observed, naturally corresponds to twice the induced superconducting gap $eV_{MAR,n=1} = 2\Delta_{induced}$. Above this voltage, the I-V curve generally turns linear, which is an alternative means of estimating this energy scale, if multiple Andreev reflections are not well pronounced.

Alongside the transparency, another quantity can be defined,

$$\Delta_{relative} = \Delta_{induced}/\Delta_{superconductor}, \tag{2.11}$$

with the superconducting energy gap $\Delta_{\text{superconductor}}$ of the superconductor leads. This ratio provides a relative measure of how large a superconducting gap is induced in the TI directly below the superconducting leads. The OTBK transparency then characterizes the S'-N-S' junction formed between these directly proximitized TI parts (S') and the connecting TI segment in betwen (N), in our case an uncovered part of nanowire linking the junction leads.

2.5 Characterizations of proximity-induced superconductivity: Tunneling junctions

Contacting a sample, e.g. a superconductor, through a thin insulating barrier, makes it possible to investigate the local density of states through tunneling spectroscopy. Based on the BCS theory of superconductivity, the following section briefly explains how the density of states can be deduced from the tunneling current to a nanowire.

2.5.1 Principle of tunneling junction experiments

When a conductor is terminated by an insulating barrier, the electronic wave function does not stop abruptly but decays exponentially into the barrier. This gives rise to a finite probability for the electrons to tunnel through it. As a consequence, if two conductors are separated by a barrier, a tunneling current I can be measured, if the conductors are biased by a voltage V. A general expression for the net current between a normal conductor (N) and a superconductor (S), as depicted in Figure 2.12, can be written as

$$I = C \int_{-\infty}^{+\infty} N_{\text{N}}(E) N_{\text{S}}(E + eV)[f(E) - f(E + eV)]dE, \qquad (2.12)$$

with N_{N}, N_{S} the respective density of states, $f(E)$ the Fermi-Dirac distribution and proportionality factors and tunneling matrix element that are assumed as constant incorporated in the factor C.

A typical purpose of a tunneling spectroscopy measurement is to investigate the density of states in a sample, which can be inferred directly through a

Figure 2.12: **Electron tunneling between a normal metal (N) and a superconductor (S).** *The tunneling current through the barrier depends on the densities of states and temperature-dependent occupation numbers on both sides, looking almost step-like in N. By applying a bias voltage V, the Fermi level of N, the energy with the highest contribution to the tunneling current from the N side, is shifted past the band structure of S by eV, resulting in a bias-voltage dependent tunneling current that represents the density of states in S. Inspired by [86].*

measurement of the differential conductance dI/dV. Calculating the derivative of Equation 2.12 and assuming the density of states in the normal metal to be constant leads in the low-temperature limit to

$$dI/dV \propto N_{\mathrm{N}}(E_{\mathrm{F}})N_{\mathrm{S}}(eV) \propto N_{\mathrm{S}}(eV). \tag{2.13}$$

The differential conductance can be measured directly with an oscillating voltage signal from a lock-in amplifier, which is biased with a DC voltage source.

3

Experimental Methods

In this chapter, the experimental practices and the laboratory equipment employed for the characterization of nanowires are presented. This comprises the characterization of nanowire growth by scanning and transmission electron microscopy as well as energy-dispersive x-ray spectroscopy, the nanofabrication of lithographic devices and the low-temperature equipment to perform electronic transport measurements at low and ultra-low temperatures.

3.1 Characterization of grown nanowires

Before qualifying for the lengthy processes of device fabrication, contacting and cryogenic electronic transport measurements, the VLS-grown nanowires must be characterized. The characterizations that can be done with reasonable effort after each growth are Scanning Electron Microscopy (SEM) and Energy-Dispersive X-ray spectroscopy (EDX). With SEM, from overviews down to close-up images of individual nanowires can be taken directly off the growth substrates. These

grayscale images are sensitive to material density or surface morphology. EDX systems are frequent additions to SEM columns, such that the object imaged by SEM can also be analyzed in terms of material composition with EDX. When it comes to crystal structures, Transmission Electron Microscopy is an imaging method of interest. Crystal structures can be visualized, with the drawback that samples must be transferred on thin carrier grids. Since taking such pictures is more complicated, especially high resolution images of crystal structures, this was done only for selected samples. In the following sections, these technologies are briefly explained.

3.1.1 SCANNING ELECTRON MICROSCOPY (SEM)

A scanning electron microscope scans samples with a focused beam of accelerated electrons. Through a precisely timed detection of either backscattered or secondary electrons, the resulting information is arranged according to the scanning sequence pixel by pixel into images.

A typical SEM column consists of an electron source, several electrostatic and magnetic elements including acceleration, focusing and deflection of the electron beam, a movable sample stage and detectors, which are all operated by a computer. After generating a beam of accelerated electrons with an energy between a few and hundreds of keV (in our case $5 - 30 \, \text{keV}$), and focussing on the sample surface, it is deflected by the x-y-deflection stage. In this way, a precise spot of incident electrons scans the sample surface rapidly, line by line of a rectangle, which is the imaged area chosen by the user. The beam interacts with the sample and generates a series of outgoing radiation, including backscattered electrons, secondary electrons and X-ray radiation. The latter will be used for EDX, see below. Both former can be used for SEM image generation, with the help of the respective detectors. Time-resolved detection of the radiation enables the computer program to arrange the data in the same geometry as it was scanned, line by line of a rectangle, resulting in an image of the chosen area of the sample surface.

Backscattered electrons contain information about the weight of atoms they

were scattered elastically from. Heavier elements backscatter more efficiently and thus appear brighter in the resulting images. Secondary electrons originate from inelastic scattering with the sample close to its surface, and provide topographic information. If available, the detection of both can be combined in order to generate more informative images.

3.1.2 Energy-Dispersive X-ray spectroscopy (EDX)

Energy-dispersive X-ray spectroscopy uses characteristic X-radiation in order to gain information about the elements contained in a sample. If combined with an SEM system, the user can select any object or region within the imaged sample to be analyzed in terms of elementary composition. It will then be irradiated by the accelerated electron beam, and the characteristic X-radiation is detected, which originates from the following process. Some of the inelastically scattered incident electrons eject an electron from an inner shell of the target atom. The initial condition will be restored by taking an electron from the surroundings and a variety of possible de-excitations. Electrons from higher shells will fall into lower shells, emitting photons of the respective energy difference. Since the orbital energies are different for every element, the resulting radiation is characteristic. The recorded EDX spectra contain signals of many atoms and are analyzed with the help of a statistical model. By reconstructing the recorded spectrum with combinations of the characteristic X-ray spectra of all possible elements, a weighted distribution of constituent elements is calculated.

When analyzing thin objects such as nanowires, the choice of acceleration voltage is influenced by the following trade-off. Higher energy electrons penetrate the sample more deeply and thus provide more information about volumes deep within the sample substrate, while the nanowires on the surface only make up a fraction of the measured spectrum. A lower energy electron beam however may produce less characteristic X-rays, depending on the contained elements. Only excitations with energies less than the incident electron beam energy are possible.

In this work, EDX spectra were mainly recorded with a beam energy of 20 kV, such that the L-lines of Bi, Sb, Se and Te are all still resolved. Since the Si/SiO_2

substrates contain none of these elements, the nanowire composition is calculated from their relative weight in the spectra, excluding the substrate contributions.

3.1.3 TRANSMISSION ELECTRON MICROSCOPY (TEM)

The structure of a transmission electron microscope is similar to that of a scanning electron microscope. The main difference is that the sample must be thin, the electrons pass through it, and the image is captured at once (no scanning) on the other side of the sample, hence transmission. With acceleration voltages of several hundreds kV, crystalline samples that are cut precisely into thin layers along its crystal structure and orientated such that the beam axis matches geometrically, images can be taken with resolutions down to the atomic scale. The TEM images of the $(Bi_{1-x}Sb_x)_2Te_3$ nanowires were taken by Dr. Stefan Roitsch in the Department of Chemistry, the images of the $Bi_2(Te_xSe_{1-x})_3$ nanowires by Dr. Thomas Fischer in the Institute of Inorganic Chemistry of the University of Cologne. The available acceleration voltages range up to 300 kV.

3.2 DEVICE FABRICATION

Electronic transport measurements on crystals on the micro- and nanoscale in general requires the nanofabrication of lithographic devices, which was done by electron-beam lithography (EBL). In the case of nanowires, the devices are especially challenging to fabricate. Being some of the smallest crystals to be measured, nanowires are mechanically fragile, prone to endure damage during fabrication and very easy to be destroyed by electrostatic discharge. Nanowires out of the Bi, Sb, Te and Se family are especially brittle, such that surface treatment, removal of oxide, the transfer from growth substrate to device wafer and also the lift-off step in device fabrication are challenging and fragile tasks. Several key factors in the fabrication chain were developed and optimized, which substantially increased the success rate and shortened the fabrication cycle.

- The transfer of nanowires was done dry and manually by directly joining the surfaces of the growth and device substrates together, without the use of any chemical (Section 3.2.3).

- For the localization of transferred nanowires with respect to the on-chip coordinate system, a *Python* program was developed, significantly speeding up the process and allowing a higher number of devices to be made within reasonable timeframes (Section 3.2.4).

- For device layout design, a *Python* program was developed, again significantly shortening design time. More importantly, by making the creation and finalization of complex device layouts feasible, higher lift-off success rates could be achieved with more elaborate and streamline shaped device layouts, instead of the commonly used simplistic square-and-rectangle style (Section 3.2.5).

3.2.1 FABRICATION OUTLINE

The fabrication of superconducting contacts and the fabrication of normal-state ohmic contacts to the nanowires both follow the same basic outline, which is

illustrated in Figure 3.2, left column. Main differences are in the choice of surface preparation and metallization. Tunneling electrodes are fabricated through the steps illustrated in Figure 3.2, right column. Each step is described in more detail in the following sections.
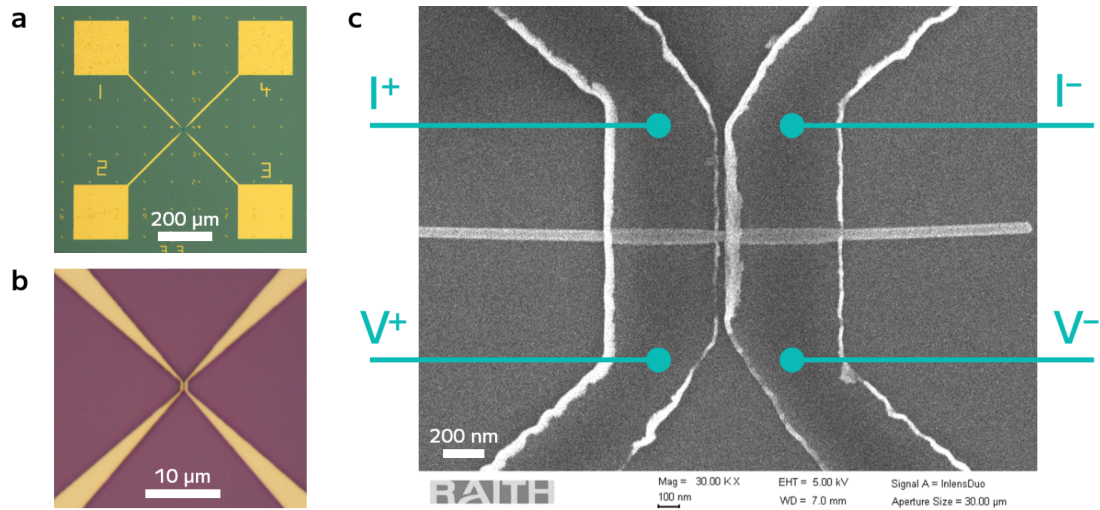
Figure 3.1: **Nanowire Josephson junction device. a** *Optical microscope image of the outer device layout showing the Nb leads and contact pads and* **b** *at higher magnification of the inner part of the leads and the Josephson junction at the center.* **c** *SEM image of the nanowire and the Nb leads on top. The colored lines show how the current is injected and the voltage drop is measured with lock-in technology.*

3.2.2 DEVICE SUBSTRATES / MARKED WAFERS PREPARATION

Devices are fabricated on Si/SiO_2 substrates, with a 280 nm thick SiO_2 surface layer on top of B-doped conducting Si wafer. Beforehand, with the help of a lithographic photomask exposure, the substrates are structured with a coordinate system into the photoresist AZ 1505 using the developer AZ 326. Metallization consists of either Pt+Au (5 nm+40 nm) for the ohmic devices or Nb (20 nm) for the superconducting devices.

Prior to nanowire transfer, the marked wafers are cleaned and prepared as follows. The protective resist layer is washed off using either warm acetone and/or
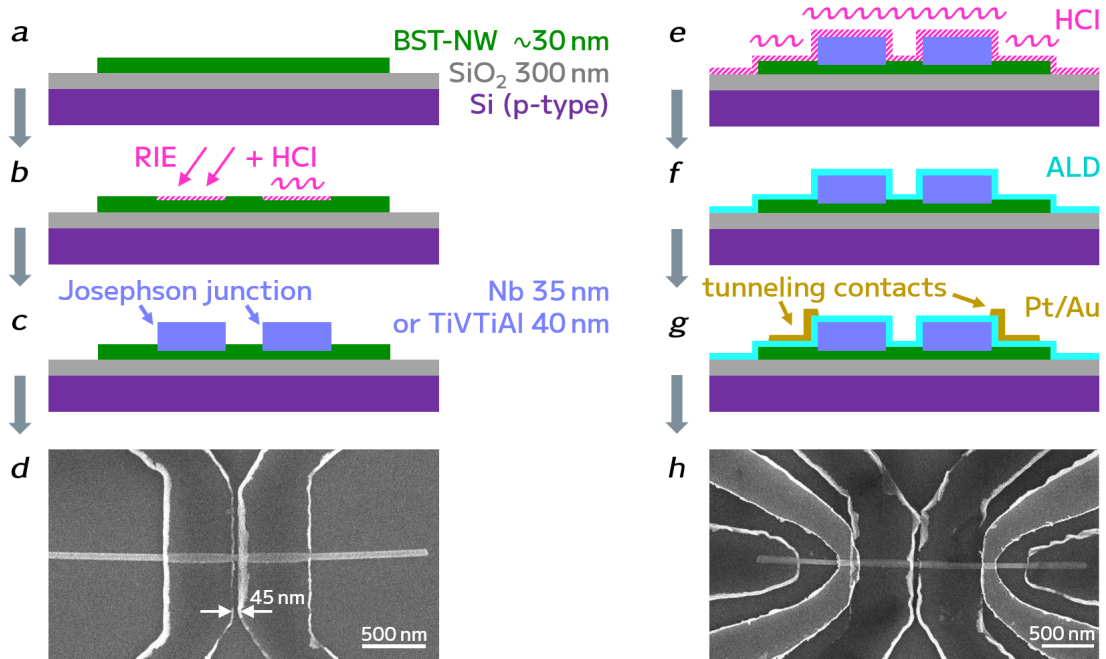
Figure 3.2: **Device fabrication: nanowire Josephson junction (left) with tunneling electrodes (right).** *Resist process omitted for clarity.* **a** *transferred nanowire,* **b** *descumming (O_2 or Ar dry-etching) and native-oxide removal (hydrochloric acid),* **c** *superconductor metallization.* **d** *SEM image. For tunneling contacts:* **e** *Native-oxide removal,* **f** *Al_2O_3 atomic layer deposition,* **g** *metallization of tunneling electrodes.* **h** *SEM image of finished $(Bi_{1-x}Sb_x)_2Te_3$ Nb-junction (dark leads) with tunneling electrodes (bright leads).*

ultrasonication. The acetone is washed off by ultrasonication in isopropyl alcohol. Finally, the substrates are UV-ozone cleaned for 2 min to improve adhesion of the EBL resist after nanowire transfer. This step is performed directly before, and the EBL resist is spun directly after nanowire transfer.

Alternative substrates. Several device batches were fabricated on two different types of substrates, 50 nm SiO_2 on doped Si, and 280 nm SiO_2 on insulating Si. In the former case, the objective was to decrease the distance of the bottom-gate to the nanowire inside the Josephson junction, but this strategy was abandoned because the integrity of the thin dielectric was mechanically too unreliable, frequently compromising the bottom-gate. In the latter case, the fabrication was successful, and due to the insulating carrier wafer, wirebonding could be done without special

precaution. However, the experiments finally required changing the chemical potential in the nanowires, which is done preferably through a bottom-gate because of the superconducting leads shielding the top side of the nanowire. Therefore, fabrication returned to the 280 nm SiO_2 on doped Si wafers.

3.2.3 NANOWIRE TRANSFER ON MARKED WAFERS

The VLS-growth substrates are extracted from the tube furnaces and either stored in vacuum or directly used for nanowire transfer, and subsequently stored in vacuum. Transferring nanowires onto the marked wafers is performed in a dry manner without involving any chemicals. After the target substrate is cleaned, the growth substrate is carefully placed upside-down on top of it, such that their surfaces touch. Then, depending on the number of already performed transfers from that growth substrate and the desired transfer yield, pressure can be exerted with a tweezer, pressing the two substrates onto each other. This step requires subtle precision because lateral force must be prevented as much as possible. Grinding the nanowires and scratching the surfaces must be omitted in order to keep the transferred samples as well as the SiO_2 dielectric intact.

This motorically challenging but minimally invasive transfer method has two principle advantages. Firstly, the nanowires are neither exposed to any additional chemical nor are they flushed through the tip of a syringe. Secondly, nanowires can be chosen deliberately from specific locations on the growth substrate and transferred to specific location on the marked wafer.

After successful transfer, the EBL resist is spun on immediately in order to prevent further oxidization. Optical images for selection and localization of nanowires can be done through the EBL resist without complications.

3.2.4 MICROSCOPE IMAGE ALIGNER (PYTHON)

This section briefly introduces the Python program *Microscope Image Aligner (MIA)* that was developed during this work.

For the lithographic pattern design, the nanowires to be used for devices must be precisely located with respect to the on-chip coordinate system and
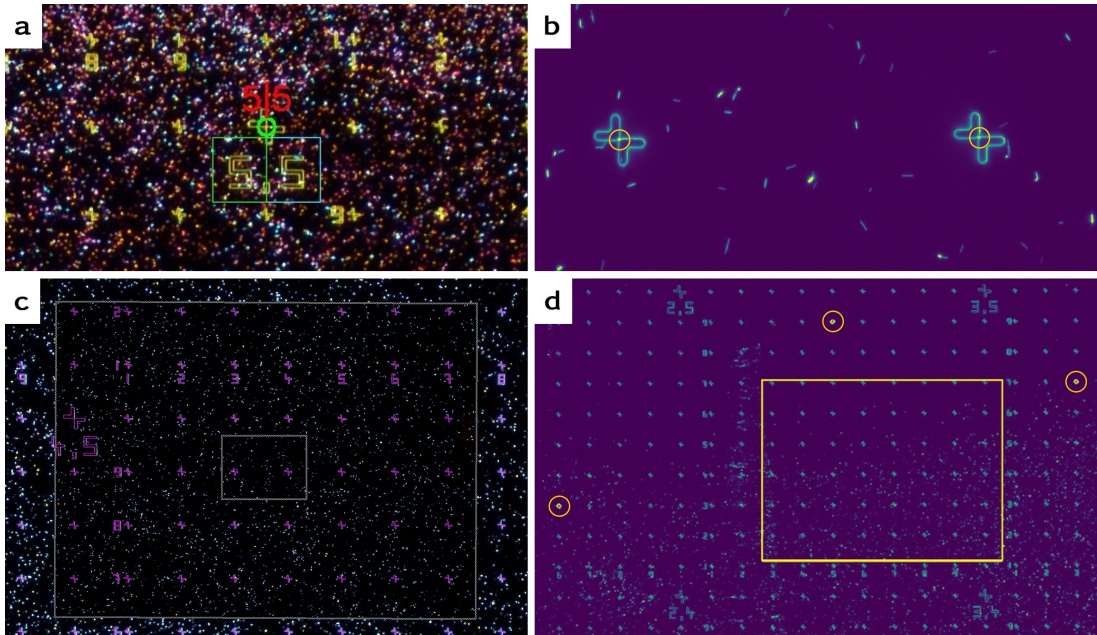
Figure 3.3: **Microscope Image Aligner (MIA). a** *Large marker (1 mm grid, green circle) and coordinate recognition (red) succeeds even with exaggeratedly high sample concentration on the substrate.* **b** *Highest magnification image showing the nanowires to be selected by the user, and the identified small markers which are precisely aligned to the 100 μm grid, guaranteeing pixel-precise localization of the nanowires in the design files.* **c** *Intermediate and high magnification images (20x, 100x) aligned to the low magnification (5x) image that was aligned with the help of its coordinates in the previous step. Visible matching of the imaged coordinate markers and the markers from the design file (magenta).* **d** *To compensate for error accumulation, each image that was optically aligned to its lower magnification parent is additionally fine-aligned to the 100 μm grid with the help of a random selection of up to 6 (to minimize processing time, yellow circles) of the identified small markers.*

integrated in a circuit design software layout file. These repetitive steps were automated through *MIA*, resulting in a significant speedup of design work. The most important decision at this stage, the choice of which nanowire exactly to select for the individual devices, however, remains in the power of the user.

As imaging method, only optical microscopy is used and the SEM is omitted at this stage in order to minimize radiation damage [87]. Dark-field images have shown to be most useful when working with nanowires. Not only are the nanowires

visible even at the lower magnifications, but also an impression of their shape, cleanliness and condition can be gained by this edge-sensitive imaging method. To this purpose, dark-field images are taken from low (5x) to high (x100) magnification for each device candidate nanowire.

From here, *MIA* takes over until the finished alignment of all images in a *.lys* session file for the widely used and free layout editor *KLayout*, as well as an initial *GDSii-TXT* layout file containing the tentative device locations, the precise on-chip coordinate system and editable device design templates. First, the low-magnitude images are aligned with the aid of the large markers (1 mm grid) and x, y coordinates. Subsequently, for each device, higher magnification images are successively matched as picture-in-picture to their parent image. At each stage, a random selection of up to 6 (to maintain fast processing times) of the numerous small markers (100 µm grid) are used for a fine-alignment to their precise grid, such that positioning error accumulation is excluded, and the highest magnification images are fine-aligned to pixel precision. Total processing time per image is less than 1 s.

3.2.5 GDS� ii-TXT Manipulator (Python)

This section explains the basics of the Python program *GDSii-TXT Manipulator (GTM)* that was developed during this work.

In a nutshell, *GTM* is capable of multiplying device design templates onto the virtual locations of the nanowires or flakes selected by the user, respecting their individual location, rotation and size or scale, while adding a number of convenient additional features. These include device numbering, an orientation marker, contact lead numbering, inner marks for writefield alignment and a ready-to-load working area file compatible with *Raith Nanosuite*.

An important advantage of this way of working is that the user can manually design the desired device pattern just like in a graphics program (e.g. using the free software *KLayout*). As opposed to common programming-based lithographic pattern design practices, where the patterns are designed via parametrized paths and shapes in a programming language, such a level of abstraction is not needed,
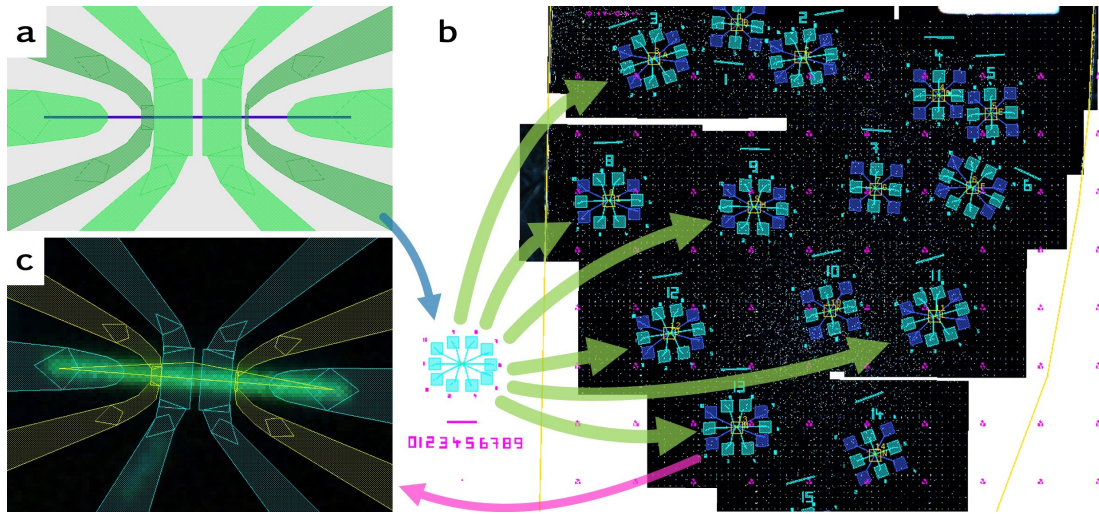
Figure 3.4: **GDSii-TXT Manipulator (GTM) working principle. a** *A device template is designed (or reused and modified) on a designated template nanowire.* **b** *After manual selection and marking of the nanowires to be used for devices, GTM multiplies, scales, rotates and fits the design on each nanowire, according to its size, orientation and location.* **c** *Successfully adapted device design on top of the original optical microscope image of a nanowire (blurred bright green).*

potentially resulting in a much workflow with less human errors. Adjustments can be made directly in the design file with visual feedback until the pattern is completely suitable. Time needed to fit a device layout on all selected nanowires on an entire chip is approximately 1 s.

3.2.6   RESIST, EXPOSURE AND DEVELOPMENT

The device layouts were patterned into the following EBL resists using the specified developers. For stability of the process, the developers were mixed beforehand and stored in a 21.5 °C controlled room temperature cabinet.

ZEP520A developed in O-Xylene is a high precision resist process and is comparably easy to use, because of the step-like sensitivity curve. In some cases however, adhesion to the SiO_2 substrate surface was problematic.

The best results were achieved with PMMA A4 developed in a mixture of H_2O and isopropyl alcohol at a 3:7 ratio. This process is more delicate to handle because it is very sensitive to development time and temperature, but

therefore permits the highest variation in undercut design and liberty in higher-dose-smaller-design practices. By increasing the dose and compensating for the widened exposure by shrinking the device layout shapes, additional degrees of freedom for dose testing are obtained. By this method, the pronounced fencing of Nb can be reduced and narrow gaps between Josephson junctions electrodes can be fabricated.

Larger structures such as 4-probe ohmic devices were fabricated using PMMA A6 developed in MIBK-isopropyl-alcohol mixture at a 1:3 ratio.

Spin coating was performed at 3000–4000 rpm for 60 s, followed by a 3–10 min softbake at 100–120 °C.

Electron-beam exposure was done in a *Raith Pioneer Two* at acceleration voltages 10 kV or 20 kV.

3.2.7 INTERFACE PREPARATION, METALLIZATION AND LIFT-OFF

After development of the EBL resist, a common descumming step is performed in an *Oxford PlasmaPro* to remove any residuals from the preceding processes. For $(Bi_{1-x}Sb_x)_2Te_3$ nanowires, 5 s of 20 W dry etching with 50 sccm O_2 at 100 mTorr are done, for $Bi_2(Te_xSe_{1-x})_3$ nanowires: 1 min of 10 W dry etching with 50 sccm Ar at 50 mTorr.

$(Bi_{1-x}Sb_x)_2Te_3$ nanowires grown by the VLS method form a native oxide layer of approximately 5 nm thickness (see Figure 1c in Chapter 5). In order to obtain high interface transparencies, this native oxide must be removed, which is done through wet etching for 20 s in 10x diluted 3.2% HCl solution and stopped with H_2O, in the last possible moment before loading into the deposition chamber. For $Bi_2(Te_xSe_{1-x})_3$ nanowires this step was not applied, because the contact resistance between the leads and the nanowire were satisfactorily low, of the same order as for the HCl-treated $(Bi_{1-x}Sb_x)_2Te_3$ nanowires. A likely reason is the significantly faster oxidization rate of Sb_2Te_3 (see Sections 4.2 and 4.3), which is absent in $Bi_2(Te_xSe_{1-x})_3$.

For ohmic contacts, 5 nm Pt and 45 nm Au are deposited in a *Mantis* sputtering machine. For Nb Josephson junction fabrication, 35 nm of Nb are deposited.

3.2. DEVICE FABRICATION

Due to observed detrimental effects on the interface transparency, the built-in Ar cleaner is omitted citeRoesslerThesis. Instead, after loading the device into the deposition chamber, it is pumped for approximately 12 h before initiating the deposition.

For TiVTiAl Josephson junctions, the device is loaded into the deposition chamber of a Plassys electron-beam evaporator after HCl treatment. The surface is treated with a 20 s Ar etch process at 80 V prior to the deposition of 5 nm Ti, 30 nm V, 5 nm Ti and 5 nm Al.

Lift-off is done in N-Methyl-2-pyrrolidon (NMP) at 60 °C or acetone at room temperature over $10 - 60$ min. The device is held in a sample holder above a magnetic stirrer rotating at 500 rpm. If necessary, the liquid is agitated locally with a pipette to rip off dangling metal pieces. Then, the remaining excess metal is removed with ultrasonication at the lowest power available for several seconds, under careful observation, using an additional glass of water for attenuation in between. Ultrasonication can break the nanowires where they are not covered by metal, but it is needed to reduce the metal fencing, especially in the narrow junction gap. Finally, the chemicals are washed off with isopropyl alcohol and the device is blow dried with N_2.

Contact resistances measured in a probe station could be as low as $0.5 - 2$ kΩ for devices with bulk-insulating nanowires with sample resistances in the range of $3 - 50$ kΩ.

3.2.8 FABRICATION AND ADJUSTMENT OF THE TUNNEL BARRIER

The tunneling contacts to the nanowires were fabricated as follows, illustrated in Figure 3.2. The native oxide of the nanowires is removed with the same HCl wet etching step as described above. Note that for the Josephson junction fabrication, only the nanowire surface below the junction contacts are cleaned, because this step is done after exposure of the pattern and before metallization. Now, the entire body of the nanowire including the junctions are submerged in diluted HCl. Then, the device is quickly loaded into an atomic layer deposition chamber (ALD) and 7 cycles of Al_2O_3 are deposited.

Next, the tunneling electrodes are defined by EBL with the same resist process with PMMA A4 as for the other contacts, except that no cleaning procedure is applied after development. In the *Mantis* sputtering machine, 5 nm Pt and 30 nm Au are deposited at a higher pressure of 10 mTorr to protect the tunneling barrier. In this step, the Au layer is thinner than for the ohmic contacts, such that the lift-off is less complicated without potentially ripping of the tunneling electrodes together with the excess metal.

Another route to fabricate tunneling electrodes was attempted that did not yield contact resistances in the desired range but rather open contacts. Here, the native oxide is kept and the HCl cleaning step is omitted, as well as the ALD deposition. Apparently, contacting the $(Bi_{1-x}Sb_x)_2Te_3$ nanowires directly through the native oxide with Pt/Au electrodes yields contact resistances in the range of $M\Omega$ and above.

3.3 Cryogenic transport measurements

Devices featuring Josephson junctions and tunneling contacts were measured in dry dilution refrigerators. Characterization of the grown nanowires through devices featuring ohmic contacts was performed in three kinds of wet refrigerators.

3.3.1 Cryostats

Fine-tuning of the nanowire growth: dipstick. After obtaining promising nanowire growth results assessed by SEM and EDX, the next step was to fine-tune the growth parameters in order to achieve the most compensated i.e. insulating nanowires. In a feedback cycle of growth, device fabrication and low-temperature electronic transport measurements, the relative composition x of $(Bi_{1-x}Sb_x)_2Te_3$ and $Bi_2(Te_xSe_{1-x})_3$ was adjusted. These measurements were carried out with the help of two primitive kinds of dipsticks inside a He dewar. Featuring no magnetic coils, the measurement parameters are limited to recording cooldown curves down to and electrostatic gating at liquid He temperature. Due to the mechanical details, effective base temperatures range between 4.3 K and 6.0 K. The cooling principle consists of storing liquid He at ambient pressure, with an open outlet to a recovery line. The liquid He stays below its boiling point of 4.2 K through evaporation and thus cools the dipstick when it is slowly inserted and lowered into the vessel. Custom sample carriers were made to fit the bonded device substrates.

Cryomag: VTI in liquid ^{4}He. Measurements in the temperature range of 1.7 K to 300 K and featuring magnetic field in one spatial direction were carried out in the *Cryomag* setup. A variable temperature insert (VTI) equipped with a superconducting solenoid and a switch-heater. By pumping evaporating He through a needle valve, the temperature can be lowered below its boiling temperature. The magnetic maximum field strengh amounts to 14 T.

Heliox: sorption pumped ^{3}He refrigerator. Measurements at temperatures down to 250 mK and also featuring a magnetic field in one spatial direction were carried out with the help of a *Heliox* insert by *Oxford Instruments* [88] inside a liquid He dewar. The *Heliox* probe is a sorption pumped ^{3}He refrigerator. This

system consists of two main cooling stages, the *1 K-pot* as a pre-cooler and the *^{3}He-pot*.

The *1 K-pot* serves as a pre-cooler and continuous heat sink, mainly for the *^{3}He-pot* and the *sorption pump*. It operates by evaporative cooling of ^{4}He, which it draws through its pickup tube from the main He bath and thus can operate continuously in principle, holding an approximately constant temperature of 1.5 K. Lower temperatures are achieved by the *^{3}He-pot*, which, however, must be operated in cycles. Given its critical point of 3.3 K, the ^{3}He inside the closed volume of *^{3}He-pot* and *sorption pump* is condensed by the cooling power of the *1 K-pot* and descends into the *^{3}He-pot*. From there, it cools down the sample holder through evaporative cooling which is solely mounted to its bottom, ideally down to 250 mK for up to 12 h. The vacuum pumping needed to pull the ^{3}He vapor from its liquid bath is effectuated by the *sorption pump*. This porous sieve material, e.g. activated carbon, being cooled by the *1 K-pot* adsorbs the evaporated ^{3}He, acting as a vacuum pump with a cold and shortest possible pump line. After the entire ^{3}He is evaporated and adsorbed, its cooling cycle has ended. In order to restore the initial state, the *sorption pump* must be heated to about 30 K for several minutes, such that all adsorbed ^{3}He evaporates, descends and liquefies into the *^{3}He-pot* again.

The dewar receiving the *Heliox* insert is equipped with a 16 T superconducting magnet submerged in the liquid He.

Triton: Dry ^{3}He/^{4}He dilution refrigerator. Measurements down to a temperature of 18 mK were performed in *Triton* dilution refrigerators [89]. Apart from the lower temperature and better noise conditions, a significant advantage of these setups is the installed vector magnet. Its field ranges amount to 1 T, 1 T and 6 T along x, y and z axis. In general, devices were aligned with their nanowire parallel along the strong field axis. In this way, not only the subband physics, requiring strong fields due to the narrow nanowire cross sections, could be accessed. In the same cooldown, the Josephson junctions could be characterized as well, with perpendicular magnetic fields of much lower required magnitudes.

The cooling mechanism of ^{3}He/^{4}He dilution refrigerators relies on the finite

solubility of ^{3}He in liquid ^{4}He at very low temperatures. Exploiting the cooling resulting from dilution of ^{3}He by ^{4}He in this temperature range was first proposed in 1962 by London, Clarke and Mendoza [90]. Below 870 mK, ^{3}He/^{4}He-mixtures undergo a spontaneous phase separation [91]. Due to the fact that inside a liquid mixture of both isotopes, ^{3}He behaves like a Fermi gas, its Fermi energy rises with the particle number due to the Pauli principle. Thus, a temperature dependent upper boundary for energetically favorable relative concentrations exists. Even at zero temperature, an arbitrarily concentrated mixture of at least 6.5 % ^{3}He separates into a pure ^{3}He phase and a mixture of 6.5 % ^{3}He in ^{4}He [92], and therefore, there is no theoretical lower temperature limit of this technique. When ^{3}He is pulled from the mixed phase, it will be substituted from the pure phase, and this expansion of new ^{3}He into the dilute mixture is thermodynamically equivalent to evaporative cooling used in simple ^{4}He refrigerators.

The phase separation of ^{3}He and ^{4}He takes place in the so-called mixing chamber, which is in direct thermal contact with the sample in order to cool it down to the lowest possible temperatures. The key to the continuous operation lies in the steady extraction of ^{3}He from the mixed phase. The mixed phase being denser than the pure ^{3}He phase and thus settling below it, a tube reaches down from the top, providing a path in a drinking straw like manner to the so-called still above.

3.3.2 MEASUREMENT CONTROL AND DATA ACQUISITION

Most data acquisition in the low-temperature measurements was done using standard lock-in amplifiers, e.g. *NF Instruments LI5645, LI6540, Stanford Research Systems SR830, EG&G Instruments 7260*. Bias currents, voltages and gate voltages were applied using DC sources, e.g. *Keithley 2400, 2450*. The equipment was controlled via GPIB or LAN, using the *QCoDeS* package for *Python* or custom *LabView* programs. Most of the non-superconducting measurements were operated through the all-in-one measurement device *Nanonis Tramea*.

Additionally, during this work, extensions to the *Qcodes* package were written in *Python*, which substantially facilitate setting up both simple and elaborate

measurements, reduce error rates and thus shorten machine time.

The connection to the devices, between the top plate of the cryostats and measurement equipment is made by a doubly shielded 24-pin cable with *Fischer* connectors, which is split up through a breakout box into 24 BNC connectors, which are individually connected with commercial BNC cables through further circuits in separate metal boxes to the lock-in amplifiers.

Lock-in measurements. Lock-in amplifiers supply and measure oscillating signals at a steady frequency and are especially useful when it comes to measurements with very low signal-to-noise ratios. Stemming from first experiments in the 1930's [93], they are among the most widely used measurement equipment in low-frequency physics experiments nowadays. Key concept is feeding a precisely oscillating signal to the measurement, and analyzing the returning signal in the most narrow frequency window possible around the same frequency (in some cases with respect to its harmonics), measuring amplitude and phase or in-phase and out-of-phase components. Since this homodyne detection involves mixing the measured signal with the carrier signal, it is basically an extremely sharp extraction of the signal of interest from a potentially large amount of all kinds of noise.

The Tramea system. *Nanonis Tramea* is an all-in-one transport measurement system. It is equipped with 8 inputs and 8 outputs that can measure or provide voltages between $-10\,\mathrm{V}$ and $10\,\mathrm{V}$, with a dynamic range of $120\,\mathrm{dB}$, resulting in a resolution of roughly $20\,\mathrm{\mu V}$. It is controlled by its own software which allows an uncomplicated approach to multi parameter sweeps and measurements at short timescales down to milliseconds. The resistance measurements for the normal state characterization of nanowires was done with the lock-ins emulated by its software, with a current-biased wiring of the devices.

Current-biased measurements. Resistance measurements in normal and superconducting state as well as Josephson junction measurements were wired in a current-biased setup. The output signal of the lock-in amplifier which oscillates at a set frequency and voltage amplitude first passes through a large and a small resistor, then through the sample and sinks into ground. The large resistor (e.g. $10\,\mathrm{M\Omega}$) being orders of magnitude more resistive than the sample, causes

a current to pass through the device that oscillates at an approximately constant amplitude. The resistance of the sample creates a voltage drop across its contacts which is the signal to be measured (and demodulated) by the lock-in amplifier input. Similarly, the voltage drop on the small resistor (e.g. $1\,k\Omega$) can be used to monitor the current.

For differential measurements, such as the differential resistance of a Josephson junction, a bias current is needed to offset the constantly oscillating current signal. It is generated using a DC voltage source and passes a large resistor (e.g. $1\,M\Omega$) for the same purpose of conversion to a current bias. Both signals are mixed in parallel to the sample which causes the oscillating and the bias current to add up. For obtaining I-V curves, this data is integrated over the current, and the differential conductance data can be calculated via subsequent derivation with respect to voltage.

Voltage-biased measurements. Tunneling spectroscopy measurements were conducted in a voltage-biased configuration. The oscillator output of the lock-in amplifier as well as the voltage bias from the DC source now pass voltage dividers and are scaled down by a factor (e.g. x1/1000). Both voltage dividers share the same grounded resistor and have their middle point connected to the sample. Since the resulting currents to ground add up, the sum of the voltage drops over the grounded resistor, hence the sum of the oscillator and the bias signal pass to the sample.

4

VLS-Growth of $(Bi_{1-x}Sb_x)_2Te_3$ and $Bi_2(Te_xSe_{1-x})_3$ nanowires

The nanowires grown and measured in this work were grown by the Vapor-Liquid-Solid (VLS) process out of the ternary TIs $(Bi_{1-x}Sb_x)_2Te_3$ (BST) and $Bi_2(Te_xSe_{1-x})_3$ (BTS). In the following sections, first, both materials are introduced and elaborated on in terms of how they can be made bulk-insulating. Secondly, the VLS growth technique and equipment are described, and the detailed working steps are shown. Lastly, characterizing transport measurements in the normal state are shown.

4.1 Topological Insulators out of Bi, Sb, Te and Sb

From the building blocks Bi, Sb, Te and Se, a number of different TI materials can be composed. The first one among these to be predicted in 2007 [46] was $Bi_{(1-x)}Sb_x$, which was experimentally confirmed only a year later [94], becoming the first known three-dimensional TI [95]. In 2009, first-principles calculations lead to the prediction that the binary compounds Bi_2Te_3, Bi_2Se_3 and Sb_2Te_3 should

also be TIs (whereas the remaining combination Sb_2Se_3 is not) [96]. Apart from featuring a single Dirac cone at the Γ-point in the Brillouin zone, the non-trivial gap of Bi_2Se_3 was estimated to be as large as 300 meV. In the same year, all three compounds were confirmed to be TIs and their gapless surface states were shown in ARPES measurements [43, 97–99].
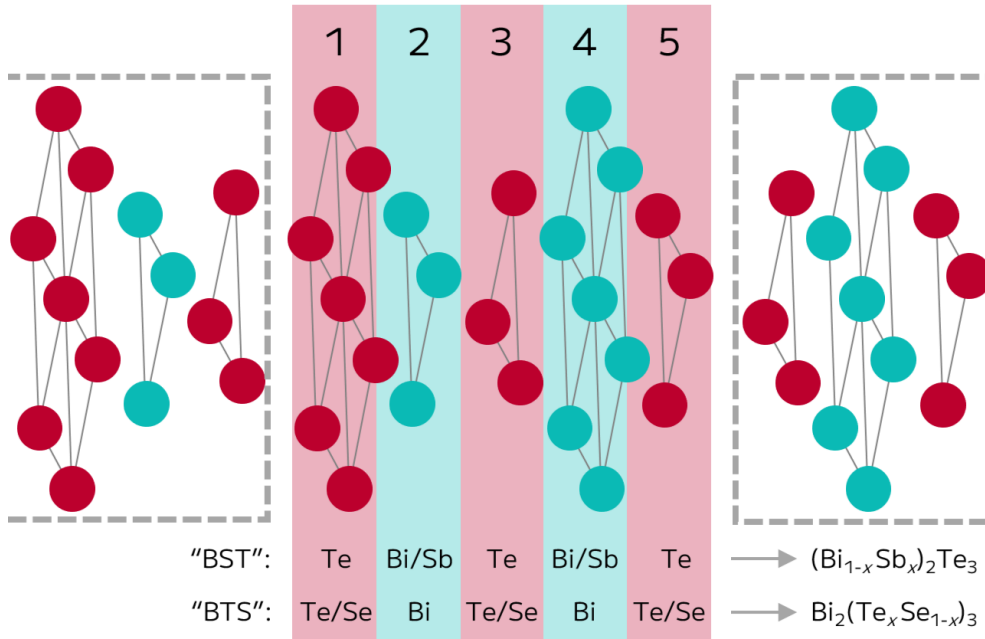
Figure 4.1: **Schematic of the tetradymite crystal structure.** *The covalently bonded quintuple layers, made out of 5 hexagonal lattice planes, are stacked with van der Waals bonds. The positions 1, 3 and 5 within a QL are occupied by Te or Se, the positions 2 and 4 with Bi or Sb.*

Bi_2Te_3, Bi_2Se_3 and Sb_2Te_3 (and Sb_2Se_3) crystallize in the tetradymite structure, which is a layered crystal structure out of hexagonal lattice planes (see Figure 4.1) with the space group $R\bar{3}m$. The planes consist of either of both elements in alternating sequence, and are stacked in quintuple layers with covalent bonds, e.g. in the sequence Te-Bi-Te-Bi-Te, in the case of Bi_2Te_3. The quintuple layers are then stacked again and held together by van der Waals interaction. This is a convenient aspect for the crystal growth of these materials, because the repeatedly occurring weaker van der Waals bonds make it possible to grow single-crystalline structures in conditions where the crystal seed structure is not

well-defined, such as in the case of the VLS growth on SiO_2 substrate surfaces that are decorated with Au nanoparticles and host potential residues of the Au buffer solution (see Section 4.6 for details on substrate preparation and Section 4.4 for an introduction to the VLS growth technique).

When it comes to the electrical properties, these binary compounds per se are not ideal candidates for TI experiments, because of their natural tendency to form crystal defects resulting in conductive samples. Bi_2Te_3 and Bi_2Se_3 predominantly grow n-type and Sb_2Te_3 p-type [4, 100]. There are many approaches to encounter this issue, such as annealing Bi_2Te_3 in Te atmosphere [27], Cd- [101], Ca- [102] or Sb-doping Bi_2Se_3 [26, 49, 50] and the respective adsorption or heterostructures [103, 104]. Furthermore, very good charge compensation can be achieved by growing $BiSbTeSe_2$ or $(Bi_{1-x}Sb_x)_2(Te_ySe_{1-y})_3$ from all four of the binary building blocks [105]

This thesis focuses on the synthesis of two ternary compounds out of this family of materials, $(Bi_{1-x}Sb_x)_2Te_3$ and $Bi_2(Te_xSe_{1-x})_3$. In the following sections, their specific mechanisms of compensating and preventing charge carrier donation are explained.

4.2   "BST" - $(Bi_{1-x}Sb_x)_2Te_3$

$(Bi_{1-x}Sb_x)_2Te_3$ is a crystalline mixture between Bi_2Te_3 and Sb_2Te_3. As it can be seen in Figure 4.1, Te constitutes layers 1, 3 and 5 of each quintuple layer, while Bi and Sb share layers 2 and 4. Bi_2Te_3 has a natural tendency to grow n-type and Sb_2Te_3 p-type. From these two binary compounds, a ternary compound can be grown, in which the Bi:Sb ratio can be adjusted such that the charge carriers are compensated, and low charge carriers can be obtained [21, 23, 100, 106]. When grown by the VLS method, bulk-insulating samples can be obtained by the same principle. In this work, this was done by the fine-tuning the contribution of the two binary source materials Bi_2Te_3 and Sb_2Te_3. However, it must be noted that Sb_2Te_3 was reported to have a significantly faster oxidization rate than Bi_2Te_3 and Bi_2Se_3 [107, 108].

4.3 "BTS" - $BI_2(TE_xSE_{1-x})_3$

$Bi_2(Te_xSe_{1-x})_3$ nanowires can be grown very similarly by the VLS process [109], but the mechanisms to make the material bulk-insulating are different. From this TI material, resistivities higher than $1\,\Omega cm$ have been reported in bulk samples [110]. Given the fact, that Bi_2Te_3 and Bi_2Se_3 both grow naturally n-type, a charge compensation similar to the case of $(Bi_{1-x}Sb_x)_2Te_3$ cannot be expected. However, under favorable conditions, the following mechanisms may reduce the occurence of crystal defects when the elements are combined close to the mixing ratio $Bi_2Te_2Se_1$, being one of the candidates raising expectations for being able to be grown as a truly insulating TI [111]. The stacking sequence Te-Bi-Se-Bi-Te within a quintuple layer makes the occurrence of the most typically occuring defects, Se-vacancies in Bi_2Se_3 and Bi-Te antisite defects in Bi_2Te_3, less likely to occur. Se has a higher electronegativity than Te, and being enclosed within the two Bi layers helps to prevent Se vacancies, and at the same time counteracts the tendency to form Bi-Te antisite defects [4, 112]. In terms of oxidization, Bi_2Te_3 and Bi_2Se_3 were reported to be rather unaffected from oxygen and water exposure [113].

4.4 VLS: THE VAPOR-LIQUID-SOLID GROWTH PROCESS

Vapor-Liquid-Solid growth is a process based on nanoparticles used as catalysts to the formation of thin nanowires out of evaporated source materials [114, 115]. In 1964, Wagner and Ellis [116] described this process, growing Si whiskers from Si vapor using Au nanoparticles. Observing that the grown whiskers had a small globule at their tip, and had grown at temperatures at which the Au was not expected to become liquid, they understood the catalytic mechanism of the nanoparticles. The evaporated source material is absorbed by the Au nanoparticles, forming a liquid alloy with a lower melting point and becoming a preferred site for the deposition from the vapor. Under ongoing absorption of source material, the droplets become oversaturated and the source material precipitates and solidifies, forming a nanowire underneath the catalyst, which is then lifted up by the growing pillar

underneath.

This growth technique is generally carried out in tube furnaces with one or multiple thermal zones equipped with a vacuum pump and a mass flow-meter, providing an adjustable flow of inert gas. Key ingredient is a thermal gradient, enabling the source material to sublimate in the hotter zone and to alloy with the catalysts on the substrates in the less hot zone. This entails that the gas flow must be injected on the hotter side while the vacuum pump is connected on the colder side. Source materials are placed at specific locations within the resulting temperature gradient, at temperatures that do not exceed their respective melting point. In general, the source materials are used in the form of ground powder, providing them with a high surface to mass ratio.
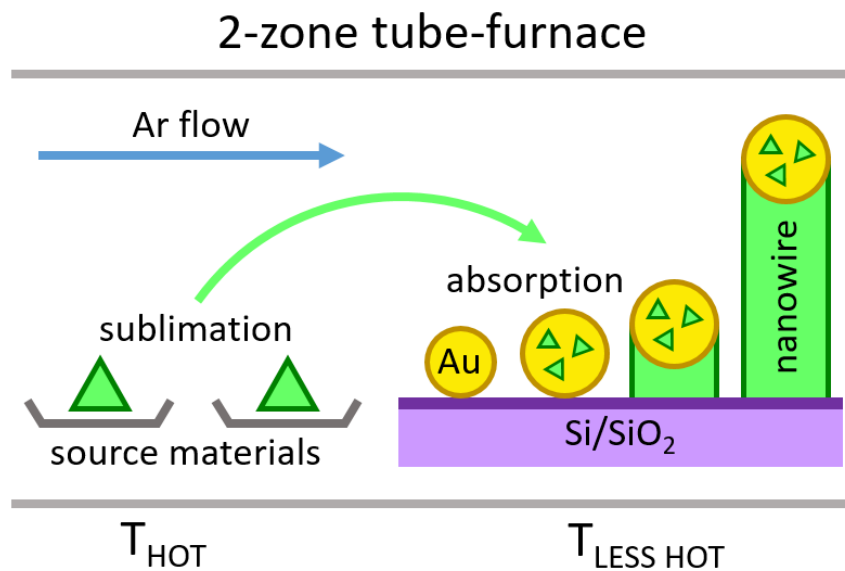
Figure 4.2: **Schematic of the Vapor-Liquid-Solid (VLS) nanowire growth process.** *The source materials are placed in the hotter side of the furnace and sublimate (**Vapor**), which is transported by the Ar gas flow to the growth substrates decorated with Au nanoparticles as catalysts. These are placed in the colder side of the furnace, which is hot enough such that the Au-source-material-alloyed nanoparticles melt (**Liquid**). With successive source material arriving and being solved in the alloy, it precipitates to the interface and builds a nanowire pillar underneath (**Solid**).*

The sublimated source materials (= vapor) are transported by the inert gas

flow towards the substrates located in the less hot side of the furnace tube. When the source materials reach the Au nanoparticles, they start to alloy and form a liquid droplet (= liquid) due to the lower melting point of the alloy of Au and source materials. Ongoing exposure of the Au nanoparticles to the incoming vapor causes the droplets to absorb more source material until the liquid alloy reaches oversaturation. Subsequently, the excess source material accumulates at the boundary to the substrate and solidifies (= solid). Given the right conditions, this process continuously creates a pillar that grows into a nanowire, lifting up the droplet which stays at the tip.

4.5 GROWTH SETUPS

Two furnace setups were used for the VLS growth of the nanowires. A larger furnace with a quartz glass tube of 50 mm diameter (Figure 4.4, and a smaller furnace with a tube diameter of 30 mm (Figure 4.3. Both are equipped with two thermal zones with individual heaters and thermocouples, that are individually addressed through the control module. A growth program consists of a set of tuples for both zones, each containing a time interval and a temperature setpoint. In a nutshell, based on the specified time intervals, the temperature setpoints are targeted and feedback is gained through the thermocouples. Between adjacent setpoints, the transition is interpolated linearly, resulting in smooth temperature changes with roughly constant rates. In a 2-zone build, one temperature can be used for the sources, one for the substrates. Variations in temperature for individual sources or substrates are achieved by placing these precisely along the arising thermal gradient with the help of a ruler. For both furnaces, the 0 mm mark of the ruler was placed at the center of the thermocouple of the left zone.

The inert Ar gas is introduced on the hotter (left) side and pumped out on the colder (right) side. The flow of Ar is controlled through a mass flow meter at a constant rate through the entire growth process. In the 50 mm furnace setup, an additional PID-controlled butterfly valve (a system made in the institute) throttles the pump line in order to maintain the pressure constant at the set value, gaining
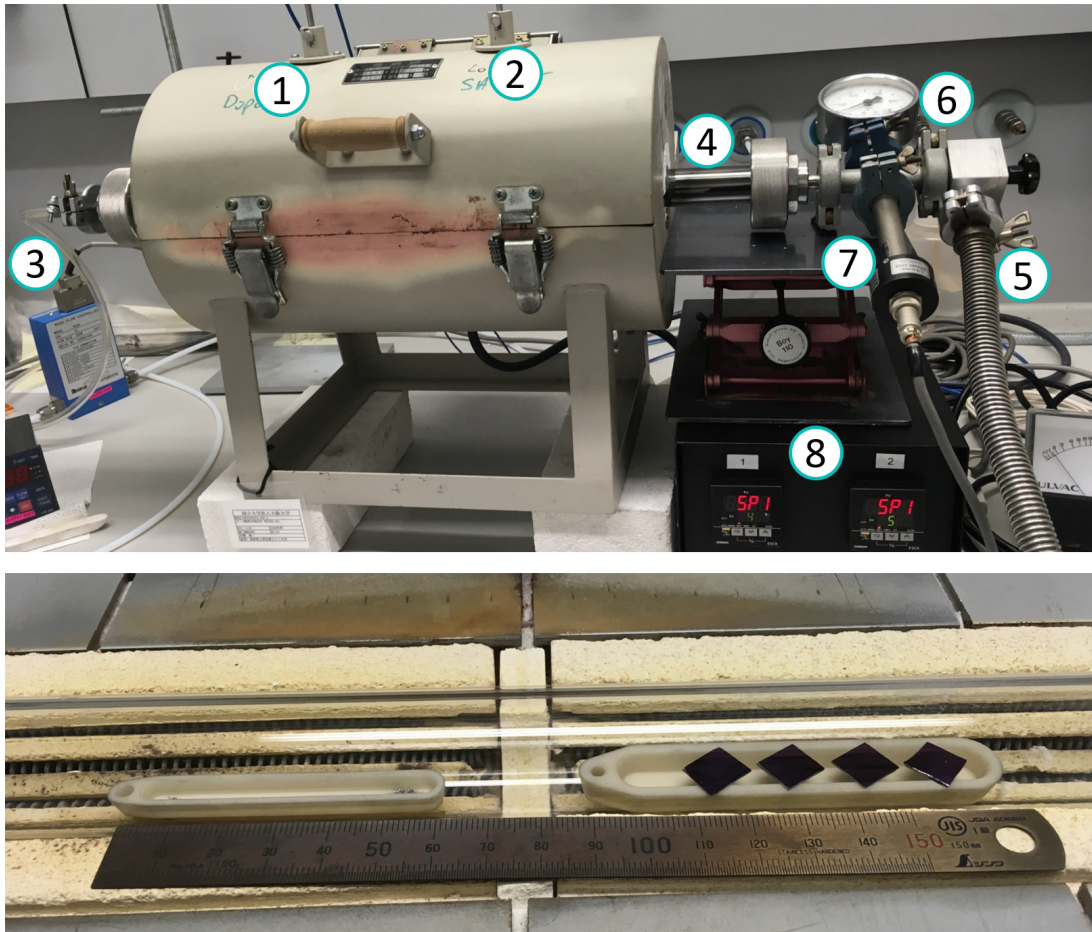
Figure 4.3: **30 mm tube furnace setup.** *Sources are placed in the hotter (1) and substrates in the colder (2) temperature zone. Ar, controlled by a mass flow meter (3), flows from left to right through the* 30 mm *quartz glass tube, where it is vacuum pumped out of the system (5). During loading, the left flange must be removed and the vent valve (6) is used to continuously flush the quartz tube with* N_2*, minimizing introduced air and humidity. Pressure gauge (7) and heater controller (8).* **Below:** *Opened furnace tube view with source materials and substrates placement with* Al_2O_3 *boats.*

feedback through a pressure gauge.

In order to load or unload samples, the entire flange must be removed from the Ar inlet side, causing a brief venting of the quartz glass tube. To minimize the resulting contamination by air and the accumulation of humidity at the quartz tube wall, an additional Ar (50 mm tube furnace) or N_2 (30 mm tube furnace)

vent valve is included on the pump side, such that the tube can be continuously flushed while the tube is open. Note that evidently, the furnaces cannot be baked again after loading sources and substrates.
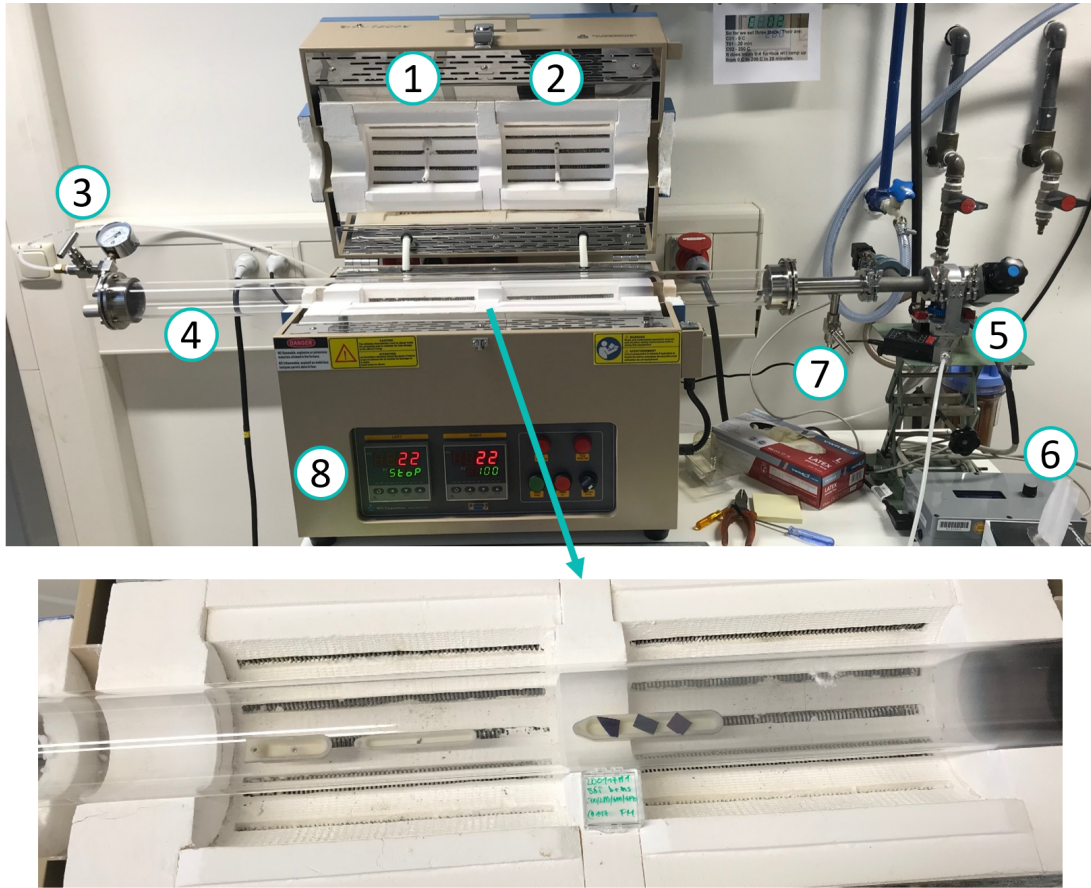
Figure 4.4: **50 mm tube furnace setup.** *Sources are placed in the hotter (1) and substrates in the colder (2) temperature zone. Ar, controlled by a mass flow meter (3), flows from left to right through the 50 mm quartz glass tube (4), where it is vacuum pumped out of the system. By throttling the pump line, the butterfly valve (5) regulates the pressure during growth with the help of a pressure gauge and a custom built PID controller (6). The vent valve is connected to an Ar line (7), enabling minimization of introduced air and humidity during loading. Heater controller (8).* **Below:** *Opened furnace tube view with source materials and substrates placement with Al_2O_3 boats.*

4.6 Substrate preparation

Si/SiO2 substrates (0.5 mm B-doped Si, 290 nm thermally grown SiO_2) are broken into rectangles of an approximate size between 8 x 12 mm and 15 x 20 mm with the help of a diamond tipped engraving pen. These are cleaned by strong ultrasonication at 37 kHz in acetone and isopropyl alcohol for 4 min each. Subsequently, organic residues are cleaned off the substrates in a UV-ozone-cleaner for 2 min. Within a short period of time, while the freshly cleaned surfaces are still hydrophilic, the substrates are dipped into Poly-L-Lysine solution *Sigma-Aldrich* for 2 s and blown dry with an N_2 gun. The same dip-and-dry procedure is repeated with a 20 nm Au nanoparticle solution in citrate buffer *Sigma-Aldrich*. Until usage, the substrates are stored in individual sample boxes in order to prevent contamination of the surfaces and mutual damaging resulting in Si dust promoting further damage.

4.7 Coarse- and fine-tuning of material composition

The objective is to find wide and robust growth windows that enable to change the nanowire composition, without having to find entirely new sets of parameters every time. In this way, the electronic properties of the nanowires can be tuned with the purpose to obtain bulk-insulating nanowires while opting for the highest possible crystal purity and well-shapedness of the nanowires.

In most cases, in a robust growth window, nanowires can be found on many locations of the substrates. This is because the vapor and substrate temperatures and the local source material flow depends on the locations in the tube as well as on the location within the substrate (e.g., hot- or cold-side-facing edge, corners, center, …). Furthermore, this natural variation of parameters enables to deduce parameter adjustments that seem promising to improve the growth for the next cycle.

In the absence of an established recipe, when growing nanowires from Bi, Sb, Te and Se, which all start to sublimate at comparably low temperatures and are partly interchangeable within their tetradymite structure, three main stages

of optimization can be recommended. Firstly, finding a coarse parameter range in which growth is taking place on the substrates through the Au catalysts. Secondly, narrowing the parameters down to obtain the desired shape of nanowires, while approaching the required ratio of elements for the tetradymite structure, namely a 2:3 ratio between the total of Bi and Sb on the one side and the total of Se and Te on the other side. Thirdly, fine-tuning the precise ratio within the interchangeable elements, such that the charge carrier compensation can be maximized. By fine-tuning the Bi/Sb ratio for BST and the Te/Se ratio for BTS, bulk-insulating nanowires can be grown.

4.8 GROWTH RESULTS: $\left(\text{Bi}_{1-x}\text{Sb}_x\right)_2\text{Te}_3$ NANOWIRES ON SiO$_2$

Out of many performed VLS growth cycles, two recipes are explained here in detail. They represent two different approaches to the trade-off between cleanliness of the growth equipment with pristine source materials versus an equilibrium state of a coated furnace interior with source materials that have already been baked out. The latter inspired to mount additional N$_2$ vent valves to the furnaces, which enable the continuous flushing of the tube with nitrogen while it is opened for loading, minimizing contamination. These are useful even if a furnace was baked out, because it must be opened again to load the source materials and substrates. After loading, it cannot be baked out anymore.

Growth A is the hotter approach that works with cleanly baked out equipment, Growth B is the colder approach and must be carried out with a more equilibrated state of equipment. Both yield bulk-insulating nanowires with diameters down to 30 nm, which likely show gate-dependent resistance oscillations and AB-like oscillations. Superconductivity was successfully induced in nanowires out of both growth recipes (see Chapter 6).

4.8.1 GROWTH A: THE ONE-SHOT (30 MM TUBE)

This $(\text{Bi}_{1-x}\text{Sb}_x)_2\text{Te}_3$ nanowire growth is performed in the 30 mm tube furnace, which was baked out beforehand at a temperature of 800 °C including the boats. The growth program consists of ramping up the temperatures to $T_1 = 570$ °C and $T_2 = 420$ °C during 60 min and constant temperature period of another 60 min until the heaters are switched off and the furnace is let to cool down naturally, with the lid closed, which takes approximately 3 h. A constant flow of inert Ar gas is set at 300 sccm during the entire process, resulting in a pressure of 2.5 mbar.

Taking into account the locations of the source materials within the furnace tube, the 6.4 mg of Sb$_2$Te$_3$ powder at $z = -60$ mm are heated to 508 °C, and the 7.1 mg of Bi$_2$Te$_3$ powder at $z = 0$ mm are heated to 561 °C. Substrates 1, 2 and 3, taken for Device 1, Device 4 and Device 3, placed at $z = 153$ mm, 166 mm and 178 mm, are heated to an effective temperature of $T = 435$ °C, 430 °C and

426 °C, respectively. These comparably high temperatures (compared to Growth B in Section 4.8.2) cause a higher evaporation rate of the source materials and a lower absorption rate in the Au nanoparticles. In this way, the source material feed in the liquid Au alloy droplet is roughly comparable, but this growth can be run in a clean baked-out furnace tube and boats. Figure 4.5 shows SEM images from the three growth substrates with the respective material composition by EDX in the inset, as well as a visualisation of the growth parameters and furnace positioning details.
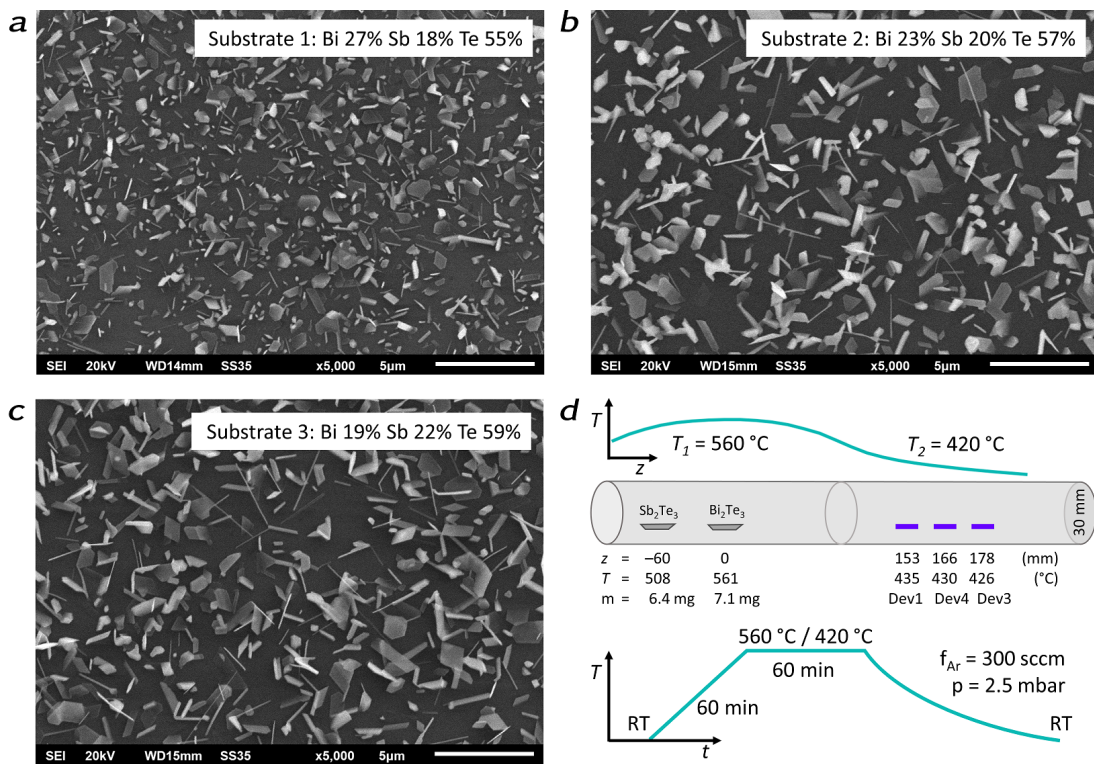
Figure 4.5: **Growth A: results and parameters. a-c** *SEM images of substrates 1-3, relative composition measured by EDX (atomic %) in the inset. The Sb:Bi ratio increases from x = 0.40 to 0.47 and 0.54 with substantial nanowire growth and increasing nanowire length across the substrates. Neighboring structures are micro crystals and flakes revealing shapes of hexagonal sheets. **d** Growth parameters and device association. Upper part shows the furnace tube with the respective locations and effective temperatures of sources and substrates. Lower part illustrates the growth program timeline.*

4.8.2 Growth B: the pre-cycled (50 mm tube)

This $(Bi_{1-x}Sb_x)_2Te_3$ nanowire growth is performed in the 50 mm tube furnace, which is pre-cycled with source materials in 5 cycles of the same recipe. The temperatures are heated up within 60 min to $T_1 = 510\,°C$ and $T_2 = 280\,°C$, kept constant for another 60 min and ramped down to room temperature within 30 min. The last step lets the cooling process commence in a controlled and smoother way compared to simply switching the heating off as in Growth A. However, after a few minutes, the set temperature lies below the real temperature inside the furnace and the natural cooling down process takes over, which lasts approximately 4 h.

Figure 4.6 shows SEM images of the nanowires grown on the two substrates with EDX-measured material composition in the insets, as well as the precise growth parameters and a timeline of the program. A high-resolution TEM image of the crystal structure is shown in Chapter 5. The effective temperatures and masses of the source materials are 512 °C and 3.6 mg for Sb_2Te_3 and 496 °C and 21.0 mg for Bi_2Te_3. Substrates 1 and 2, the latter taken for fabrication of Device 2 (TiVTiAl Josephson junction in Section 6.2), are placed at $z = 124$ mm and $z = 137$ mm and are heated to an effective temperature of $T = 367\,°C$ and $T = 347\,°C$, respectively.

a

b

Substrate 1: Bi 25% Sb 16% Te 59%

Substrate 2: Bi 20% Sb 21% Te 59%

SEI   20kV   WD17mm   SS34   x5,000   5µm

SEI   20kV   WD17mm   SS34   x5,000   5µm

c

$T_1 = 510\,°C$ $T_2 = 280\,°C$

Sb_2Te_3 Bi_2Te_3

z	=	−55	15		124	137	(mm)
T	=	512	496		367	347	(°C)
m	=	3.6 mg	21.0 mg			Dev2	

d

510 °C / 280 °C   1 + 4x pre-cycled
60 min f_{Ar} = 600 sccm
 p_{PID} = 15 mbar

T

RT

60 min

30 min

RT   RT

t
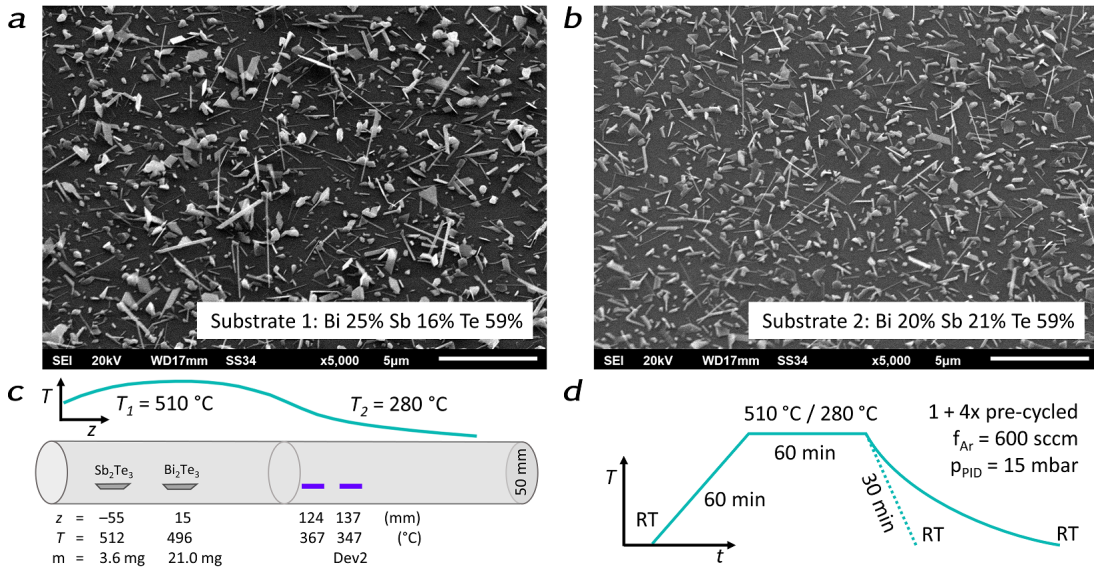
Figure 4.6: **Growth B: results and parameters. a, b** *SEM images of substrates 1 and 2, relative composition measured by EDX (atomic %). At precisely these parameters, both substrates show a significant nanowire growth while the Sb:Bi ratio increases from $x = 0.39$ to 0.51. Neighboring structures are micro crystals and flakes revealing shapes of hexagonal sheets.* **c, d** *Furnace placement schematic with device association and growth program sequence, with parameters. High-resolution TEM image of this growth available in Chapter 5.*

When comparing the temperatures of sources and substrates to Growth A, one may find that most of these are lower in Growth B. For the Bi_2Te_3 source this means an approximately 3 times lower vapor pressure [117], which is accounted for by increasing the mass. Furthermore, to increase the amount of source material settling down on the growth substrates, they are placed at lower temperatures, and the pumping efficiency is throttled. A PID-controlled butterfly valve is set to maintain 15 mbar of pressure. While the net throughput of the 600 sscm Ar-flow with respect to the larger tube is only 30 % lower than in the case of Growth A, throttling the pump and increasing the pressure by a factor of 6 significantly slows down the gas flow.

Nonetheless, the furnace tube as well as the boats need to be in a more equilibrated, pre-coated state, which is done by pre-cycling the furnace interior with the same procedure 5 times. After a preliminary bake-out at 800 °C, the first

and second of these pre-cycles is done with freshly weighed source materials, the further cycles re-use the material from the second cycle, hence $1+4x$ in the figure caption of panel d. After finally loading sources and substrates and closing the furnace tube, it is evacuated with a turbo pump for at least 1 h before starting the program.

4.9 GROWTH RESULTS: Bi$_2$(Te$_x$Se$_{1-x}$)$_3$ NANOWIRES GROWN ON SiO$_2$

Although the Bi$_2$(Te$_x$Se$_{1-x}$)$_3$ nanowires grown during this work have not shown a charge neutrality point in the gating experiments yet, their relative change of resistance is similar to the (Bi$_{1-x}$Sb$_x$)$_2$Te$_3$ nanowires, such that the chemical potential lies likely within the bulk band gap. The AB-like oscillations measured in multiple Bi$_2$(Te$_x$Se$_{1-x}$)$_3$ nanowire devices are very well defined, outperforming the (Bi$_{1-x}$Sb$_x$)$_2$Te$_3$ nanowires presented in this thesis.

A possible explanation to this could be the different charge compensation mechanism in Bi$_2$(Te$_x$Se$_{1-x}$)$_3$ than in (Bi$_{1-x}$Sb$_x$)$_2$Te$_3$. In a nutshell, charge compensation in (Bi$_{1-x}$Sb$_x$)$_2$Te$_3$ can be achieved by matching the concentrations of positive and negative charge carriers originating from the naturally occurring defects in Sb$_2$Te$_3$ and Bi$_2$Te$_3$, respectively. This however does not mean that a (Bi$_{1-x}$Sb$_x$)$_2$Te$_3$ nanowire showing a charge neutrality point necessarily must also have a very low total concentration of charged defects. For Bi$_2$(Te$_x$Se$_{1-x}$)$_3$ however, one could make the argument, that if close to charge neutrality, it is more likely to have a low density of charged defects in total. This is based on the assumption that the naturally electron-doped Bi$_2$Te$_3$ and Bi$_2$Se$_3$ cannot simply compensate with positive and negative defects as in (Bi$_{1-x}$Sb$_x$)$_2$Te$_3$, but mutually help preventing the formation of their typically occurring anti-site defects and vacancies, respectively [4, 112]. While this is one reason for the difficulties to obtain fully bulk-insulating nanowires from Bi$_2$(Te$_x$Se$_{1-x}$)$_3$, it is also a possible argument for a higher sample grade, once highly bulk-insulating samples are grown.

4.9.1 $Bi_2(Te_xSe_{1-x})_3$ NANOWIRE GROWTH (30 MM TUBE)

Figure 4.7a shows an SEM image of the growth result, featuring comparably straight, stiff and thin nanowires, hexagonally layered flakes and micro crystals. The composition measured by EDX suggests $Bi_2Te_{1.5}Se_{1.5}$. Panel b is a high resolution TEM image of a nanowire, covering its entire diameter. The single crystalline structure appears uninterrupted and an amorphous oxide layer is barely recognizable. Panels c and d illustrate the growth parameters and instructions.
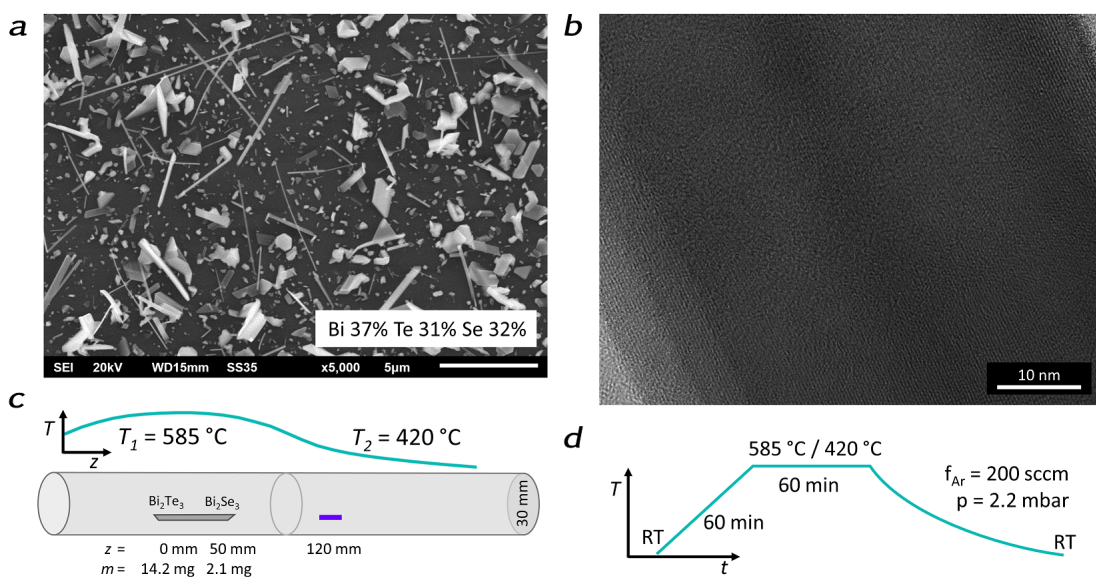
Figure 4.7: **$Bi_2(Te_xSe_{1-x})_3$ nanowires grown on SiO_2 in the 30 mm tube furnace. a** SEM image of the substrate showing thin and straight nanowires of lengths of up to 8 µm and widths below 50 nm, aside micro crystals and hexagonally layered flakes. **b** High-resolution TEM image covering the entire diameter of a nanowire. Although the optical axis could not be aligned exactly along any of the crystal axes, a single-crystalline structure is visible that extends over the entire observed section of the nanowire. **c, d** Parameters, illustration of furnace placement and growth program.

This growth can be performed with baked-out furnace tube and boats, but recurring growth and experiments suggested that repeating this recipe without baking out the equipment might provide a more equilibrated and homogeneous growth result. The powdery source materials of Bi_2Te_3 and Bi_2Se_3 are placed in the same boat, which must be long enough to allow their placement at $z = 0\,mm$

and 50 mm, respectively. The substrate is placed at $z = 12$ mm. With an Ar-flow of 200 sccm and a pressure of 2.2 mbar, the furnace temperatures are ramped up during 60 min to $T_1 = 585\,°C$ and $T_2 = 420\,°C$, held constant for another 60 min until the heaters are switched off and the furnace cools down naturally within 3 h.

4.9.2 AB-LIKE OSCILLATIONS

The AB-like oscillations measured in the Bi$_2$(Te$_x$Se$_{1-x}$)$_3$ nanowires grown during this work are well pronounced and their π-shift can often be seen without any need of background substraction. Figure 4.8a shows a prime example of 0- and π-shifted AB-like oscillations measured at different gate voltages. Although a resistive maximum at zero field is rarely observed, the further oscillation periods alternate clearly. The insets show the temperature dependence of the resistance during cooldown and the gating curve measured in both directions. The latter shows large fluctuations which are unlikely associated with resistance oscillations from subband crossings (as discussed in [1]), but are likely caused by impurity states. However, an oscillation of smaller amplitude seems to be contributing to the curve which would be consistent with the subband oscillations. The nested inset shows a magnified view on it, revealing that the π-shifted AB-like oscillations were measured at its minimum and maximum, respectively.

Figure 4.8b shows a colormap of more magnetoresistance curves out of which the AB-like oscillations were extracted by subtracting a Savitzky-Golay filtered background. The gate voltages, at which these were measured, are not equally spaced but narrower around values at which the transition between 0- and π-ABLO takes place, in order to investigate the transformation. Apparently, individual peaks shift gradually and sudden major changes occur in between. Thus, although the required alternation is present, in this case it is not simply a switching between both ABLO phases in the sense of a chess pattern, as expected by theory.
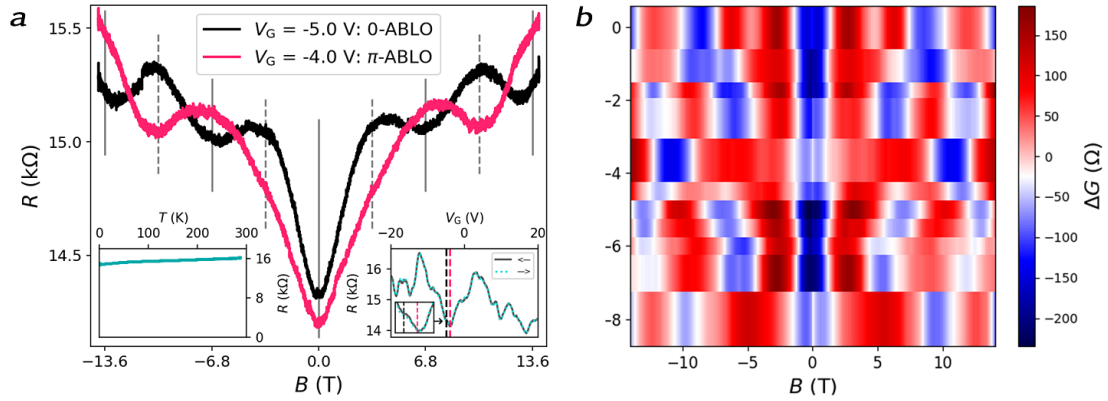
Figure 4.8: **AB-Like oscillations of a $Bi_2(Te_xSe_{1-x})_3$ nanowire device. a** 0- and π-AB-like oscillations measured at $V_G = -5\,V$ and $-4\,V$, respectively. No background subtracted. Left inset: $R(T)$-curve, right: gating curves in both sweep directions (dashed and solid curve) showing no hysteresis, with vertical dashed lines indicating the gate voltages at which the magnetic field sweeps were measured. The large fluctuations are likely due to impurities in the nanowire and shadow the less pronounced subband oscillations. A possible subband oscillation is shown in the nested inset, which would be consistent with the observed ABLO phase shift between magnetic sweeps measured at its maximum and its minimum. **b** Colormap of the extracted AB-like oscillations (background subtracted), measured at $V_G = 0, -1.2, -1.8, -2.1, -4, -4.5, -5, -5.5, -6, -6.5, -8\,V$. These non-equidistant voltages were chosen in order to track the transition between 0- and π-ABLO, which seems to occur not clearly but through a mixture of gradual shifting and sudden jumps of individual features.

5

Quantum confinement of the Dirac surface states in topological-insulator nanowires

5.1 Introduction

One of the main objectives for nanowire experiments is the emergence of size-related effects arising through the confinement to a narrow rod of material. In the case of TIs, the topological surface states that normally live on a flat surface, are now wrapped around a narrow cylinder. The question whether the surface states become quantized in the way it is theoretically predicted, is of large interest. It lays the foundation for a number of experiments, such as, among others, the realization of Majorana fermions in topological insulator nanowires. By the spatial constraint of one surface dimension to the narrow circumference of a nanowire, a discrete spectrum is obtained. These spin-non-degenerate sub-bands are key ingredient for the realization of Majorana bound states at the ends of the nanowire [3].

In this publication, resistance fluctuations were measured in normally conducting topological insulator nanowires, that appeared during changing the chemical potential via electrostatic gating. By building a theoretical model and simulating its effect on transport, it was found that not only the diverging density

of states at the flat bottom of each sub-band causes an effect on conductivity. While this sudden availability of conductive states causes an abrupt increase in conductivity, it also boosts the probability of scattering. In the weak scattering regime, it was found that the resistive peaks arise whenever the chemical potential touches a new sub-band.

5.2 CONTRIBUTION TO PUBLICATION AND ITS RELEVANCE IN THIS THESIS

Growth of nanowires, device fabrication and transport measurements were carried out by the author in cooperation with O. Breunig, D. Fan and M. Rößler and supervised by Y. Ando. The theoretical model for the gate-dependence of the topological surface state sub-bands, the electrostatic model and the scattering effects were built and established by H. F. Legg and supervised by A. Rosch. Transmission electron microscopy and energy-dispersive x-ray spectroscopy was performed by S. Roitsch. Figures and captions were contributed by all three first authors. The text sections were collaboratively written by all first authors, and supervised and finalized by Y. Ando.

Measuring the sub-band quantization of the topological surface states of topological insulator nanowires is a crucial foundation for the subsequent experimental work presented in this thesis. The basic assumption that the finite circumference of the nanowires in the nanometer scale causes a size-quantization for the electrons in terms of their angular momentum quantum number ℓ, is a foundation for a large number of research, and conceptual propositions in the field of topological quantum computation and spintronics. In this publication, the quantization was not only confirmed to arise in the grown nanowires, but also a growth recipe was developed and further insights were gained that enable the reproducible growth of bulk-insulating $(Bi_{1-x}Sb_x)_2Te_3$ nanowires. Furthermore, the previously ambivalent interpretation of fluctuations in transport measurements was led to a clearer picture such that promising nanowires and quantized sub-bands can be recognized by transport measurements. In the subsequent work, superconductivity

will be induced into the topological surface state sub-bands by the proximity effect. For this purpose, the understanding of the details of electronic transport as well as the identification and localization of the sub-bands in the measurements are of crucial importance.

Quantum confinement of the Dirac surface states in topological-insulator nanowires

Felix Münning [1,5], Oliver Breunig [1,5], Henry F. Legg [2,3,5], Stefan Roitsch[4], Dingxun Fan[1], Matthias Rößler [1], Achim Rosch [2] & Yoichi Ando [1✉]

The non-trivial topology of three-dimensional topological insulators dictates the appearance of gapless Dirac surface states. Intriguingly, when made into a nanowire, quantum confinement leads to a peculiar gapped Dirac sub-band structure. This gap is useful for, e.g., future Majorana qubits based on TIs. Furthermore, these sub-bands can be manipulated by a magnetic flux and are an ideal platform for generating stable Majorana zero modes, playing a key role in topological quantum computing. However, direct evidence for the Dirac sub-bands in TI nanowires has not been reported so far. Here, using devices fabricated from thin bulk-insulating $(Bi_{1-x}Sb_x)_2Te_3$ nanowires we show that non-equidistant resistance peaks, observed upon gate-tuning the chemical potential across the Dirac point, are the unique signatures of the quantized sub-bands. These TI nanowires open the way to address the topological mesoscopic physics, and eventually the Majorana physics when proximitized by an s-wave superconductor.

[1] Physics Institute II, University of Cologne, Zülpicher Str. 77, 50937 Köln, Germany. [2] Institute for Theoretical Physics, University of Cologne, Zülpicher Str. 77, 50937 Köln, Germany. [3] Department of Physics, University of Basel, Klingelbergstrasse 82, CH-4056 Basel, Switzerland. [4] Institute of Physical Chemistry, University of Cologne, Luxemburger Str. 116, 50939 Köln, Germany. [5] These authors contributed equally: Felix Münning, Oliver Breunig, Henry F. Legg. ✉email: ando@ph2.uni-koeln.de

In topological insulator (TI) nanowires[1–3], the quantum confinement of the electron motion along the circumferential direction is described by the angular-momentum quantum number ℓ. In zero magnetic field, this quantization leads to the gap opening at the Dirac point, and the sub-bands become doubly-degenerate (see Fig. 1a). When a magnetic flux Φ threads along the wire, the energy spectrum is modified in a nontrivial way as described by the following formula (under the simplified assumption of a circular wire cross-section):

$$E_\ell(k) = \pm \hbar v_F \sqrt{k^2 + \left(\frac{\ell - \eta}{R_w}\right)^2}, \quad \eta \equiv \Phi/\Phi_0. \quad (1)$$

Here, v_F is the Fermi velocity, R_w is the wire radius, and $\Phi_0 = hc/e$ is the flux quantum; note that ℓ takes half-integer values $\pm\frac{1}{2}, \pm\frac{3}{2}, \ldots$ due to a Berry phase arising from the spin-momentum locking of the TI surface states[1]. Interestingly, a spin-non-degenerate gapless spectrum is restored when Φ is a half-integer multiple of Φ_0; the spin-momentum locking in this gapless sub-band leads to the appearance of Majorana zero modes (MZMs) when the wire is proximitized by an s-wave superconductor[3,4]. The tunability of the spin-momentum locking with Φ makes the sub-bands described by Eq. (1) a particularly interesting platform for topological mesoscopic physics.

In experiments, to elucidate the peculiar quantization effects, the TI nanowire should be bulk-insulating and as narrow as possible, preferably less than ~100 nm. Past efforts for TI nanowires[5–16] have only been able to indirectly probe the quantized Dirac sub-bands, although bulk-insulating TI nanowires have been occasionally reported[12,16–21]. In this work, we employed the vapor–liquid–solid (VLS) method using Au nanoparticles as catalysts[5] and applied the concept of compensation, which has been useful for achieving bulk-insulation in bulk crystals[22,23]. Specifically, we tuned the Bi/Sb ratio of $(Bi_{1-x}Sb_x)_2Te_3$ nanowires to a value that yields the most insulating properties. Fabrication of gate-tunable four-terminal devices allows us to bring the chemical potential across the Dirac point, upon which we discovered unusual oscillatory behavior in the resistance near the Dirac point in very thin wires. This feature turns out to be the signature of the quantized Dirac sub-bands in TI nanowires as our theoretical calculations show.

Results

Structural and chemical analysis. During the VLS growth, the catalysts form a constantly over-saturated liquid alloy with the absorbed source materials, which then precipitate and form a crystal underneath. Using nominally-20-nm-diameter Au nanoparticles as catalysts, we obtain nanowires with a constant diameter between 20 and 100 nm, with a length of up to several μm (Fig. 1b). By using transmission electron microscopy (TEM) and energy-dispersive X-ray (EDX) analysis (Fig. 1c), we identify the Au catalyst at the tip of most of the analyzed nanowires. The wires are found to be surrounded by a ~4-nm-thick amorphous oxide shell. The selected-area diffraction patterns (SAED, Fig. 1c inset) indicate a high crystalline quality. We found hexagonal symmetry for a direction perpendicular the nanowire axis, which allows us to identify the growth direction to be $\langle 11\bar{2}0 \rangle$-type. The compositional analysis using EDX along the wire shows a constant stoichiometry $(Bi_{0.68}Sb_{0.32})_2Te_3$ in the nanowire core and no incorporation of Au was detected (See Supplementary Note 2).

Temperature and gate-dependent device resistance. In the following, we report five representative devices 1–5. The scanning electron microscope (SEM) picture of device 5 is shown in Fig. 1d, with its schematic depicted in Fig. 1e. The single-crystalline nanowires are most likely of hexagonal shape (see Supplementary Note 1). The resistance R vs. temperature T curves shown in Fig. 1f present both insulating and metallic
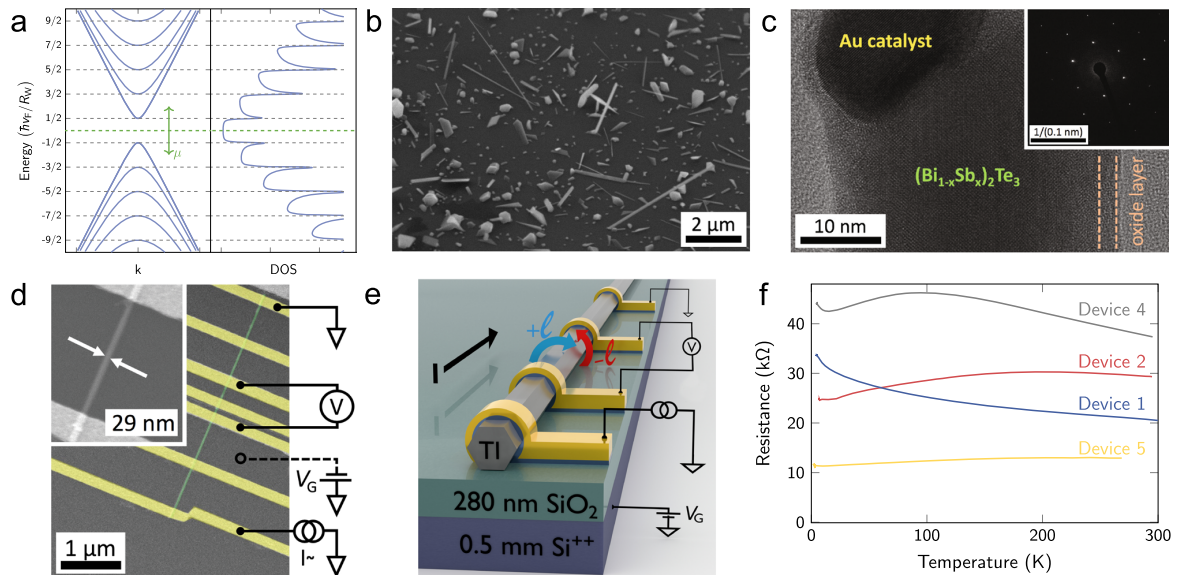
Fig. 1 Topological-insulator nanowire and its device. a The sub-band structure of quantum-confined TI surface states described by Eq. (1) (left) and corresponding density of states (right). **b** SEM image of nanowires (and other nanostructures) grown on a substrate. **c** TEM image revealing the single-crystalline nanowire body, the remainder of the 20 nm Au-nanoparticle growth catalyst, and a 4-nm thick oxide layer at the nanowire surface. The inset shows the SAED pattern taken in the c-axis direction. TEM image and SAED pattern were taken from different nanowires and directions. **d** false-color SEM micrograph of device 5 with the schematics of electrical wiring. Pt/Au leads are colored yellow, the nanowire is shown in green. The inset shows a magnified view of the nanowire. **e** Schematic 3D image of the device construction. Pt/Au leads are illustrated in yellow. The blue and red arrow illustrate the angular momentum ℓ. **f** $R(T)$ curves of devices 1, 2, 4, and 5.
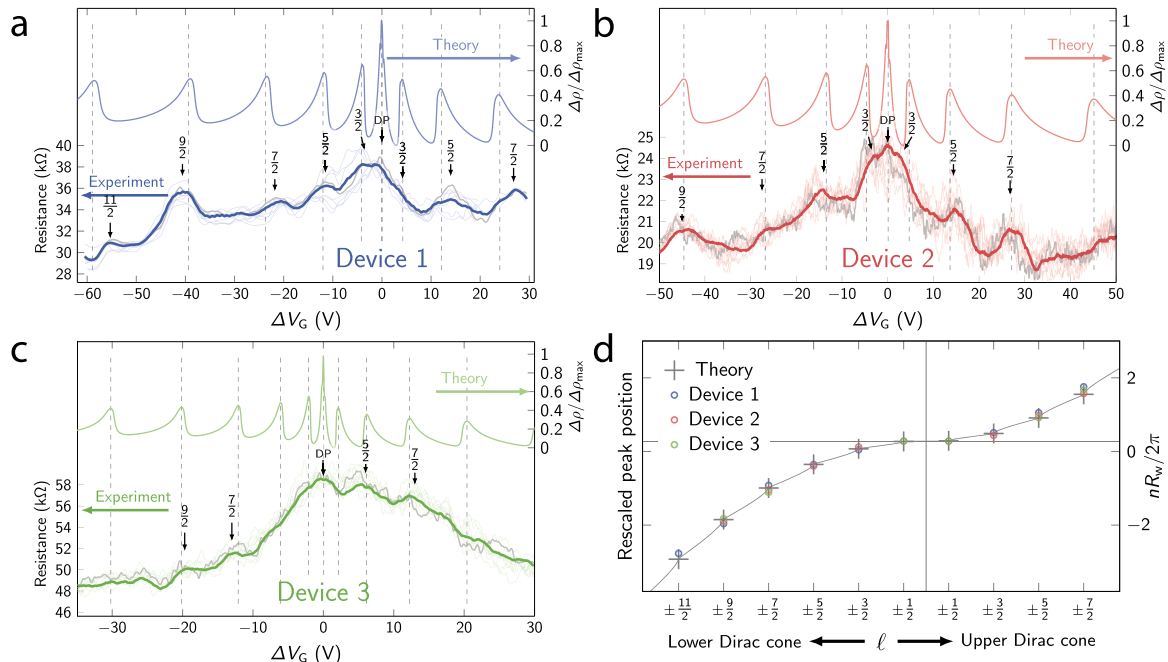
Fig. 2 Signature of sub-band crossings. In panels **a**-**c**, lower curves show the V_G dependence of R observed in devices 1-3 at 2 K; $\Delta V_G = 0$ corresponds to the Dirac point of the TI surface state, which was achieved with V_G of 30.5, 10, and 18.5 V in devices 1, 2, and 3, respectively. For each device multiple consecutive sweeps (9, 54, and 40 for devices 1, 2, and 3, respectively) were performed. For clarity, only 9 of these sweeps are shown for each device as thin lines, together with a single exemplary curve highlighted in bold gray. From the average (colored bold lines) large oscillations of type I are identified (see main text) which arise from the sub-band structure and the corresponding maxima are labeled by arrows. Oscillations of type II are smaller and differ between individual sweeps. Upper curves in **a**-**c** are the theoretically calculated resistivity with a small density of impurities, assuming that electron density n is proportional to V_G; we used R_w of 20, 16, and 20 nm, and C_G of 2.0, 2.2, and 3.6 pF/m for devices 1, 2, and 3, respectively. Pronounced maxima arise at sub-band crossings (dashed lines). **d** Rescaled position $\Delta V_G/V_0$ (see main text) of the resistivity maxima of the three devices (open circles) as a function of the quantum number ℓ compared to the theoretically calculated n in units of $2\pi/R_w$ (solid line). Crosses indicate the value of n at sub-band minima.

behavior; nevertheless, all these samples were bulk-insulating, which can be seen in their gate-voltage V_G dependences of R (Fig. 2a–c and Supplementary Fig. 4) showing a clear maximum, indicating that the Dirac point is crossed. The difference in the $R(T)$ dependence is most likely explained by a slightly different electron density n of the samples in the absence of gating ($n \approx 0.38, 0.14, 0.42, -0.2, 0.5$ nm^{-1} relative to the Dirac point, according to our analysis described later).

In the $R(V_G)$ traces, we found a hierarchy of fluctuation features. We observe semi-oscillatory features in the V_G dependence with the amplitude $A_I \approx 3, 2$ and 1 kΩ for devices 1, 2, and 3, respectively. We will show these features (type I) to be the signature of sub-band crossings. They are not universal conductance fluctuations (UCF) whose main fingerprint would be a strong change in magnetic field and the lack of any clear periodicity and a random amplitude. In contrast, the present features of type I occur in a regular fashion, i.e., at regularly spaced gate voltages and with a largely uniform amplitude. Further, they are robust in small applied magnetic fields (for a detailed discussion on UCF see Supplementary Note 3). The other type of fluctuations have the amplitude $A_{II} \approx 0.5$ kΩ (type II) and were changing with time (Supplementary Fig. 3). We speculate that they arise from time-dependent conductance fluctuations due to charge traps or mobile scattering centers, similar to those observed in metallic nanowires of similar mesoscopic size[24], but they may also be affected by the presence of electron-hole puddles[25–27]. Averaging over several gate-voltage sweeps suppresses type II fluctuations while type I fluctuations remain unaffected, see Supplementary Note 4.

Model of gate-voltage dependent surface conduction. We now discuss the main observation of this work, that is, the reproducible semi-oscillatory feature in the $R(V_G)$ curves. Due to the 1D nature of the energy bands in the nanowire, the density of states (DOS) diverges as $1/\sqrt{E}$ at each of the sub-band's edges as shown in Fig. 1a. This causes a sub-band crossing to have two contrasting effects on R: (i) The opening of a new conductance channel can decrease the resistivity as more charge can be transported. It can, however, also (ii) increase the resistivity by opening a new channel where electrons from other bands can scatter into. Thus, we have performed a straightforward theoretical calculation using an idealized model based on the surface state of a circular TI nanowire. (Small anisotropy effects arising both from the hexagonal shape of the wire and the anisotropic electrostatic environment are discussed in the Supplementary Notes 13–16). The effects of local impurities are taken into account using the T-matrix formalism and we find that the experimental data is best described by weak impurities (see Supplementary Note 11). In Fig. 3, we schematically show how different sub-bands contribute to the conductivity: When a new channel is added (Fig. 3b), all other channels scatter efficiently into the new channel and, as a result, the conductivity contribution of each channel drops. This is by far the dominant effect and leads to pronounced peaks in R even when several channels are present. The diverging density of states of the newly added channel (Fig. 1a) is the main reason why this effect is so large, but it is further enhanced by a matrix-element effect originating in the topological protection of the surface states (Supplementary Note 11).
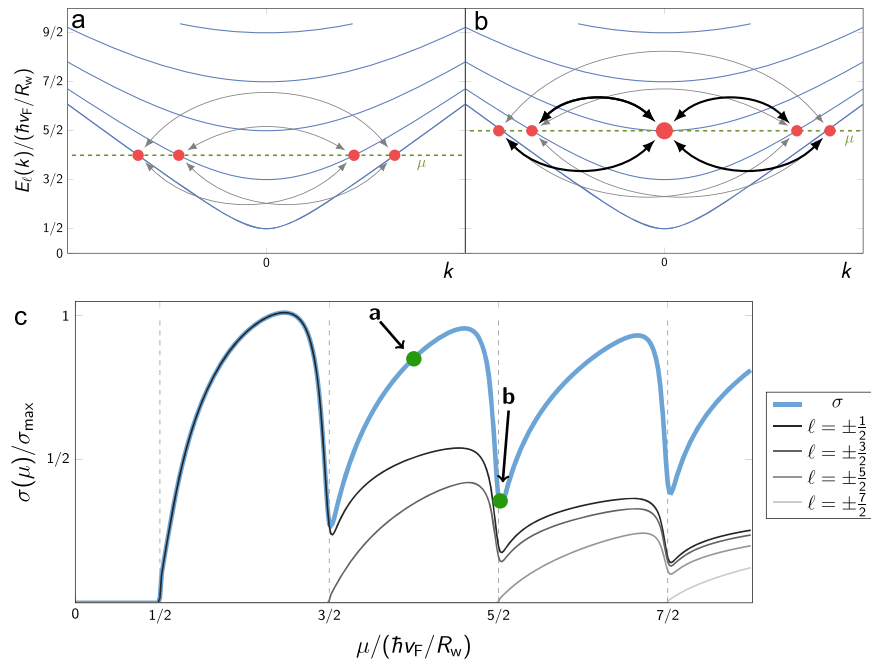
Fig. 3 Scattering processes and conductivity. a, b Scattering processes (arrows) between conduction channels for two positions of μ (dashed line). When μ is at the bottom of a sub-band, **b** all other sub-bands scatter at large rates (bold arrows) with the new sub-band due to its diverging density of states (illustrated by a large red dot), leading to a pronounced minimum in the conductivity. **c** Theoretically-calculated conductivity as function of μ (parameters as in Fig. 2). Thin black lines display the contribution of each sub-band labeled by $\ell = \pm\frac{1}{2}, \pm\frac{3}{2}, \pm\frac{5}{2}, \pm\frac{7}{2}$, which add up to give the total conductivity (thick blue line). The conductivity of all channels shows pronounced minima at $\mu = \ell\hbar v_F/R_w$, when the chemical potential touches the bottom of a new sub-band.

Hence, our calculations show that the resistance is expected to show a peak, each time a sub-band is crossed. This leads to equidistant peaks in Fig. 3, at $\mu = \ell\hbar v_F/R_w$, when the conductivity is plotted as function of the chemical potential μ. In the experiment, however, the gate voltage V_G, rather than μ, is varied and we observe a super-linear dependence of the spacings of the main peaks (neglecting features of type II). This originates from the fact that the effective capacitance of the nanowire devices (which dictates the V_G dependence of the accumulated charge) must be computed from their quantum capacitance C_Q and geometric (or galvanic) capacitances C_G in series where C_Q is proportional to the DOS[16]. In our experiment, C_G strongly dominates and the gate voltage directly controls the electron density n ($n \approx C_G \Delta V_G/e$, with ΔV_G measured from the Dirac point), rather than μ. This relation is used for the theory plots in Fig. 2. It also determines the peak positions indicated by dashed lines. We label the position of the peaks identified in the experimental data by the angular momentum quantum number ℓ of the added channel. The influence of the flat bottom gate geometry on the charge homogeneity around the wire is negligible, since it does not affect the position of peaks due to Klein-tunneling physics[16] (see Supplementary Note 13). When the chemical potential reaches the bottom of the first electron or the top of the first hole band ($\ell = \pm\frac{1}{2}$), the charge density is approximately zero in both cases and therefore there is only a single peak in the center for $\ell = \pm\frac{1}{2}$. For large ℓ, the peak position scales with ℓ^2, which is peculiar to the sub-bands of Dirac origin, where the charge density grows as μ^2 due to the 2D nature of the TI surface.

Sub-band crossings observed in experiment. It is striking that in Figs. 2a–c the theory can reproduce the essential features of our experiment, in particular the locations of the peaks in the

averaged $R(V_G)$ curves. While for devices 1 and 2 every peak can be indexed, type II features arising from disorder are more pronounced in device 3, such that some of the sub-band crossing features are not discernible despite averaging. To visualize the agreement between theory and experiment, we plot in Fig. 2d the rescaled gate voltage values of the peaks, $\Delta V_G/V_0$, vs the sub-band index ℓ, and compare it to the theoretically calculated electron density n at the peak position (in units of $2\pi/R_w$). In these units the rescaling factor is given by $V_0 = \frac{2\pi e}{R_w C}$, where C is the capacitance per length of the wire. The super-linear behavior in the V_G-dependent sub-band crossings and the excellent agreement of theory and experiment is a direct signature of the quantum-confined Dirac surface states, which is observed here for the first time.

It is prudent to mention that the quantum-confined sub-band structure of TI nanowires have been indirectly inferred[5–16] from the Aharonov–Bohm (AB)-like oscillations of R as a function of the axial magnetic flux Φ, which is due[1] to a periodic change in the number of occupied sub-bands at a given μ. In particular, the observation by Cho et al.[12] that R at $\Phi = 0$ takes a maximum when μ is near the Dirac point and changes to a minimum at some other μ was consistent with the gapped Dirac cone; however, the V_G dependence was not very systematic nor convincing in ref. [12]. A relatively systematic V_G dependence of R was recently reported for HgTe nanowires and was carefully analyzed[16]; unfortunately, the Dirac point of HgTe is buried in the bulk valence band, hindering the characteristic super-linear behavior in the ΔV_G vs ℓ relation from observation.

Discussion

The realization of very thin, bulk-insulating TI nanowires and the observation of the quantum-confined Dirac sub-band structure reported here is crucial for exploring the mesosocpic physics

— 73 —

associated with the topological surface states, not to mention their potential for future studies of MZMs. For example, the dependence of the spin degeneracy on the magnetic flux along the nanowires will give us a new tuning knob for mesoscopic transport phenomena, in which the spin-momentum locking can be varied. Also, it is an interesting insight that the charge inhomogeneity induced by gating on TI nanowires will not affect the energy locations of the sub-band crossings due to Klein-tunneling physics. Therefore, the new-generation TI nanowires realized here will open vast opportunities for future studies of topological mesoscopic physics including MZMs.

Methods

Nanowire synthesis. The $(Bi_{1−x}Sb_x)_2Te_3$ nanowires were synthesized by the VLS method using powders of Bi_2Te_3 and Sb_2Te_3 as starting materials in a two-zone 50-mm tube-furnace under a constant Ar flow. The Si/SiO$_2$ substrates were first decorated with suspended 20-nm Au-nanoparticles with the help of Poly-L-Lysine solution and then placed between the two zones (set to temperatures T_1 and T_2) of the furnace. The temperature was first ramped to $T_1 = 500$–$510\,°C$ and $T_2 = 280\,°C$ within 60 min, kept at these values for 60 min, and finally reduced back to ambient temperature in roughly 4 h, while keeping a constant Ar flow of 600 SCCM.

Device fabrication. Our gate-tunable four-terminal devices were fabricated on degenerately-doped Si wafers covered by 280-nm thermally-grown SiO$_2$ which acts as a gate dielectric. Gold contact pads and a coordinate system were pre-defined by optical lithography. The as-grown nanowires were transferred by gently bringing together the surfaces of the pre-patterned wafer and the growth substrate, and nanowires suitable for device fabrication were identified by optical microscopy. Per device, five to seven contacts with varying distances were defined by electron beam lithography, which was performed by exposing a PMMA A4 resist layer using a Raith PIONEER Two system. The contact area was cleaned using gentle oxygen plasma treatment and a dip in dilute hydrochloric acid shortly before metallization. Subsequently, 5-nm-thick Pt was sputter-deposited as a wetting layer and an additional 45-nm-thick Au layer was deposited by thermal evaporation (devices 4 & 5) or by sputtering (devices 1, 2, and 3), resulting in the structure schematically shown in Fig. 1e. The contact resistance was well below 1 kΩ for all of the devices. Following the transport measurements, SEM was used to determine the device geometry and the nanowire diameter. The distance between the centers of the voltage contacts were 0.5, 0.8, 1.0, 1.2, and 0.7 μm, and the diameter of the nanowires were 41, 32, 41, 43, and 29 nm for devices 1–5, respectively.

TEM analysis. TEM micrographs, as well as TEM diffraction patterns, were recorded by using a JEM 2200-FS (JEOL) microscope operated at an acceleration voltage of 200 kV. A carbon film supported by a standard copper grid was used as sample carrier for TEM characterization. Elemental chemical analysis of the samples was done by Energy-Dispersive X-ray Analysis (EDX) performed with a JEOL Dry SD100GV detector.

Measurements. Transport measurements were performed in a liquid-helium cryostat in the temperature range of 2–300 K. The wafers were glued onto copper sample holders and manually bonded with 50-μm gold wires using vacuum-cured silver paste. For fast measurements, we used a quantum transport measurement system (SPECS Nanonis Tramea) in the low-frequency lock-in mode with the ac current of 100 nA at the frequency $f ≈ 17$ Hz, while the device is configured in a conventional four-(device 3, 4, & 5) or three-(device 1 & 2) terminal geometry. Gate-voltage sweeps were performed at various rates from 0.0125 V/s to 0.25 V/s while monitoring the sample temperature with a dedicated thermometer using a low-power AC resistance bridge (Lakeshore Model 370).

Theoretical calculations. We consider the surface states of a quantum wire described by the 2D Dirac equation where antiperiodic boundary conditions in the transverse direction arise from curvature-induced Berry phase effect[1]. Disorder is modeled by a small density of randomly located local scattering potentials, which is treated within a (non-self-consistent) T-matrix approximation, which can be calculated in a fully analytic way, see Supplementary Note 9. Within our approximation, qualitative features are independent of the density of impurities; however, they do depend on the amplitude of the scattering potential. The Kubo formula was used to calculate the conductivity. Vertex corrections were ignored as a previous study showed that they have only a small, purely quantitative effect[28]. Plots of resistivities were obtained from $ρ = 1/(σ_0 + σ(μ))$, where $σ_0$ is mainly used to avoid the divergence of $ρ$ when $σ = 0$. It describes the presence of conductance contributions (e.g., from impurity bands on the surface or in the bulk) not taken into account in our approximation. Note that, although the experimental data are shown in resistance R, the theory calculates the resistivity $ρ$, because the transport is assumed to be in the diffusive regime. The dependence of $μ$ on $ΔV_G$ is computed from $n(μ) = C_G ΔV_G / e$, where $n(μ)$ is the electron density along the wire and C_G is

treated as a fitting parameter. Full details of our calculations including a discussion of effects arising from deviations of the circular shape of the wire are given in Supplementary Notes 13–16.

References

1. Zhang, Y. & Vishwanath, A. Anomalous Aharonov-Bohm conductance oscillations from topological insulator surface states. *Phys. Rev. Lett.* **105**, 206601 (2010).
2. Bardarson, J. H., Brouwer, P. W. & Moore, J. E. Aharonov-Bohm oscillations in disordered topological insulator nanowires. *Phys. Rev. Lett.* **105**, 156803 (2010).
3. Cook, A. & Franz, M. Majorana fermions in a topological-insulator nanowire proximity-coupled to an s-wave superconductor. *Phys. Rev. B* **84**, 201105 (2011).
4. Alicea, J. New directions in the pursuit of majorana fermions in solid state systems. *Rep. Prog. Phys.* **75**, 076501 (2012).
5. Peng, H. et al. Aharonov-Bohm interference in topological insulator nanoribbons. *Nat. Mater.* **9**, 225 (2009).
6. Xiu, F. et al. Manipulating surface states in topological insulator nanoribbons. *Nat. Nanotechnol.* **6**, 216–221 (2011).
7. Tian, M. et al. Dual evidence of surface dirac states in thin cylindrical topological insulator Bi$_2$Te$_3$ nanowires. *Sci. Rep.* **3**, 1212 (2013).
8. Hamdou, B., Gooth, J., Dorn, A., Pippel, E. & Nielsch, K. Surface state dominated transport in topological insulator Bi$_2$Te$_3$ nanowires. *Appl. Phys. Lett.* **103**, 193107 (2013).
9. Safdar, M. et al. Topological surface transport properties of single-crystalline SnTe nanowire. *Nano Lett.* **13**, 5344–5349 (2013).
10. Hong, S. S., Zhang, Y., Cha, J. J., Qi, X.-L. & Cui, Y. One-dimensional helical transport in topological insulator nanowire interferometers. *Nano Lett.* **14**, 2815–2821 (2014).
11. Bäßler, S. et al. One-dimensional edge transport on the surface of cylindrical Bi$_x$Te$_{3−y}$Se$_y$ nanowires in transverse magnetic fields. *Appl. Phys. Lett.* **107**, 181602 (2015).
12. Cho, S. et al. Aharonov-Bohm oscillations in a quasi-ballistic three-dimensional topological insulator nanowire. *Nat. Commun.* **6**, 7634 (2015).
13. Arango, Y. C. et al. Quantum transport and nano angle-resolved photoemission spectroscopy on the topological surface states of single Sb$_2$Te$_3$ nanowires. *Sci. Rep.* **6**, 29493 (2016).
14. Jauregui, L. A., Pettes, M. T., Rokhinson, L. P., Shi, L. & Chen, Y. P. Magnetic field-induced helical mode and topological transitions in a topological insulator nanoribbon. *Nat. Nanotechnol.* **11**, 345–351 (2016).
15. Bhattacharyya, B., Sharma, A., Awana, V. P. S., Senguttuvan, T. D. & Husale, S. FIB synthesis of Bi$_2$Se$_3$ 1D nanowires demonstrating the co-existence of Shubnikov-de Haas oscillations and linear magnetoresistance. *J. Phys. Condens. Matter* **29**, 07LT01 (2017).
16. Ziegler, J. et al. Probing spin helical surface states in topological HgTe nanowires. *Phys. Rev. B* **97**, 035157 (2018).
17. Hong, S. S., Cha, J. J., Kong, D. & Cui, Y. Ultra-low carrier concentration and surface-dominant transport in antimony-doped Bi$_2$Se$_3$ topological insulator nanoribbons. *Nat. Commun.* **3**, 757 (2012).
18. Wang, Z., Qiu, R. L. J., Lee, C. H., Zhang, Z. & Gao, X. P. A. Ambipolar surface conduction in ternary topological insulator Bi$_2$(Te$_{1−x}$Se$_x$)$_3$ nanoribbons. *ACS Nano* **7**, 2126–2131 (2013).
19. Jauregui, L. A., Pettes, M. T., Rokhinson, L. P., Shi, L. & Chen, Y. P. Gate tunable relativistic mass and Berry's phase in topological insulator nanoribbon field effect devices. *Sci. Rep.* **5**, 8452 (2015).
20. Dufouleur, J. et al. Weakly-coupled quasi-1d helical modes in disordered 3d topological insulator quantum wires. *Sci. Rep.* **7**, 45276 (2017).
21. Kunakova, G. et al. Bulk-free topological insulator Bi$_2$Se$_3$ nanoribbons with magnetotransport signatures of dirac surface states. *Nanoscale* **10**, 19595–19602 (2018).
22. Taskin, A. A., Ren, Z., Sasaki, S., Segawa, K. & Ando, Y. Observation of Dirac holes and electrons in a topological insulator. *Phys. Rev. Lett.* **107**, 016801 (2011).
23. Ando, Y. Topological insulator materials. *J. Phys. Soc. Jpn.* **82**, 102001 (2013).
24. Beutler, D. E., Meisenheimer, T. L. & Giordano, N. Resistance fluctuations in thin Bi wires and films. *Phys. Rev. Lett.* **58**, 1240–1243 (1987).

25. Borgwardt, N. et al. Self-organized charge puddles in a three-dimensional topological material. *Phys. Rev. B* **93**, 245149 (2016).

26. Breunig, O. et al. Gigantic negative magnetoresistance in the bulk of a disordered topological insulator. *Nat. Commun.* **8**, 15545 (2017).

27. Bömerich, T., Lux, J., Feng, Q. T. & Rosch, A. Length scale of puddle formation in compensation-doped semiconductors and topological insulators. *Phys. Rev. B* **96**, 075204 (2017).

28. Taskin, A. et al. Planar hall effect from the surface of topological insulators. *Nat. Commun.* **8**, 1340 (2017).

29. Münning, F. et al. Dataset for "Quantum confinement of the Dirac surface states in topological-insulator nanowires". figshare. https://doi.org/10.6084/m9.figshare.13524050 (2021).

Acknowledgements

Author contributions

Y.A. conceived the project. F.M., O.B., D.F., and M.R. performed the growth and device experiments. S.R. performed the TEM analysis. H.F.L., supported by A.R., developed the theory. Y.A., F.M., H.F.L., O.B., and A.R. wrote the manuscript with inputs from all authors.

Funding

Competing interests

The authors declare no competing interests.

Additional information

Supplementary information The online version contains supplementary material available at https://doi.org/10.1038/s41467-021-21230-3.

Correspondence and requests for materials should be addressed to Y.A.

Peer review information *Nature Communications* thanks the anonymous reviewer(s) for their contribution to the peer review of this work.

Reprints and permission information is available at http://www.nature.com/reprints

Publisher's note Springer Nature remains neutral with regard to jurisdictional claims in published maps and institutional affiliations.

Supplementary Information for "Quantum confinement of the Dirac surface states in topological-insulator nanowires"

Felix Münning,[1] Oliver Breunig,[1] Henry F. Legg,[2,3] Stefan Roitsch,[4]

Dingxun Fan,[1] Matthias Rößler,[1] Achim Rosch,[2] and Yoichi Ando[1]

[1]*Physics Institute II, University of Cologne,*

Zülpicher Str. 77, 50937 Köln, Germany

[2]*Institute for Theoretical Physics, University of Cologne,*

Zülpicher Str. 77, 50937 Köln, Germany

[3]*Present address: Department of Physics, University of Basel,*

Klingelbergstrasse 82, CH-4056 Basel, Switzerland

[4]*Institute of Physical Chemistry, University of Cologne,*

Luxemburger Str. 116, 50939 Köln, Germany

1

Supplementary Note 1. Growth direction and shape of nanowires

TEM investigations reveal that the growth direction of the nanowires is parallel to the $\langle 11\bar{2}0\rangle$ direction, i.e. perpendicular to the c axis of the crystal structure. Since in our TEM characterization the nanowires lie on the supportive carbon carrier, the $\langle 11\bar{2}0\rangle$ direction is always oriented perpendicular to the optical axis of the microscope. However, the rotation of the nanowires along the growth direction is arbitrary with respect to the support. As a consequence, different orientations perpendicular to the growth direction can be observed by TEM. The c-axis, revealing the distinguished hexagonal symmetry, can only be observed occasionally. This fact also suggests that our nanowires are closer to a cylindrical shape than a ribbon shape. In this regard, it has been theoretically shown that the energetically most favorable cross-sectional shape of Bi_2Se_3 and Bi_2Te_3 nanowires grown along the $\langle 11\bar{2}0\rangle$ direction is hexagonal due to the alignment of atoms in neighbouring quintuple-layers [1]. In fact, it was experimentally found that a narrow Bi_2Se_3 nanowire (diameter of $\sim$80 nm) grown along the $\langle 11\bar{2}0\rangle$ direction has a hexagonal cross-section [2]. Therefore, it is most reasonable to assume that the narrow $(Bi_{1-x}Sb_x)_2Te_3$ nanowires grown in this work also have a hexagonal cross-section, rather than a rectangular cross-section often assumed for wide nanowires [3].

Supplementary Note 2. Homogeneity and purity of nanowires

The chemical composition of the $(Bi_{1-x}Sb_x)_2Te_3$ nanowire body is homogeneous along the nanowire axis, such that the atomic fraction of each element measured by EDX on six different locations varies only within a few percent (Fig. S1). An incorporation of Au atoms can be excluded within the accuracy of the measurement.
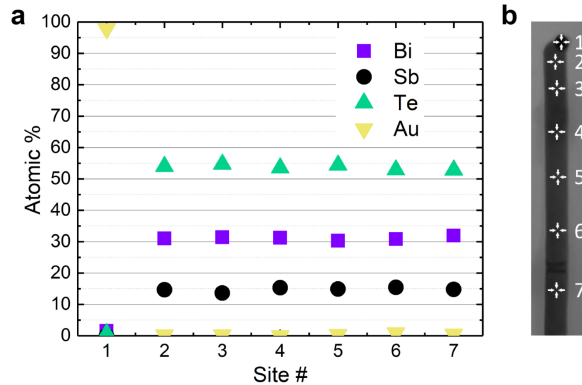
Supplementary Fig. 1: **Series of EDX measurements along the nanowire axis. a**, Atomic fraction of the elements Bi, Sb, Te, and Au at each location as shown in **b**.

2

Supplementary Note 3.   Universal conductance fluctuations

In mesoscopic systems universal conductance fluctuations (UCF) arise from a specific distribution of scattering sites. Our devices fall into this regime, which raises the question whether type I peaks could also be explained by UCF. However, type I peaks are much too regular to be caused by conductance fluctuations. UCF occur without any clear periodicity as a function of gate voltage or magnetic field. In contrast, the features of type I that we identify with the sub-band crossings occur in a regular fashion, i.e. at regularly spaced gate voltages, as shown by Fig. 2d. Secondly, the amplitude of type I features strongly differs from what would be expected for typical UCF. For UCF, the amplitude of individual peaks is random. In contrast, our type I oscillations occur with a largely uniform amplitude. Both of these facts speak against UCF as the origin of type I peaks. Furthermore, for every type I peak at gate voltage ΔV_G we observe a symmetry-related peak close to $-\Delta V_G$ (see Fig. 2d). This is expected from the presence of an approximate particle-hole symmetry of the Dirac cone of $(Bi_{1-x}Sb_x)_2Te_3$ [4] and is not consistent with UCFs for which no such symmetry is expected.

Another hallmark of UCFs is that they are strongly affected by small magnetic fields. If features of type I in our gating curves were UCF, they should rapidly change when applying a small magnetic field. Using device 6 (fabricated in the same way to devices 1-5) multiple gate sweeps were performed at constant magnetic fields of 0.1 and 0.5 T. Fig. 2 shows the average of these sweeps (see Supplementary Note 4 below). While there is finite differences in the background (which partly consists of residual type II fluctuations that may well be field-dependent) the main features that we identify with the sub-band crossings remain robust upon changing the magnetic field. Thus, we can clearly rule out UCFs as the origin of type I peaks, both due to the regularity of their amplitude and periodicity, as well as their independence on small magnetic fields.
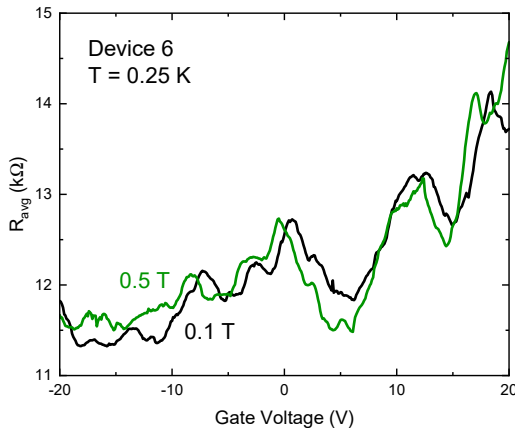
Supplementary Fig. 2: **Gate voltage dependence of the resistance of device 6.** The curves were obtained by averaging over multiple consecutive sweeps at magnetic fields of 0.1 and 0.5 T.

3

Supplementary Note 4.   Averaging of multiple gate sweeps

As discussed in the main text, two distinct types of oscillations are seen in the $R(V_{\mathrm{G}})$ curves: Large oscillations coming from sub-band crossings (type I, $\sim 3\ \mathrm{k\Omega}$) and smaller, time-dependent oscillations (type II, $\sim 0.5\ \mathrm{k\Omega}$). The type-I oscillations are reproducible and most of the peaks are well pronounced. On the other hand, as shown examplarily for device 5 in Fig. 3, the resistance of the devices changes with a timescale of a few minutes. The magnitude of these jumps is of the order of the type II features in the $R(V_{\mathrm{G}})$ curves. We speculate that each jump of the resistance is associated with a reconfiguration of the scattering site distribution and thus changes the background on which we expect to observe the intrinsic gate voltage or magnetic field dependence of the surface state transport. Since the gating-curves were measured in about 80 minutes, this process also takes place during our gate sweeps. The fact that type II features consequently differ between each individual sweep opens a way to suppress their conductivity contribution by performing a time average or, more practically, an average of multiple sweeps. Comparing the individual gate sweeps with the average (see Fig. 2a-c of the main text) clearly shows that large features (type I) are preserved upon averaging while minor peaks (type II) in the individual curves are suppressed. As such, averaging of multiple sweeps is a useful tool to deterministically extract the dominant conductivity features due to the Dirac sub-band structure.
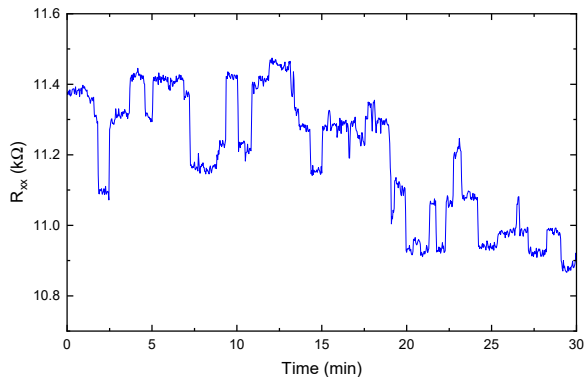
Supplementary Fig. 3: **Time-dependent resistance fluctuations.** Type II fluctuations measured as a function of time on device 5.

Supplementary Note 5.   Identification of the sub-band peaks without averaging

Even without performing gate voltage sweep averages, type I features are also found in each individual sweep as discussed for two additionally fabricated devices in the following. For these devices we did not perform averaging at the time of the data acquisition. Yet, they also show full gate-tunability through the Dirac point and their individual gating curves exhibit features similar to those of devices 1–3 discussed in the main text (Supplementary Fig. 4). By comparison

4

to the theory, major peaks can be indexed for these devices as well, even without performing a time-consuming averaging over a large number of gate sweeps. However, the type-II oscillations can make the identification of the type-I peaks complicated, and in such rare cases it is useful to adopt two criteria for the identification of the type-I peaks: amplitude and regularity. Namely, we identify peaks that stand out in terms of the amplitude and appear semi-regularly to be type-I. For example, the identification of type-I peaks in device 5 (Supplementary Fig. 4b) followed these criteria. Nevertheless, we emphasize that in most cases (such as device 1 shown in Fig. 2a) the identification of type-I peaks is evident. The intrinsic type-I peaks identified this way remain robust after averaging multiple gate sweeps as mentioned above and turn out to agree well with the theoretical calculations as shown in the main text.
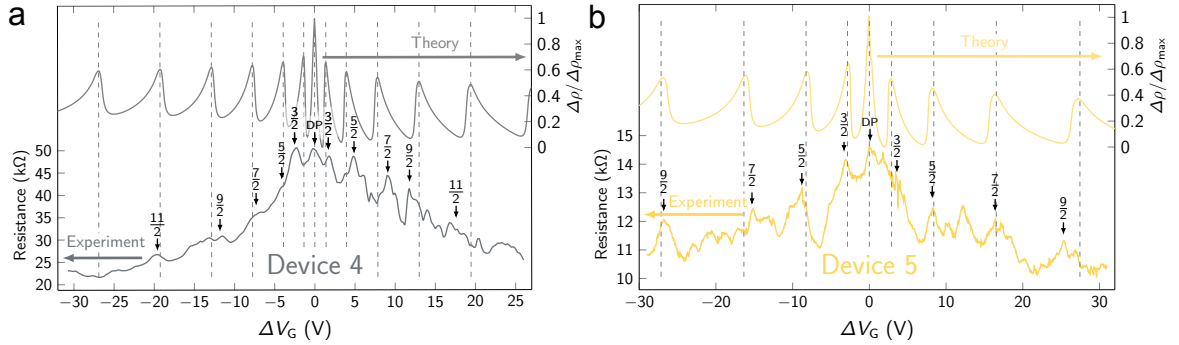
Supplementary Fig. 4: **Gate-voltage dependence of the resistance of the additional devices 4 and 5.** $\Delta V_{\mathrm{G}} = 0$ corresponds to the Dirac point of the TI surface state, which was achieved with V_{G} of -6 in device 4 and 19 V in device 5. We used R_{w} of 22 and 15 nm and C_{G} of 5.8 and 4.1 pF/m for devices 4 and 5, respectively. In comparison to theory, sub-band crossing peaks can be identified even though type II features are also present in these non-averaged, single gating curves.

Supplementary Note 6.   Geometric and quantum capacitances

In general, the gate voltage required to provide the nanowire with additional charge Q can be expressed as

$$V_{\mathrm{G}} = \frac{Q}{C_{\mathrm{G}}} + \frac{Q}{C_{\mathrm{Q}}}, \tag{1}$$

where C_{G} is the geometric capacitance of the device and C_{Q} is the quantum capacitance, or, equivalently, as $eV_{\mathrm{G}} = \frac{e^2}{C_{\mathrm{G}}} n(\mu) - \mu$, where $e < 0$ is the electron charge, μ the chemical potential, and $n(\mu)$ the electron density. In our experiments, a change of the gate voltage by 30 V leads to changes of the chemical potential by less then 100 meV. Therefore, the effect of the geometric capacitance dominates by more than two orders of magnitude and we can safely approximate $V_{\mathrm{G}} \approx \frac{1}{C_{\mathrm{G}}} en(\mu)$.

The geometric capacitance C_{G} was found to be $2 - 3.6$ pF/m in our experiments. Note that C_{G} depends on materials properties and the device geometry, and one needs to numerically calculate it for each situation [5]. For the present gate geometry, as presented in the section Supplementary

5

Note 13, a value of $C_{\mathrm{G}} \approx 15$ pF/m would be expected. However, our nanowires are not metallic as is typically assumed in simulations, and hence the result of such numerical simulations should be taken as an upper bound for C_{G}. In addition, the effective capacitance is further affected by parasitic capacitances due to the leads, as well as by the finite length of the nanowire. For these reasons we treat the value of the capacitance as a phenomenological parameter.

Supplementary Note 7.   Hamiltonian of a disordered TI nanowire

The Hamiltonian for the surface of a cylindrical TI nanowire of radius R_w depends only on momentum around the wire, $\hat{p}_\phi = \hat{L}_\phi/R_w = -iv_F\partial_\phi/R_{\mathrm{w}}$, and momentum along the wire, $\hat{p}_x = -i\hbar\partial_x$, and is given by [6]

$$H_{\mathrm{surf}} = i\hbar v_F \left(\frac{\sigma_x}{R_{\mathrm{w}}}\partial_\phi - (\sin(\phi)\sigma_z - \cos(\phi)\sigma_y)\partial_x \right). \tag{2}$$

This can be simplified by applying a spinor-rotation by ϕ about the x-axis, *i.e.*, the unitary transformation $U_x(\phi) = \exp(-i\phi\sigma_x/2)$. The result is the Hamiltonian

$$H_0 = i\hbar v_F \left(\frac{\sigma_x}{R_{\mathrm{w}}}\partial_\phi - \sigma_y\partial_x \right). \tag{3}$$

In the presence of a flux Φ threaded along the wire, ∂_ϕ is replace by $\partial_\phi - i\eta$ with $\eta = \Phi/\Phi_0$. Importantly, since spinor rotations are 4π periodic, the eigenfunctions of this Hamiltonian must obey anti-periodic boundary conditions, resulting from $U_x(\phi) = -U_x(\phi + 2\pi)$. As such the wave function can be written in the general form $\psi_\ell(k) = e^{i(kx+\ell\phi)}\boldsymbol{\xi}$, where the anti-periodic boundary conditions require the total angular momentum to satisfy $\ell = \pm 1/2, \pm 3/2, \ldots$ and $\boldsymbol{\xi}$ is a spinor encoding the spin-structure of the surface state within this rotated system.

Due to the finite geometry along the circumference of the wire the eigenenergies of the Hamiltonian are quantised

$$E_{\ell,\pm}(k) = \pm\hbar v_F \sqrt{k^2 + \left(\frac{\ell - \eta}{R_{\mathrm{w}}} \right)^2}. \tag{4}$$

The band edge of each band is for $\eta = 0$ given by $\varepsilon_{\ell,\pm} = \pm\hbar v_F \ell/R_{\mathrm{w}}$. We define $\varepsilon_\ell = \varepsilon_{\ell,+}$.

Disorder is modelled by impurity potentials located at random positions $\boldsymbol{r}_i$, $V_i(\boldsymbol{r}) = u_0 \mathbb{1}\delta(\boldsymbol{r} - \boldsymbol{r}_i)$, where $\boldsymbol{r}$ and $\boldsymbol{r}_i$ are 2d coordinates on the surface of the wire.

Supplementary Note 8.   Density of states and charge density

The free retarded Green's function – which is a matrix – has the form

$$[\boldsymbol{G}^0]_{\alpha\beta}(\mu, k, \ell) = (\mu\mathbb{1} - H_0(k, \ell) + i\delta\mathbb{1})^{-1}_{\alpha\beta}, \tag{5}$$

6

where we take the matrix inverse. Here δ acts as some overall background scattering rate due degrees of freedom (e.g. impurity bands) not described by our Hamiltonian. It has the effect of broadening the divergence of the density of states at the bottom of each sub-band.

The local Green's function of each ℓ resolved sub-band is given by

$$\mathbf{\Delta}(\mu,\ell) = \frac{1}{2\pi R_{\mathrm{w}} v_F} \int \frac{dk}{2\pi\hbar} \mathbf{G}^0(\mu,k,\ell) = -\frac{(\mu+i\delta)\mathbb{1} - \varepsilon_\ell \sigma_x}{4\pi v_F R_{\mathrm{w}} \hbar \sqrt{\varepsilon_\ell^2 - (i\delta+\mu)^2}}. \tag{6}$$

From the Green's function we can obtain the local density of states (at a fixed position at the surface of the wire)

$$\rho(\mu) = -\frac{1}{\pi} \sum_{\ell=\pm\frac{1}{2},\pm\frac{3}{2},\cdots} \mathrm{Im}\left\{\mathrm{Tr}\,\mathbf{\Delta}(\mu,\ell)\right\} = \frac{1}{2\pi^2 R_{\mathrm{w}} v_F \hbar} \sum_{\ell=\pm\frac{1}{2},\pm\frac{3}{2},\cdots} \mathrm{Im}\{\frac{\mu+i\delta}{\sqrt{\varepsilon_\ell^2 - (i\delta+\mu)^2}}\}, \tag{7}$$

which, as should be expected, tracks the 2d Dirac density of states $\rho^{\mathrm{2d}}(\mu) = |\mu|/2\pi v_F^2 \hbar^2$.

From the density of states we can also obtain the charge density along the wire. It is given by

$$n(\mu) = 2\pi R_{\mathrm{w}} \int_0^\mu d\mu' \rho(\mu') = -\frac{1}{\pi v_F \hbar} \mathrm{Im}\left\{ \sum_{\ell=\pm\frac{1}{2},\pm\frac{3}{2},\cdots} \sqrt{\varepsilon_\ell^2 - (\mu+i\delta)^2} \right\}. \tag{8}$$

Here $n(\mu)$ is zero at the Dirac point and counts the total charge density per length of wire. For $\mu > 0$ this means counting the contribution of all bands above the Dirac point up to the chemical μ. Correspondingly, for $\mu < 0$ counting the charge of all holes contributed by bands below the Dirac point, in other words $n(\mu)$ is negative for $\mu < 0$. It is shown as a grey line in Fig. 2d of the main text.

Supplementary Note 9.   T-matrix approximation

The full disorder averaged Green's function is

$$[\mathbf{G}]_{\alpha\beta}(\mu,k,\ell) = (\mu\mathbb{1} - H_0(k,\ell) + \mathbf{\Sigma}(\mu))^{-1}_{\alpha\beta}, \tag{9}$$

where $\mathbf{\Sigma}(\mu)$ is the full self-energy from all scattering processes, including disorder and the other scattering processes modelled by the factor $i\delta$ (see Supplementary Note 8).

To approximate the self-energy contribution due to disorder scattering we use the full T-matrix calculated at first order in impurity density n_{imp} (i.e. the non-crossing approximation). Within

7

this approximation the self-energy, which is also a matrix, is [7]

$$[\boldsymbol{\Sigma}]_{\alpha\beta}(\omega) = n_{\text{imp}} u_0 \left\langle \left(\mathbb{1} - \frac{u_0}{2\pi R_{\text{w}}} \sum_{\ell=\pm\frac{1}{2},\pm\frac{3}{2},\dots} \int \frac{dk}{2\pi\hbar v_F} \boldsymbol{G}^0(k,\mu,\ell) \right)^{-1} \right\rangle_{\text{imp}}$$

$$= n_{\text{imp}} u_0 \left(\mathbb{1} - u_0 \sum_{\ell=\pm\frac{1}{2},\pm\frac{3}{2},\dots} \Delta(\mu,\ell) \right)^{-1}. \qquad (10)$$

For small δ the $\boldsymbol{\Delta}(\mu,\ell)$, from Eq. (6), only has a substantial imaginary part for $|\mu| > |\varepsilon_\ell|$, this means that a conductivity channel only contributes when the corresponding sub-band has an occupation of electrons (holes) for the upper (lower) Dirac cone. Further the off-diagonal components of $\boldsymbol{\Sigma}$ are exactly zero for diagonal impurities since the off-diagonal contributions of positive and negative ℓ cancel.

The self-energy can also be calculated self-consistently by replacing $\mu \to \mu + \Sigma_{11}$ and $\varepsilon_\ell \to \varepsilon_\ell + \Sigma_{12}$, where Σ_{11} and Σ_{12} are the diagonal and off-diagonal components, respectively. Self-consistency has a similar impact on the self-energy as δ, that is, the breadth of the peaks in scattering rate become broadened in proportion to the self-energy itself. Ultimately this means that peaks at high sub-band index become "washed out" when the self-energy is of the same order of magnitude as the sub-band spacing. This is not of relevance for the experimental situation discussed here where the mean free path is several times the wire radius, but would limit the number of peaks seen in thicker or dirtier wires where the ratio of mean free path and radius can be substantially smaller.

Supplementary Note 10. Conductivity calculation

The conductivity is found using the Kubo formula to calculate the current-current correlation function in linear response. The current operator along the wire is given by $j_x = e\partial H/\partial k = -i\hbar v_F e \sigma_y$. We neglect vertex corrections which previous studies have shown only have a quantitative effect on overall conductivity[7]. Within this scheme the DC conductivity is given by

$$\sigma = \frac{e^2 v_F^2 \hbar^2}{\pi} \frac{1}{2\pi R_{\text{w}}} \sum_{\ell=\pm\frac{1}{2},\pm\frac{3}{2},\dots} \int d\omega \, n_F'(\omega) \int \frac{dk}{2\pi\hbar} \text{Tr}\left(\sigma_y \boldsymbol{G}(\omega,k,\ell) \sigma_y \boldsymbol{G}^\dagger(\omega,k,\ell) \right) = \sum_{\ell=\pm\frac{1}{2},\pm\frac{3}{2},\dots} \sigma_\ell(\mu),$$
$$(11)$$

where in general the contribution σ_ℓ is given by

$$\sigma_\ell(\mu) = \frac{e^2 v_F}{(2\pi)^2 R_{\text{w}}} \frac{1}{\tilde{\mu}\Gamma_{11} - \tilde{\varepsilon}_\ell \Gamma_{12}} \text{Im}\left\{ \frac{\lambda}{\sqrt{\xi}} - \frac{\lambda^\dagger}{\sqrt{\xi^\dagger}} \right\} \approx \theta(\mu^2 - \varepsilon_l^2) \frac{e^2 v_F}{2\pi^2 R_{\text{w}} |\Gamma_{11}|} \frac{\mu^2 - \varepsilon_l^2}{\mu\sqrt{\mu^2 - \varepsilon_l^2}}, \qquad (12)$$

8

where $\mathbf{\Gamma} = \mathrm{Im}\mathbf{\Sigma}$ is the (spin-resolved) scattering rate, $\tilde{\mu} = \mu + \mathrm{Re}\Sigma_{11}$, $\tilde{\varepsilon}_\ell = \varepsilon_\ell + \mathrm{Re}\Sigma_{12}$, and the factors $\xi = -(\mu + i\Gamma_{11})^2 + (\varepsilon_\ell + i\Gamma_{12})^2$ and $\lambda = -\tilde{\varepsilon}_\ell^2 - i\tilde{\varepsilon}_\ell\Gamma_{12} + i\tilde{\mu}\Gamma_{11} + \tilde{\mu}^2$ ensure the channel only contributes to conductivity when $|\mu| \gtrsim |\varepsilon_\ell|$. The approximation in Eq. (12) is valid for small self-energies and diagonal impurities.

Supplementary Note 11. Parameters for theory plots

An important parameter for our theory is u_0, the strength of the impurity potential. In Supplementary Fig. 5 we show the resistivity as function of gate voltage for weak, intermediate and strong impurity potentials. Only for weak impurity potentials, $\frac{u_0}{\hbar v_F R_\mathrm{w}} \ll 1$, peaks occur at the band edges and particle- and hole doping are almost equivalent. For intermediate impurity strength, $\frac{u_0}{\hbar v_F R_\mathrm{w}} \sim 1$, the curve is highly asymmetric. For $\frac{u_0}{\hbar v_F R_\mathrm{w}} \gg 1$, the particle-hole symmetry is restored but instead of peaks one obtains dips.

We find that only weak u_0 fit the experimental data. This is expected because the wavefunction of the conduction channel wraps around the circumference of the wire, effectivly diluting the impurity by a factor $1/(2\pi R_\mathrm{w})$. To be precise: Weak scattering can be defined by $u_0\bar{\rho} \ll 1$, where $\bar{\rho} \sim \frac{1}{2\pi v_F \hbar R_\mathrm{w}}$ is the typical density of states in the system for small ℓ. Assuming that the width of the scattering potential is of the order of the lattice constant a, the weak scattering limit is reached when the amplitude, $V_0 = u_0/a^2$, of the scattering potential fulfils $V_0 \ll \frac{v_F}{a\hbar}\frac{2\pi R_\mathrm{w}}{a}$. Since in our experiments the circumference is many lattice constants, $\frac{R_\mathrm{w}}{a} \sim 100$, the weak scattering limit is generically realised.

Therefore, for the plots in Fig. 2 and Fig. 3 of the main text we use $u_0 = 0.1 v_F \hbar R_\mathrm{w}$, $n_\mathrm{imp} = 20/R_\mathrm{w}^2$ and $\delta = 0.025 v_F \hbar/R_\mathrm{w}$, see also method section. This reproduces the order of magnitude ~ 5 nm/kΩ of the fluctuations in wire conductivity found experimentally.

While the main contribution to the peaks at the sub-band edges arised from the diverging density
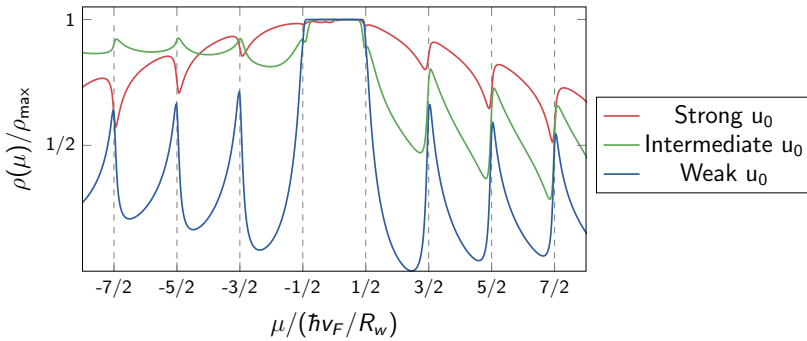
Supplementary Fig. 5: **Resistivity as a function of chemical potential in the weak, intermediate, and strong scattering regimes**. A weak scatterer, $\frac{u_0}{\hbar v_\mathrm{F} R_\mathrm{w}} = 0.1$, $n_\mathrm{imp} = 20/R_\mathrm{w}^2$, as in the main text, is shown as the blue curve. The green curve, $\frac{u_0}{\hbar v_\mathrm{F} R_\mathrm{w}} = 1$, $n_\mathrm{imp} = 2/R_\mathrm{w}^2$, describes scatterers of intermediate strength, the red curve, a strong scatterer $\frac{u_0}{\hbar v_\mathrm{F} R_\mathrm{w}} = 20$, $n_\mathrm{imp} = 0.1/R_\mathrm{w}^2$. Strong scattering is capable of turning resistivity peaks at sub-band edges into resistivity dips, however such a situation is unlikely (see text).

9

of states, this effect is further enhance by a matrix-element effect closely related to the topological protection of TI surface states. Here the spin orientation is locked to the propagation direction and scattering from $\boldsymbol{k}$ to $-\boldsymbol{k}$ is prohibited by time-reversal symmetry. In our nanowires, $k_y = \ell/R_{\mathrm{w}}$ is quantized, and the 1D bands are doubly degenerate as for each $k_x = k$, two transverse momenta, $\pm k_y$, are possible. For $k_x \gg k_y$, however, the 2D vectors $\boldsymbol{k} = (k_x, \pm k_y)$ and $\boldsymbol{k} = (-k_x, \pm k_y)$ are almost antiparallel, leading to a suppression of the scattering rate by the factor $(k_y/k_x)^2$. This matrix element effect (encoded in the 2×2 matrix structure of the T-matrix) substantially suppresses backscattering among occupied channels with $\ell/R_{\mathrm{w}} \ll k_x$ relative to the scattering to a newly opened channel with a large k_y.

Supplementary Note 12. Electron-hole puddles

Several physical effects have not been taken into account by our theoretical treatment. For example, we do not reproduce the type II fluctuations which likely arise from extra charge traps in the experimental setup. We also assume scattering from local impurities, but there will be also long-range potentials arising from randomly distributed positive and negative charges in our compensation doped samples of $(\mathrm{Bi}_{1-x}\mathrm{Sb}_x)_2\mathrm{Te}_3$. In bulk systems, these lead to the formation of electron-hole puddles [8, 9] both in the bulk and in the surface states [10] of TIs. Estimates from Ref. 11 suggest that bulk puddles are absent in TI nanowires with a radius of less than $\sim 100\,\mathrm{nm}$. But also in this case, one can expect substantial fluctuations of the chemical potential on the surface of the TI. For surface states of bulk samples of $\mathrm{BiSbTeSe}_2$, fluctuations of the local chemical potential with an amplitude of $20\,\mathrm{meV}$ on a length scale of $50\,\mathrm{nm}$ have been measured by scanning tunneling spectroscopy [10]. While the size of these fluctuations will be reduced for nanowires, surface puddles can be expected to be of quantitative importance (perhaps, also for type II fluctuations).

Supplementary Note 13. Electrostatic modeling and anisotropy effects

In Supplementary Notes 7-11 above, we investigated disorder effects assuming an idealized setup with cylindrical symmetry. Now we investigate the role of anisotropy effects arising both from the hexagonal shape of the wire and of the electrostatic environment. As shown in Supplementary Fig. 6a, wires with diameters between 29 and 43 nm are positioned on a 255 nm thick dielectric SiO_2 substrate, see methods for details. When in our experiment the chemical potential is adjusted via a flat bottom gate below the dielectric substrate, the induced charge around the wire will not be uniform and will depend on both the substrate/gate geometry and also the approximately hexagonal wire shape. These geometric effects can introduce changes to both the sub-bands and the charging physics of the wires. We will show that Klein-tunnelling physics means that the locations of the sub-band minima in terms of chemical potential are largely unchanged and so the underlying theoretical signature of confinement: An increased scattering at the bottom of each sub-band and a corresponding resistivity peak, should remain robust for most set-ups. In contrast, charging effects could be important such that the mapping from induced charge density to chemical

10
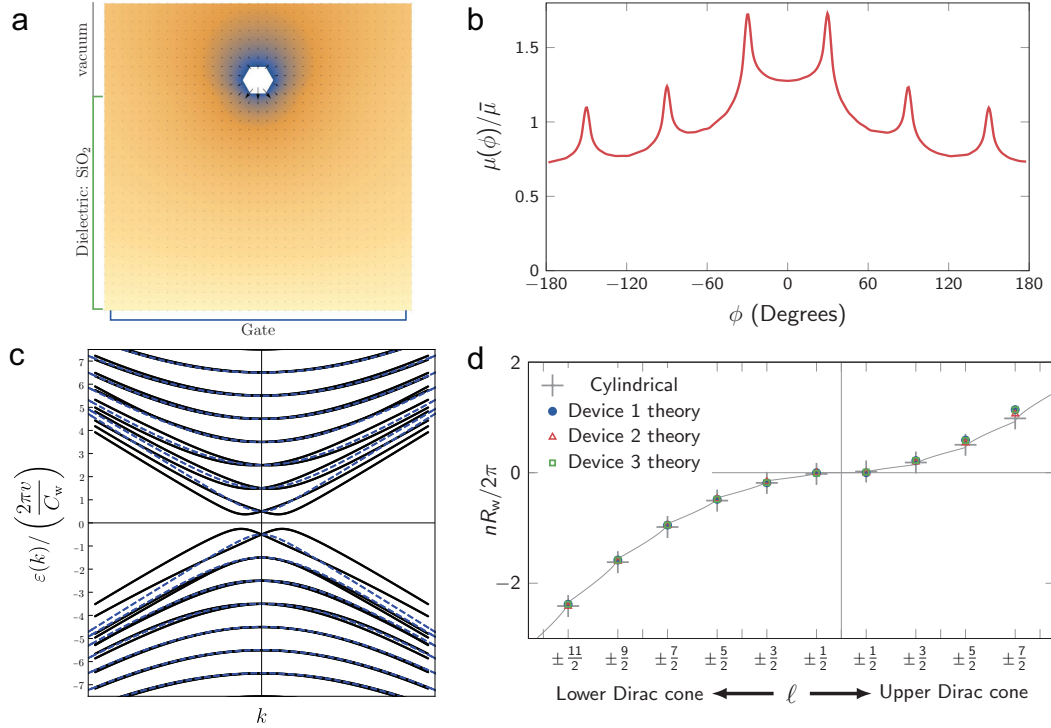
Supplementary Fig. 6: **Effect of a bottom gate on an hexagonal nanowire**. **a** Numerical solution of the Laplace equation and electric field due to bottom gate and metallic hexagonal wire. **b** Ratio of chemical potential, $\mu(\phi)$, to the average chemical $\bar{\mu}$ around the nanowire. **c** Resulting sub-bands of device 1 when tuned to the charge neutrality point. The sub-bands of an isotropic circular wire are shown as blue dashed lines. **d** Theoretically calculated locations of the van-Hove singularities in the experiment as a function of charge density for anisotropic hexagonal wires (circles) compared to the isotropic wire (grey crosses).

potential is influenced by the geometry of the system.

For our experiment, however, we will argue that these effects are below the resolution of the experiment and so the cylindrical wire description above remains a valid approximate model of our experimental set-up. Such effects could, however, be important in future experiments.

We would like to stress that, as discussed above, the following electrostatic modeling is not fully quantitative as it ignores, for example, parasitic capacitances as arising, e.g., from the gold contacts, see Fig. 1d of the main text, and the finite length of the wire. Furthermore, our modeling assumes metallic surfaces of the topological insulator and there are effects arising from the finite penetration depth of the surface state, the experimental uncertainty in the radius of the wire and its surface chemistry, and also possible effects arising from electron-hole puddles, see Supplementary Note 12, which may act as extra charge reservoirs.

11

Supplementary Note 14. Influence of geometry on energies of sub-band minima

We start by addressing the influence of the geometric effects on the sub-band minima and associated resistivity maxima. An important question for our experiment and physical interpretation is the consequence the induced charge anisotropy has for the confinement of surface states around the wire. It turns out that the Dirac nature of the TI surface states leads to Klein tunnelling of the state through any smooth surface potential and that, as a result, the energies of sub-band minima and associated peaks in resistivity are only very weakly sensitive to any charge anisotropy.

The charge anisotropy induced by bottom gating can be modelled as an angular dependent chemical potential $\mu(\phi) = \bar{\mu} + \delta\mu(\phi)$, where $\bar{\mu}$ is the averaged chemical potential around the wire and $\delta\mu(\phi)$ the angular variation of the chemical potential. (An estimate of $\mu(\phi)$ calculated using an electrostatic model and the full influence on sub-bands, which is important for the charge density, can be found below).

Of relevance to our study is the impact this angular dependent potential has on the quantisation of the surface states. In the cylindrical case the location of the quantisation peaks is set by the energies of the bottom of the sub-bands i.e. at $k = 0$. Adding an inhomogeneous chemical potential $\mu(\phi)$ to the Hamiltonian of the surface at the sub-band bottom gives

$$H_{k=0} = i\hbar v_F \sigma_x \frac{\partial_\phi}{R_W} + \mu(\phi)\mathbb{1}. \tag{13}$$

This Hamiltonian still has quantum confined eigenstates around the wire, given exactly by

$$\psi_\pm(\ell, k = 0) = \boldsymbol{\xi}_\pm e^{i\left((\ell-\bar{\mu})\phi - \int_0^\phi d\phi' \, \delta\mu(\phi')\right)}, \tag{14}$$

with $\ell = \pm\frac{1}{2}, \pm\frac{3}{2}, \pm\frac{5}{2}, ...$ and the spinors $\boldsymbol{\xi}_\pm$ are eigenspinors of the Pauli-matrix σ_x. Although the states $\psi_\pm(\ell, k = 0)$ are no longer simultaneous eigenstates of the angular momentum operator $L_z = -iv_F \frac{\partial_\phi}{R_W}$, they still have eigen-energies $\varepsilon_{\ell,\pm} = \pm\hbar v_F|\ell|$, the same as those of a wire with an isotropic surface chemical potential $\bar{\mu}$. Importantly this means that the locations where the chemical potential are tuned to a sub-band edge, $\mu_0 = \varepsilon_{\ell,\pm}$, will be very close to those of an idealised circular wire without any inhomogeneity.

Physically, the absence of an effect at $k = 0$ is due to Klein tunnelling of 1d chiral modes around a wire through the additional potential $\delta\mu(\phi)$, this potential only induces an angular dependence of the mode's phase and does not alter its energy at $k = 0$ [12]. Away from $k = 0$ the Klein-tunneling is not perfect and anistotropies can cause small shifts in the sub-band minima to finite k, most prominently for low angular momenta sub-bands, see Supplementary Fig. 6c and explanation below. Strikingly, however, the perfect Klein-tunnelling at $k = 0$ and strong but imperfect Klein-tunnelling for small k means that there is very little change in the energies where sub-band minima occur and associated resistivity peaks at these energies, even if that anisotropy is much larger than the sub-band gap.

<center>12</center>

Supplementary Note 15.   Estimate of the anisotropic chemical potential

Although Klein-tunnelling results in extremely small changes in the energies of sub-band minima due to geometric effects, the charge density – as changed in the experiment – will be dependent on these effects due to changes at large k where Klein-tunnelling is less effective and suppressed [12]. To assess the influence of these effects on density we first need to obtain an estimate of the induced charge and resulting anisotropy in chemical potential $\mu(\phi) = \bar{\mu} + \delta\mu(\phi)$, this can be approximated using a classical electrostatic analysis. As in Ref. [12], the inhomogeneity of charge density can be estimated by numerically solving the Laplace equation for our set-up, $\nabla\big[\varepsilon(x,y)\nabla\Phi(x,y)\big] = 0$, as shown in Supplementary Fig. 6. We use $\varepsilon = 3.5$ for the dielectric constant of SiO_2 and the Dirichlet conditions $\Phi(x,y) = V_G$ on the gate and $\Phi(x,y) = 0$ on the surface of the TI nanowire, which assumes the wire is perfectly metallic and hexagonal (with rounded corners, see below). The induced charge on the nanowire is proportional to the electric field normal to the wire, $\sim \nabla\Phi(x,y)\cdot\hat{\boldsymbol{r}}$. To obtain an estimate for $\mu(\phi)$, we can use the 2D Dirac relation $n \propto \mu^2$. The ratio of the chemical potential to its average is shown Supplementary Fig. 6b in terms of the polar angle around the wire. We see that the flat bottom gate leads to an imbalance in chemical potential around the wire and that the hexagonal shape results in sharp features at the corners of the wire. This numerical estimate assumes that the surface of the nanowire is perfectly metallic, with no penetration of the surface state into the wire. The influence of the finite penetration of the surface state into the wire will be most apparent at the corners, which cannot anyway be treated as perfectly sharp, and at the bottom of the wire, where the wire touches the dielectric. To model this we assume a small distance of 1 nm between dielectric and bottom of the wire and round the edges of the hexagon by the equivalent of 0.2 nm, which is much smaller than estimates for the penetration depth of the surface state and so likely overestimates the sharpness of the voltage spikes at the corners.

Supplementary Note 16.   Influence of geometry on charge density of sub-band minima

Having obtained an upper bound for the chemical potential anisotropy around the wire, $\delta\mu(\phi)$, we can use this to calculate the full change of the resulting sub-bands through the matrix elements $\langle \ell, \eta|\, \delta\mu(\phi)\, |\ell', \eta'\rangle$ between different sub-bands, where ℓ is the angular momentum and $\eta = \pm$ indicates particle/hole sub-bands. These matrix elements can be simplified since

$$\langle \ell, \eta|\, \delta\mu(\phi)\, |\ell', \eta'\rangle = \boldsymbol{\xi}^{\dagger}_{\ell,\eta}(k)\boldsymbol{\xi}^{\dagger}_{\ell',\eta'}(k) \int \frac{d\phi}{2\pi} e^{i(\ell'-\ell)\phi}\delta\mu(\phi) = \left[\boldsymbol{\xi}^{\dagger}_{\ell,\eta}(k)\boldsymbol{\xi}_{\ell',\eta'}(k)\right]\delta_{|\ell-\ell'|,n}\frac{\delta\mu_{(n)}}{2} \qquad (15)$$

where the product in square brackets accounts for Klein-tunnelling effects and we have used the Fourier cosine transformation of the anisotropic chemical potential $\delta\mu(\phi) = \sum_{n=1}^{\infty} \delta\mu_{(n)}\cos(n\phi)$. Diagonalising the full Hamiltonian matrix for each k we can obtain the band structure for a given average chemical potential $\bar{\mu}$. An example of the resulting sub-bands is shown in Supplementary Fig. 6c which is calculated for the parameters of device 1 when it is tuned to the Dirac point. As expected from the above discussion on Klein tunnelling, there is little alteration to the locations

13

of the sub-band minima in terms of energy apart from a small splitting of the lowest angular momentum sub-band $\ell = \pm 1/2$ away from $k = 0$, which results from the fact $\delta\mu_{(1)}$ is largest. Since this sub-band is anyway not visible in our experiment the theoretical discussion of transport in the main text is essentially unchanged by geometric effects. In particular, the theoretical plot Fig. 3 of the main text, which shows that resistivity peaks are equally spaced as a function of chemical potential for a circular wire, remains valid for our geometry apart from very small shifts in peak positions and the onset of a finite conductivity at a slightly smaller chemical potential.

Despite this, we see in Supplementary Fig. 6c that for large k the bands and their net velocity are affected by the anisotropies arising from $\mu(\phi)$. Thus the charge density $n(\bar{\mu})$ is modified, which is the quantity controlled in our experiment by the gate voltage. To estimate the influence of the anisotropy on the position of the peaks as a function of charge density – rather than chemical potential – we show in panel Supplementary Fig. 6d the charge density at which the bottom of a sub-band occurs and a resistivity peak is expected (to be compared to Fig. 2d of our paper). The plot is calculated self-consistently by tuning the chemical potential to a given sub-band minimum, then recalculating all bands for the applied potential. This allows the recalculation of densities and applied voltages in an iterative procedure until convergence is reached.

Supplementary Fig. 6d shows the resulting effect is small for all three of our experimental devices, which differ by the amount of gate voltage ($V_G^0 = 30.5$, 10, and 18.5 V for device 1, 2, and 3, respectively) needed to reach charge neutrality. For negative voltages the effects are completely negligible for all three devices but for positive voltages which add to V_G^0 there is a small effect visible, most pronounced for device 1 as V_G^0 is largest in this case. More precisely, we find that the change of density Δn is smaller than $0.2\frac{2\pi}{R_W}$ which corresponds to a change of gate voltage of $\approx 4.5\,\mathrm{V}$ for the largest peak shift of device 1, i.e. $\ell = 7/2$ for $\Delta V_G > 0$. Actually, this trend is consistent with our data (the circular-wire fits predict the position of the peak at $\Delta V_G \approx 24\,\mathrm{V}$ but it occurs experimentally at $\Delta V_G \approx 27\,\mathrm{V}$). Although this might indicate the change of charge density is just visible in our experiment, one should also take into account experimental noise, the substantial uncertainties in our electrostatic modeling, and further small perturbations to the sub-band structure, e.g. due to non-linearities of the Dirac spectrum.

For device 2 the effect of anisotropies is smaller compared to device 1, while device 3 is similar to device 1. In device 2 we find a maximal shift in density of $0.12\frac{2\pi}{R_W}$ or $\approx 2.5\,\mathrm{V}$ for the largest shift in a peak, i.e. for $\ell = 7/2$ of the upper Dirac cone, which occurs at $\Delta V_G = 28\,\mathrm{V}$. We therefore conclude that the effects of gate-, dielectric- and shape-induced anisotropies on charge density are small for our experimental set-up and do not affect our modelling of the experiment. In particular the presence of quantum-confined surface states in a bulk-insulating quantum wire identified by resistivity peaks with a super-linear dependence on gate voltage remains valid our set-up, but geometric effects may be relevant for future devices, in particular when a large gate voltage is necessary for accessing the Dirac point.

---

[1] Virk, N. & Yazyev, O. V. Dirac fermions at high-index surfaces of bismuth chalcogenide topological insulator nanostructures. *Sci. Rep.* **6**, 20220 (2016).

14

[2] Zhu, H. *et al.* Topological insulator Bi_2Se_3 nanowire high performance field-effect transistors. *Sci. Rep.* **3**, 1757 (2013).

[3] Kong, D. *et al.* Topological insulator nanowires and nanoribbons. *Nano Lett.* **10**, 329–333 (2010). 0912.5045.

[4] Zhang, J. *et al.* Band structure engineering in $(Bi_{1-x}Sb_x)_2Te_3$ ternary topological insulators. *Nat. Commun.* **2**, 574 (2011).

[5] Wunnicke, O. Gate capacitance of back-gated nanowire field-effect transistors. *Appl. Phys. Lett.* **89**, 083102 (2006).

[6] Zhang, Y. & Vishwanath, A. Anomalous Aharonov-Bohm conductance oscillations from topological insulator surface states. *Phys. Rev. Lett.* **105**, 206601 (2010).

[7] Taskin, A. *et al.* Planar hall effect from the surface of topological insulators. *Nat. Commun.* **8**, 1340 (2017).

[8] Borgwardt, N. *et al.* Self-organized charge puddles in a three-dimensional topological material. *Phys. Rev. B* **93**, 245149 (2016).

[9] Breunig, O. *et al.* Gigantic negative magnetoresistance in the bulk of a disordered topological insulator. *Nat. Commun.* **8**, 15545 (2017).

[10] Knispel, T. *et al.* Charge puddles in the bulk and on the surface of the topological insulator $BiSbTeSe_2$ studied by scanning tunneling microscopy and optical spectroscopy. *Phys. Rev. B* **96**, 195135 (2017).

[11] Bömerich, T., Lux, J., Feng, Q. T. & Rosch, A. Length scale of puddle formation in compensation-doped semiconductors and topological insulators. *Phys. Rev. B* **96**, 075204 (2017).

[12] Ziegler, J. *et al.* Probing spin helical surface states in topological HgTe nanowires. *Phys. Rev. B* **97**, 035157 (2018).

15

6

PROXIMITY-INDUCED SUPERCONDUCTIVITY IN TI NANOWIRES

Inducing superconductivity by the proximity effect into the surface states of topological insulator nanowires is a promising route not only to realize Majorana fermions, but also to explore the peculiar physics of the topological surface states. In this chapter, results on electronic transport measurements at cryogenic temperatures of proximity-induced superconductivity in BST nanowire Josephson junctions are discussed.

As superconductors, two kinds of material are used, niobium (Nb, Section 6.1), and vanadium (V) enclosed in the stacking composition Ti/V/Ti/Al (Section 6.2). In both systems, a fully dissipationless current across the Josephson junction is observed. In a current-based wiring with standard lock-in technique (details in Chapter 3.3), the differential resistance is measured at magnetic fields in all spatial directions. In fields perpendicular to the nanowire axis, no Fraunhofer interference patterns are observed, which is consistent with the picture of quasi-one-dimensional transport. Gate-dependent resistance oscillations similar to previous normal state experiments (Chapter 5) are observed and the critical cur-

rent of the junctions follows approximately the inverse behavior.

After characterizing the successful proximitization by Josephson junction physics, electronic transport is investigated further. In Section 6.4, tunneling spectroscopy measurements are presented, in which the density of states is measured close to the superconducting leads. These measurements lay the foundation towards precisely resolving the electronic states within the superconducting gap in proximitized TI nanowires.

6.1   Nb Josephson junction on BST nanowire

In this section, the proximity induced superconductivity by Nb in BST nanowires is investigated in Josephson junctions. The SEM micrograph in Figure 3.1a shows a representative device, featuring a nanowire Josephson junction in pseudo-4-point wiring. This type of device is used to fine-tune the fabrication, nanowire surface preparation and metallization details in order to improve the proximitization, before proceeding to more complex device architectures.

6.1.1   Temperature dependence

At base temperature, the main task is to access the characteristic physics of the topological surface states. This is only possible if the chemical potential of the nanowires lies close to charge neutrality. For this purpose, the high temperature part of a cooldown curve is insightful, revealing the temperature dependence of the resistance of the nanowire in the normal state. Figure 6.1 shows the cooldown R-T-curve of Device 1. The normal state temperature dependence, shown by the upper inset, features a wide hump between 20 K and 80 K, and a swift upturn below 18 K. This shape is consistent with $(\text{Bi}_{1-x}\text{Sb}_x)_2\text{Te}_3$ nanowires and thin films with good charge carrier compensation [1, 100, 106].
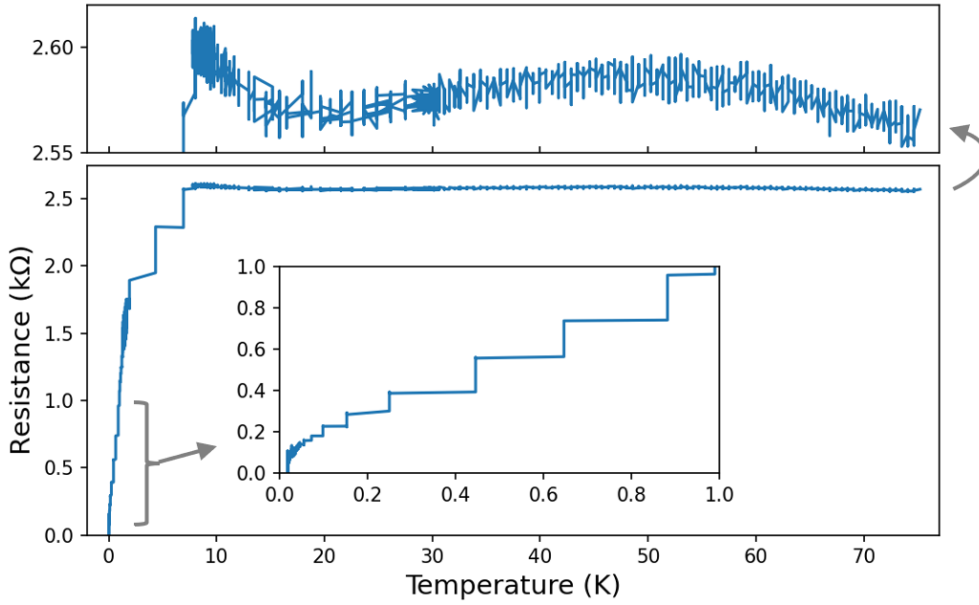
Figure 6.1: **Cooldown curve of Device 1. Upper panel:** *Temperature dependence of resistance in the normal state and onset of the superconducting transition. Enlarging the curve vertically around its normal resistance reveals one of the typical R-T characteristics of bulk-insulating $(Bi_{1-x}Sb_x)_2\,Te_3$ nanowires and thin films.* **Lower panel:** *Full cooldown curve.* **Inset:** *Enlarged completion of the superconducting transition down to zero resistance. Steps in the curve are due to the cryostat temperature readings.*

Below 8 K, the Nb leads turn superconducting (Appendix A.2) and the junction resistance starts to suddenly drop. At the lowest temperatures, as shown by the lower inset, the resistance is steadily dropping and approaching, but not quite reaching zero yet, which will be achieved later, after a longer period of thermalization. As measured subsequently and shown in Figure 6.2a, this Josephson junction has a critical current of 6.1 nA. Following the argument in Section 2.4.1, expressing the corresponding Josephson coupling energy in units of k_B yields a temperature of $E_{J0}(I_c = 6\,\text{nA})/k_B \approx 143\,\text{mK}$. Hence, the incomplete superconducting transition in the cooldown measurement might be owed to the slowly decreasing effective temperature of the sample and nearby wiring in the 100 mK range. After the onset of superconductivity at 8 K, reaching zero resistance took about 9 h.
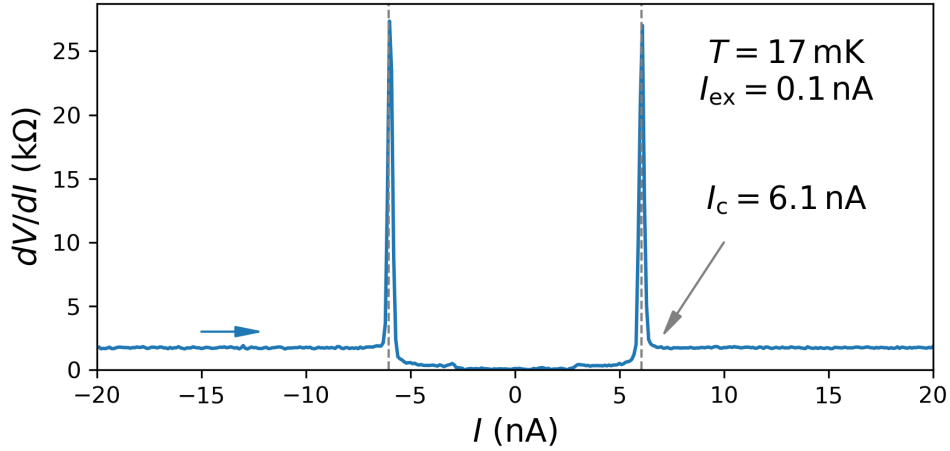
Figure 6.2: **Device 1: Differential resistance at low bias currents.** *At basetemperature, a dissipationless current flows through the junction. Increasing the bias current reveals a critical current of $I_C = 6.1\,nA$, followed by a flat curve. The features below the critical current are possibly due to imperfections in the interface, see text.*

Figure 6.2 shows the differential resistance of Device 1 at low biases, measured with an lock-in exciting current of $I_{ex} = 0.1\,\text{nA}$. Now, that the sample in the cryostat has thermalized to base temperature at $T = 17\,\text{mK}$, a dissipationless current flows though the nanowire Josephson junction, at bias currents within $I_{bias} = \pm 3\,\text{nA}$. At higher biases, a small but nonzero voltage drop is measured until large peaks appear at the critical current $I_C = 6.1\,\text{nA}$. The finite resistance between $3\,\text{nA}$ and $6\,\text{nA}$ could be caused by an imperfect interface, as it has been observed in Nb junctions on etched $(\text{Bi}_{1-x}\text{Sb}_x)_2\text{Te}_3$ nanowires [35], W junctions on milled Bi_2Se_3 flakes [37], as well as in other systems with nonideal interfaces [118].

6.1.2 TRANSPARENCY AND INDUCED GAP

By measuring the differential resistance up to higher bias currents, further information can be gained such that the nanowire Josephson junction can be characterized in terms of transparency and induced superconducting gap. Such a measurement must be continued up to at least twice the bias voltage corresponding to the superconducting gap of the Nb leads. This can be estimated with the help of the

transition temperature $T_{C,Nb} \approx 8.0\,\text{K}$ of the Nb leads measured during cooldown (measured in other device branches on the same chip, see Appendix A.2), using the BCS relation $\Delta(0) = 1.76 k_B T_C$,

$$\Delta_{Nb,leads}(0) \approx 1.2\,\text{meV}. \qquad (6.1)$$

Figure 6.3 shows the resulting I-V characteristic of Device 1. This curve is calculated from the current-biased differential resistance measurement via integration of the measured voltage drop.
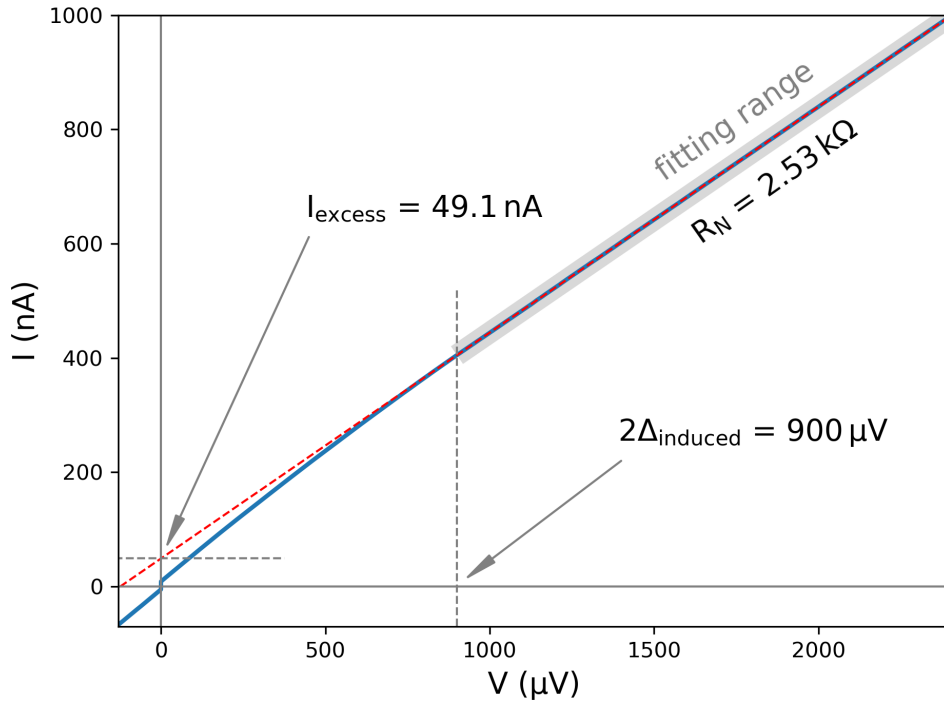
Figure 6.3: **Device 1: I-V characteristic.** *The data is taken in a differential, current based setup and the absolute voltage values are calculated via integration. Above 900 µV, the curve is linear, with a slope of $R_N = 2.53\,\text{k}\Omega$. Fitting a line to this section reveals an offset of $I_{exc} = 49.1\,\text{nA}$, the excess current. The induced superconducting gap can be estimated as half the onset of the linear regime, $\Delta_{induced} = 0.45\,\text{meV}$.*

When the bias current exceeds the critical current, the measured voltage increases abruptly. Upon further increase of the bias current, the curve approaches

a linear behavior in a rather featureless manner (differential conductance curve in Figure A.2). Only when the resulting bias voltage exceeds twice the energy scale of the induced superconducting gap, the I-V curve is expected to turn fully linear. This threshold can be visualized by fitting a linear function to the I-V curve, as shown in Figure 6.3. The slope indicates a normal resitance of $R_N = 2.53\,\text{k}\Omega$, and the linear regime begins at a bias voltage of 900 μV. The induced superconducting gap can be estimated as half of this value,

$$\Delta_{\text{induced}} \approx eV_{\text{linear}}/2 \approx 0.45\,\text{meV}. \tag{6.2}$$

In relative terms, this amounts to

$$\Delta_{\text{relative}} = \Delta_{\text{induced}}/\Delta_{\text{Nb,leads}}(0) = 0.375 \tag{6.3}$$

of the estimated superconducting gap of the Nb electrodes as fabricated.

Even though the I-V curve is linear above the $2\Delta_{\text{induced}}$ voltage threshold, this part does not extrapolate to zero, but is shifted by a remaining superconducting contribution. The so-called excess current can be determined by extrapolating the fitted line to zero bias voltage and taking the current axis intercept,

$$I_{\text{exc}} = 49.1\,\text{nA}. \tag{6.4}$$

With the extracted normal state resistance R_N, excess current I_{exc} and induced superconducting gap Δ_{induced}, the interface transparency can be calculated according to the OTBK theory (Section 2.4.6). Due to the rather small excess current and no significant subharmonic energy-gap structure, the onset of the linear regime is not clearly visible. Figure A.2 shows the differential conductance calculated by differentiation, which shows a clear break from linearity at 900 μV. Nonetheless, in order to accomodate a certain error of estimating a reasonable $2\Delta_{\text{induced}}$, it is calculated with a 10 % error, which yields qualitatively the same results (details in Appendix A.3.1). To show how this error translates, the error margins are included for the calculation steps of this device.

The interface barrier height can be determined after caluclating the fraction $\frac{eI_{\text{exc}}R_N}{\Delta_{\text{induced}}} = 0.28 \pm 0.03$ as

$$Z = 0.91 \pm 0.02, \tag{6.5}$$

6.1. NB JOSEPHSON JUNCTION ON BST NANOWIRE

The interface transparency then computes as $T = \frac{1}{1+Z^2}$,

$$T = 0.547 \pm 0.010. \tag{6.6}$$

This moderate transparency is consistent with the absence of a clear subharmonic gap structure [80, 82]. The relatively small error shows that the transparency does not change significantly if the fit parameters to the I-V curve are varied. Thus, it will be omitted in the discussion of the following devices. Next, the characteristic length scales of electron transport can be estimated based on the available numbers.

For the mobility, although literature values report larger values of $\mu > 1000\,cm^2/Vs$ [27, 38, 119–121], similar works have reported $\mu \approx 600\,cm^2/Vs$ [18] on etched $(Bi_{1-x}Sb_x)_2Te_3$ nanowires. From the electrostatic gating experiments in Chapter 5 mobilities of the order $\mu \approx 300\,cm^2/Vs$ can be estimated. This was done [122–124] by fitting the average slope of the conductance gating curve $G(V_{gate})$, and making use of the galvanic capacitances calculated from the same experiments. Essentially, $\mu \approx \Delta G/\Delta U \cdot L^2/C$ with L the channel length and $C = c_L \cdot L$ the galvanic device capacitance.

From the experiments in Chapter 5, mean free paths larger than the nanowire radius were concluded [2], however in device architechtures with much larger distance between the contact leads. In case of the Nb devices presented here, with much smaller contact distance-to-width ratio, the junction fabrication might have a more damaging effect on the TI. Analogous to [50], the mean free path can be calculated by $l_e = v_F \tau$ and $\tau = \hbar\sigma\sqrt{\pi/n}/(e^2 v_F)$, which yields $l_e \approx 6.8\,nm$. From similar works on Nb Josephson junctions on etched $(Bi_{1-x}Sb_x)_2Te_3$ nanowires, mean free paths were reported of $l_e = 2.29\,nm$ [35].

Using the estimated induced superconducting gap $\Delta_{induced} \approx 0.45\,mV$, the coherence length $\xi = \sqrt{\hbar D/\Delta_{ind}}$ with the diffusion constant $D = v_F l_e/d$ in d dimensions [125] can be calculated. Using $v_F = 4.4 \times 10^5\,m/s$ [58] and $l_e = 2\,nm$ in 3D as a lower bound, and $l_e = 50\,nm$ in 1D as an upper bound, the coherence length is expected to lie within $\xi \approx 20 - 180\,nm$.

Based on these numbers and a junction length of $L_N \approx 40\,nm$, the junctions can be assumed to be in the intermediate regime, at most quasi-ballistic but

rather diffusive. The intermediate regime makes generally sense, because surface states and the residual finite bulk contribution have different properties. In terms of length regime, the junctions can be assumed to be in the short limit since the junction length is shorter than the critical length $L_N < L_C \approx 3.65\xi$ [126], even for the lower estimate of the coherence length.

For this regime, the product of $I_C R_N = 15.4\,\mu V$ lies two orders of magnitude below the ideal value $1.32\pi\Delta_{ind}/e$ for short diffusive SNS junctions [126–128], which could be connected to the formation of a screened dipole layer at the interface [78].

6.1.3 MAGNETIC FIELD

At base temperature, the nanowire Josephson junction is measured in the field of a vector magnet in the three natural directions with respect to the nanowire orientation and the substrate, parallel to the nanowire axis as well as perpendicular, in-plane and out-of plane of the substrate. As before, differential resistance is measured with lock-in technique as a function of bias current, but now additionally as a function of magnetic field.

In the normal state, the TI nanowires have shown particular signatures of quasi-one-dimensional transport due to the quantum confinement of the circumferential direction of the topological surface states into sub-bands. In magnetic field, this concerns the field direction parallel to the nanowire axis, which gives rise to Aharonov-Bohm-like resistance oscillations 2.2.2. Individual sub-bands are shifted in energy, depending on their angular momentum around the lateral surface of the nanowire, which can now be probed in the superconductive state.

In the directions perpendicular to the nanowire axis, the main question is, whether Fraunhofer patterns emerge. These modulation patterns of the critical current are typically observed in larger Josephson junctions (Section 2.4.2). The magnetic flux through the N part of the Junction causes a phase gradient and therewith an oscillating current density along the width of the Junction, creating a slit-like diffraction pattern. However, in a quasi-one-dimensional system, this degree of freedom is missing, and the modulation pattern is not expected to

arise. Interestingly, since the nanowires are of comparable height and width, this measurement can be made in both perpendicular directions, in-plane as well as out-of-plane of the substrate plane.

In order to estimate the expected magnetic field periodicity of a potential Fraunhofer pattern, three factors must be taken into account. The projected area of the nanowire segment between the junction electrodes, the London penetration depth of the magnetic field into the Nb electrodes, and the flux focusing resulting from the expulsion of the magnetic field from the Nb electrodes. The scope of this estimation is to show that the absence of Fraunhofer patterns in the following measurements stems from the nanowire junctions being in the quasi-one-dimensional transport limit. The trivial case that the side-lobes of the pattern disappear simply due to the magnetic field exceeding the critical field, can be excluded by showing that the observed monotonous decay spreads to much higher fields than the expected Fraunhofer-pattern periodicity.

Estimation of Fraunhofer periodicity in out-of-plane direction. The effective magnetic flux through the N-part of the junction can be estimated as follows [23, 34, 129], illustrated in Figure 6.4. The effective length of the junction is longer than the visible nanowire link between the Nb leads, because the magnetic field can partly penetrate the superconductor of the order of the London penetration depth. Furthermore, the main part of the Nb electrodes expel the magnetic field due to the Meißner-Ochsenfeld Effect, causing the field between the centers of both electrodes to be focused towards the junction center, the so-called flux-focusing effect. However, since the relevant measure for the Fraunhofer pattern is the magnetic flux through the area of the effective N-part, the details of the field penetration into the superconductor can be neglected. Hence, the effective flux can be estimated by multiplying the applied field with the area, within which the field is focused towards the junction center,

$$\Phi = B(L_\mathrm{N} + 2 \cdot \frac{1}{2} L_\mathrm{Nb})W_\mathrm{N} = B \cdot A_\mathrm{eff,OOP}, \tag{6.7}$$

with L_N the lenght of the N-part of the Junction, i.e. the length of the nanowire link between the junction electrodes, L_Nb the length of the Nb electrodes, W_N the

width of the N-part (or nanowire), $A_{\text{eff,OOP}}$ the effective area and B the applied
magnetic field. Inserting the device dimensions $L_N = 40\,\text{nm}$, $L_{Nb} = 500\,\text{nm}$,
$W_N = 30\,\text{nm}$ yields

$$B_{\Phi_0,\text{OOP}} = \frac{\Phi_0}{A_{\text{eff,OOP}}} = \frac{\Phi_0}{(40\,\text{nm} + 500\,\text{nm}) \cdot 30\,\text{nm}} \approx 0.13\,\text{T} \qquad (6.8)$$

as the expected out-of-plane Fraunhofer periodicity.

Figure 6.4: *Schematic of the flux focusing effect in the nanowire
Josephson junction device: out-of-plane field direction.* *In order
to estimate the periodicity of a potential Fraunhofer pattern, the effec-
tive magnetic flux through the nanowire segment must be estimated.
Since the London penetration depth also increases the effective area
of the exposed nanowire, it can be neglected. The flux focusing due to
the expulsion of the field from the Nb electrodes is what significantly
increases the field in the junction center.*

Estimation of Fraunhofer periodicity in in-plane direction. Following the
same argumentation as for the out-of-plane direction, for the in-plane direction
of the magnetic field, an effective area for the calculation of the magnetic flux
can be estimated by increasing the lenght of the N-part of the junction by twice
the length scale, over which the magnetic field is focused from the Nb electrodes
towards the junction center. In this case however, since the magnetic field is ap-
plied parallel to the Nb film, the cross sectional area of the Nb it encounters is

much smaller. Hence, the focusing of the field towards the junction occurs only over a distance as large as half the film thickness, approximately. Any field passing further away from the central edge of the Nb electrode would rather be deflected above or below the Nb film [23]. Hence,

$$B_{\Phi_0,\text{IP}} = \frac{\Phi_0}{A_{\text{eff,IP}}} = \frac{\Phi_0}{(40\,\text{nm} + 35\,\text{nm}) \cdot 30\,\text{nm}} \approx 0.92\,\text{T}, \qquad (6.9)$$
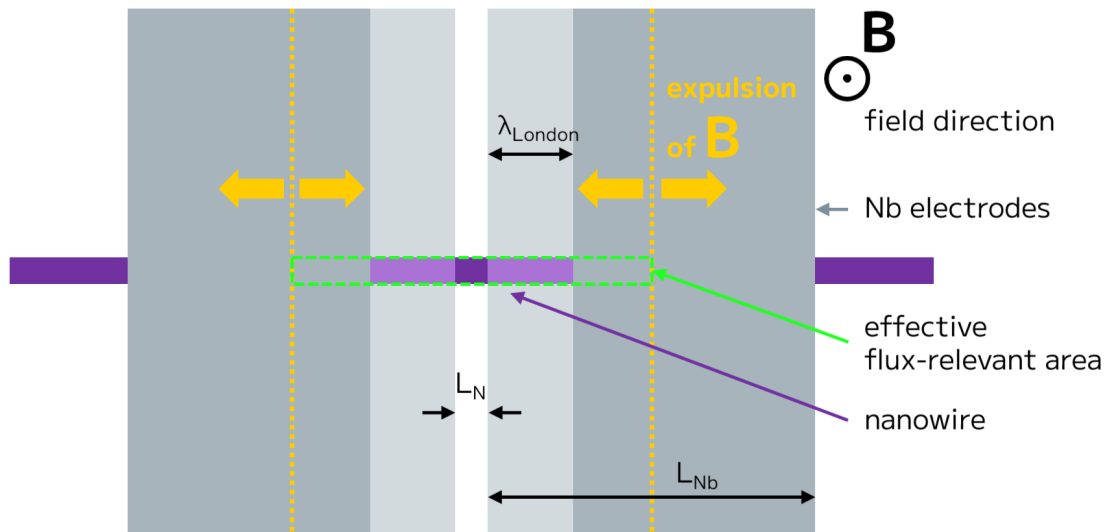
with $T_{\text{Nb}} = 35\,\text{nm}$ the Nb film thickness.
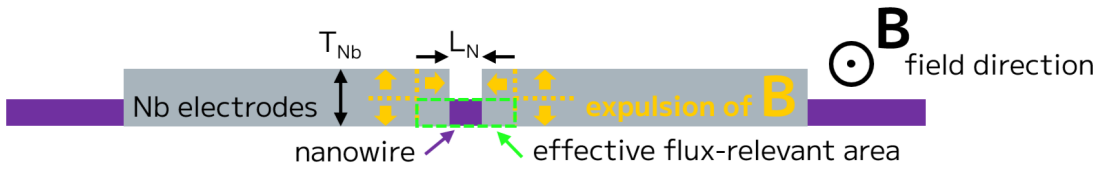
Figure 6.5: **Schematic of the flux focusing effect in the nanowire Josephson junction device: in-plane direction.** *Similar to the out-of-plane direction illustrated in Figure 6.4, the in-plane direction follows the same argumentation. However, the flux focusing effect is much less pronounced, because the projected area of the Nb contacts is much smaller due to the field direction being in-plane to the Nb film. Hence, the field is expelled only over a length scale of the order of half the Nb film thickness towards the junction center.*

Measurement. The differential resistance maps measured in magnetic field parallel, perpendicular in-plane and out-of plane to the nanowire on the device substrate are shown in Figure 6.6b and d. The bright line stems from the sharp peaks in the differential resistance, and can be retraced in order to find the critical current of the junction at each magnetic field value. The unusual choice of colorscale makes the identification of the normal state resistance possible by its narrow change in color at low values.

In both field directions perpendicular to the nanowire axis, the critical current is never reduced to zero, but is only at most reduced to half its zero-field value of 6 nA to roughly 3 nA. In-plane, the zero-resistance state and the switching current peaks persist in a damped manner up to the full field range of 1 T. Out-of-plane, where the flux focusing effect is much stronger and causes the effective field through the junction to be several times higher, the critical current

is still not reduced to zero, but the entire curve is smeared out above a magnetic field strength of 0.6 T. Hence, in both perpendicular directions to the nanowire axis, no Fraunhofer diffraction pattern is observed, even though, according to the estimation in the previous sections, a destructive interference - and therewith a switching current reduction to zero - would be expected around a field scale of 0.92 T and 0.13 T, respectively. These findings are consistent with the quasi-1D-limit observed in the normal state.

Both perpendicular directions show a noticeable fluctuation on top of the monotonous decay of the switching current, which have at least the following two origins. On the one hand, the discontinuities appearing as vertical cuts through the heatmap, repeating the pattern of a slightly lower field scale, stem from magnetic flux jumps. The Nb leads in these devices are fabricated in a tapered shape from the large bonding pads to the small junction leads (as shown in Figure 3.1b). Therefore, apart from the sudden formation of vortices in the type II superconducting electrodes, which abruptly change the effective flux through the junction in a step-wise manner, these can also migrate with increasing field towards the junction, in the direction of the lead narrowing, resulting in a gradual distortion of the pattern. As expected, these occur at a much higher frequency in the out-of-plane direction.

On the other hand, $(Bi_{1-x}Sb_x)_2Te_3$ nanowires are prone to charge jumps. Trapped charges, sudden changes in the disorder landscape, fluctuations of the chemical potential throughout the crystal influence transport in a complicated way. Apart from simply occuring randomly over time [1, 2], the application and change of magnetic field can trigger these as well, causing step-wise changes in transport behavior (Section 4.9.2).

In the field along the nanowire axis, Figure 6.6c, the zero resistance and the pronounced switching current peak begin to blur above 1.5 T, but superconductivity persists at least up to the measured field range of 3 T. In this field direction, the Nb film has the least projected area and only a few flux jumps occur. The oscillation of the switching current on top of its monotonous decrease, being much smoother compared to the other field directions and at a lower field peri-
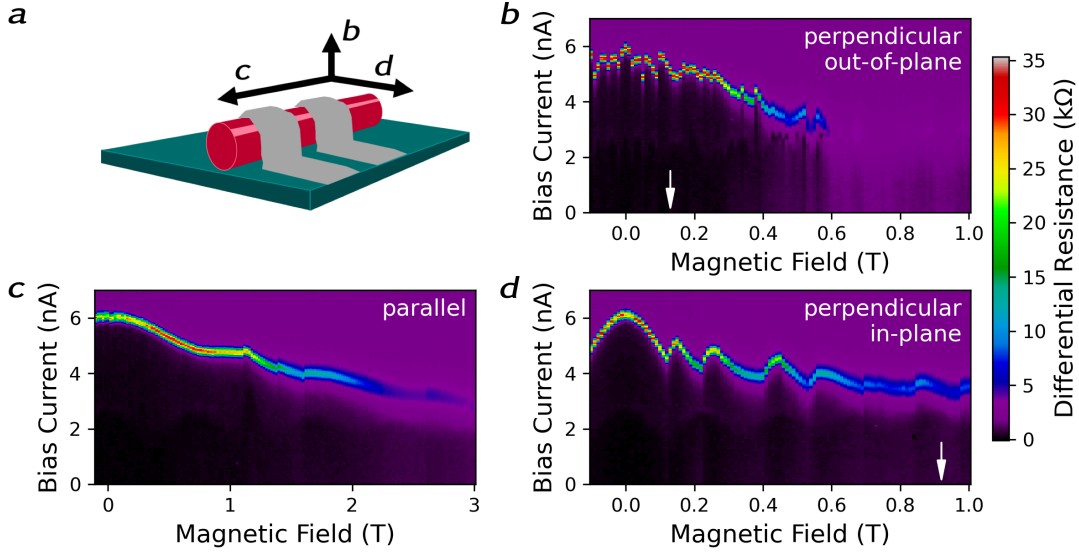
Figure 6.6: **Device 1: Differential resistance in magnetic field.** *Bright line shows the switching current. **a** Schematic of field directions with respect to nanowire orientation. **b, d** Perpendicular field out-of- and in-plane, showing no Fraunhofer pattern, which would be expected to reduce the critical current to zero at approximately $0.13\,\mathrm{T}$ and $0.92\,\mathrm{T}$, respectively (white arrows). Instead, the critical current persists with more than half its zero-field value up to $1\,\mathrm{T}$ and $0.6\,\mathrm{T}$, respectively. The absence of Fraunhofer patterns in perpendicular field is consistent with the quasi-1D picture of the induced superconductivity. **c** Field along the nanowire axis with surviving zero-resistance state over the measured field range of $3\,\mathrm{T}$ and potential signs of AB-like oscillations.*

odicity, reasonably matches possible AB-like oscillations. The concrete periodicity is however obscured by the interruptions. The strongest among these, occurring at $B_{\parallel} = 1.1\,\mathrm{T}$, resembles the typical charge jumps in magnetic field. These not only cause step-wise changes in resistance, but also switch abruptly from one exemplary AB-like oscillation mode to a completely different one, similar to what is observed in the normal-state magnetoresistance.

Now that the induced superconductivity in $(\mathrm{Bi}_{1-x}\mathrm{Sb}_x)_2\mathrm{Te}_3$ nanowires has been observed and measured with niobium as superconductor, the next section shows the results on another type of device in which vanadium is used as super-

conductor in the Josephson junction.

6.2 TiVTiAl Josephson junctions on BST nanowires

Ongoing research by P. Umesh showed that Josephson junctions can be fabricated by using the stacked metals Ti/V/Ti/Al on $BiSbTeSe_2$ flakes. A complication is the mechanical strain resulting from the mismatch between V and BSTS. This 4-layered metallization makes use of a Ti buffer layer, which is repeated above the V layer to reduce the strain, as well as an Al layer, protecting from oxidization from above. Similarly, in this work, $(Bi_{1-x}Sb_x)_2Te_3$ nanowire Josephson junctions were fabricated with TiVTiAl metallization (details in Section 3.2.7), to investigate the proximitization on the VLS grown BST nanowires. In the following sections, elecronic transport measurements at cryogenic temperatures are shown, similarly to the measurements performed on the Nb Josephson junctions.
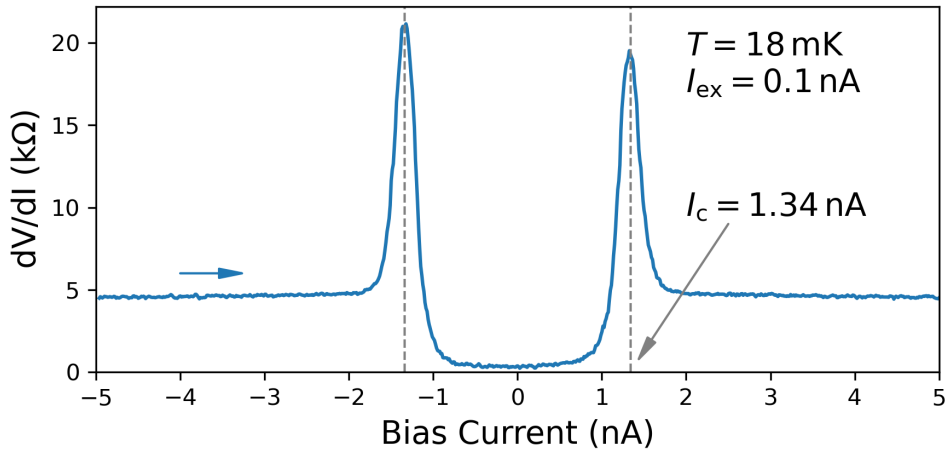
Figure 6.7: **Device 2: Differential resistance in dependence at low bias currents.** *A dissipationless current flows through the junction at low bias. The critical current peaks around $I_C = 1.34$ nA appear to be thermally broadened, see text.*

At base temperature, the voltage drop over the junction disappears almost completely, and the supercurrent survives up to a bias of 1.34 nA. The shape of the differential resistance sweep shown in Figure 6.7 is broadend to a certain extent. The small resistance at zero bias increases upon approaching the I_C-peaks which are widened as well. Thermal broadening and noise contribution are potential

reasons for this, since the Josephson coupling energy calculated from the critical current is not much larger than the thermal energy scale at the base temperature of 18 mK, namely $E_J(1.34\,nA) \approx 32$ mK [66].

6.2.1   TRANSPARENCY AND INDUCED GAP

By extending the differential resistance measurement to high bias currents, the I-V characteristic, shown in Figure 6.8, is obtained through integration. Fitting a line to the linear regime and extrapolating it to zero voltage yields an excess current of $I_{exc} = 21.3$ nA. The linear region extends down to 0.66 mV, hence the induced superconducting gap can be estimated as

$$\Delta_{induced} = 0.33\,\text{meV}, \tag{6.10}$$

and the OTBK transparency then yields

$$T = 0.571 \tag{6.11}$$

The normal state resistance of $R_N = 5.33$ kΩ suggests that the nanowire is bulk-insulating. To put this estimated induced superconducting gap in relation to the pristine V, the literature value must be taken due to the lack of cooldown data of the fabricated TiVTiAl leads. With a critical temperature of $T_C = 5.45$ K [130], the estimated superconducting pairing gap would be $\Delta(0)_V = 1.76k_B T_C = 0.83$ meV. Comparing the induced gap extracted from the I-V curve yields

$$\Delta_{V,\text{relative}} = \Delta_{V,\text{induced}}/\Delta_{V,\text{leads}}(0) = 0.398. \tag{6.12}$$

6.2.2   MAGNETIC FIELD

In magnetic field, the differential resistance behaves similarly to what was observed in the Nb measurements. In both field directions perpendicular to the nanowire, in-plane and out-of-plane of the substrate surface, there are no signs of a Fraunhofer pattern. Similarly as done for Device 1 in Section 6.1.3, the magnetic field expected to create the first Fraunhofer dip can be estimated as follows. The
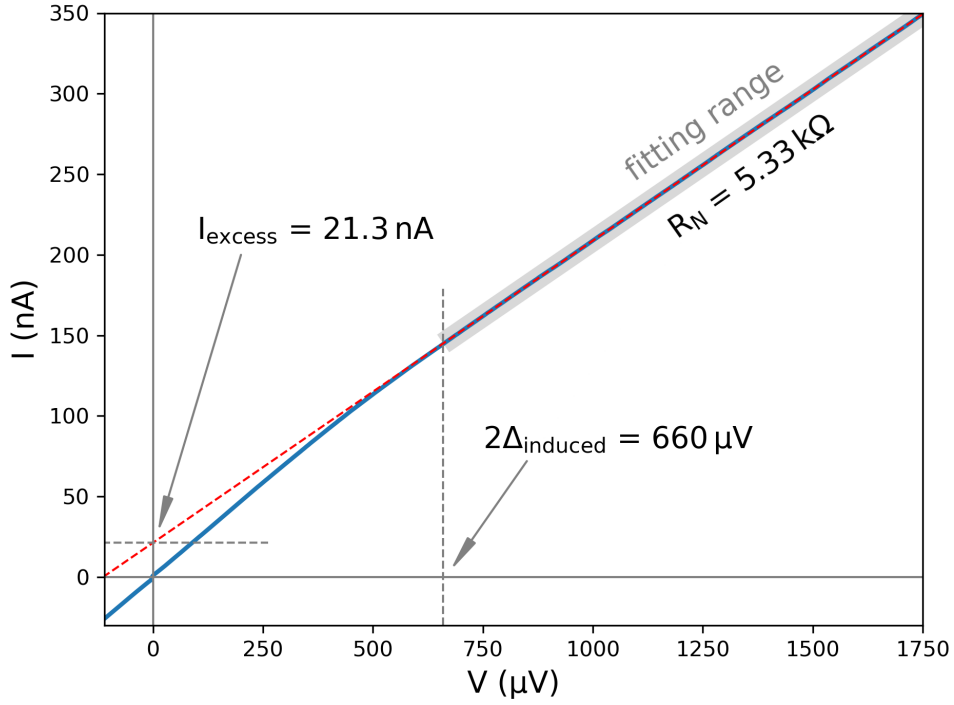
Figure 6.8: **Device 2: I-V characteristic.** *Data integrated from a differential resistance measurement. Linear curve fit for extraction of* $I_{exc} = 21.3\,\mathrm{nA}$, $R_N = 5.33\,\mathrm{k\Omega}$ *and* $\Delta_{induced} = 0.33\,\mathrm{meV}$

nanowire segment between the junction electrodes has a width of 30 nm and a length of 100 nm, the TiVTiAl electrodes are 45 nm thick and the flux focusing is estimated to occur over a distance of 500 nm as before. Thus, the maximal magnetic field expected to cause a Fraunhofer dip computes as

$$
\begin{aligned}
B_{\Phi_0,\mathrm{IP}} &= \frac{\Phi_0}{A_{\mathrm{eff,IP}}} = \frac{\Phi_0}{(100\,\mathrm{nm} + 45\,\mathrm{nm}) \cdot 30\,\mathrm{nm}} \approx 0.48\,\mathrm{T} \\
B_{\Phi_0,\mathrm{OOP}} &= \frac{\Phi_0}{A_{\mathrm{eff,OOP}}} = \frac{\Phi_0}{(100\,\mathrm{nm} + 500\,\mathrm{nm}) \cdot 30\,\mathrm{nm}} \approx 0.11\,\mathrm{T}
\end{aligned}
\tag{6.13}
$$

for the in-plane (IP) and out-of-plane (OOP) direction, respectively.
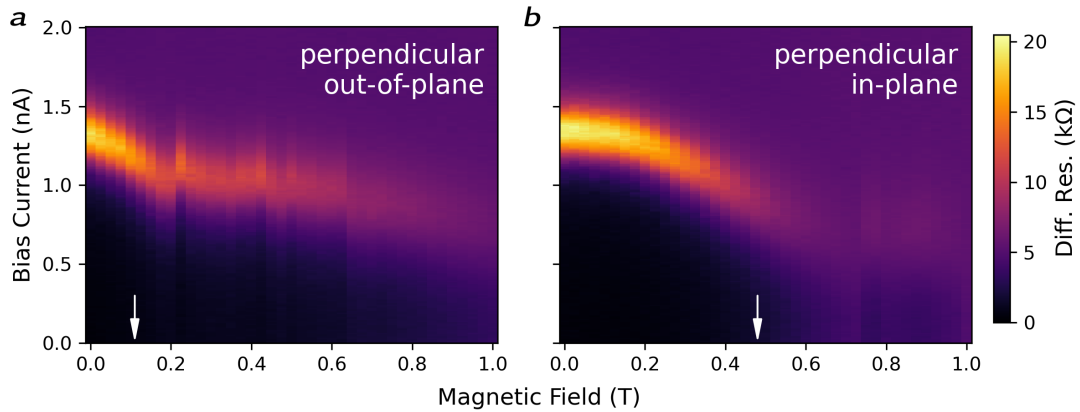
Figure 6.9: **Device 2: Differential resistance in magnetic field.** *Differential resistance in dependence of bias current, in both magnetic field directions perpendicular to the nanowire axis. White arrows mark the expected first zero crossings if a Fraunhofer pattern was present.* **a** *In-plane and* **b** *out-of-plane of the substrate surface.*

6.2.3 TOPOLOGIAL SURFACE STATES

Figure 6.10 shows the effects of changing the chemical potential in the nanowire by electrostatically charging the backgate of the substrate. The critical current increases and decreases repeatedly upon changing the gate voltage, following the inverse behavior of the normal state gating curve. Depending on the location of the chemical potential, alternating oscillations in magnetic field parallel to the nanowire axis can be observed, which could be of AB-like origin.
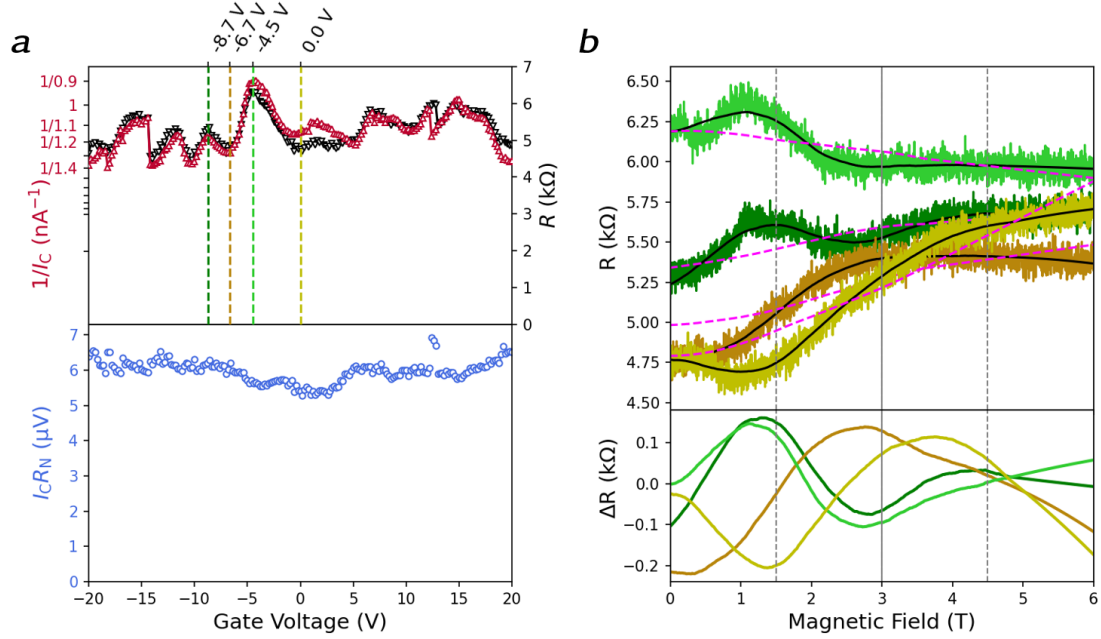
Figure 6.10: **Device 2: Signatures of the topological surface states in the TiVTiAl Josephson junction on a BST nanowire.** **a** Above: Inverse critical current measured at different gate voltages, in comparison to the normal-state gating curve. Below: Gate voltage dependence of $I_C R_N$, calculated from the values above. **b** Magnetoresistance (above) and background-subtracted oscillations (below) inside the NW junction at four distinct gate voltges, -8.7 V, -6.7 V, -4.5 V and 0 V, where the gating curve shows consecutive peaks and dips, marked with color-matched dashed lines.

In order to obtain the gating curve of the nanowire normal resistance, a constant bias current above the critical current is set of $I_{bias} = 2$ nA. Then, the gate voltage is changed while the resistance of the nanowire is measured. The upper subplot of Figure 6.10a compares this curve (black) with the critical current measured at different gate voltages, plotted as its inverse (red). Both curves show a strikingly similar behavior, increasing and decreasing repeatedly with gate voltage. The horizontal spacing of these up and down movements in terms of gate voltage is consistent with the expected magnitude for the the TSS sub-band spacing [1]. Thus, it is possible that some of these fluctuations originate from the chemical potential crossing the size-quantized TSS sub-band bottoms.

However, it must be noted that a conclusive association of such oscillations in the gating curve with specific subband crossings in the nanowire is a complicated task [17].

The magnetoresistance curves shown in panel b are measured at consecutive minima and maxima of the gating curve. They likely contain contributions of AB-like as well as AAS oscillations of half the periodicity. Since the expected AB-periodicity lies within $3\,\mathrm{T}$, and $6\,\mathrm{T}$, maximally two periods can be observed within the measured field range of $6\,\mathrm{T}$. Additionally, the low field oscillations are usually distorted from the strong weak antilocalization dip, making the identification of the AB-like oscillation modes difficult, without enough visible oscillation periods at higher fields. Only one of the measured magnetoresitance curves shows a prototypical AB-like oscillation, the one measured at $V_{\mathrm{gate}} = -6.7\,\mathrm{V}$, namely the 0-ABLO mode, in which the resistance is highest at $\Phi_0/2$. However, a distinct appearance of the magnetoresistance curves measured at resistive peaks versus the curves measured at resistive dips can be made out.

The lower part of Figure 6.10a shows the product $I_\mathrm{C}R_\mathrm{N}$ calculated from the resistance and switching current values measured versus gate voltage plotted above. The curve is approximately constant over the measured voltage range within $\pm 10\,\%$, with the highest values on the sides and the lowest value in the center, around $0\,\mathrm{V}$.

The average of $I_\mathrm{C}R_\mathrm{N} = 5.97\,\mathrm{\mu V}$ lies more than orders of magnitude below the ideal value $1.32\pi\Delta_{\mathrm{ind}}/e$ for short diffusive SNS junctions [126–128]. Similar I_C and R_N dependencies have been observed in Al junctions on BiSbTeSe$_2$ flakes [34] and Al-InAs nanowire junctions [125, 131], and without gating dependence on W-Bi$_2$Se$_3$ [37], all with higher absolute $I_\mathrm{C}R_\mathrm{N}$ compared to the superconducting gap. A probable reason for the low $I_\mathrm{C}R_\mathrm{N}$ values presented here is the formation of a charge-accumulation layer at the interfaces which can significantly suppress the critical current [78]. The Fermi energy mismatch between superconductor and TI nanowire makes the transparency of the S-N interface drop rapidly, which makes it become essentially a S-I-N interface with an insulating barrier in between, as described in Section 2.4.3. Changing the chemical potential by electrostatic gating

only has effect in the TI nanowire and not in the superconductor, where the Fermi energy is pinned. It is therefore reasonable to expect that the charge accumulation layer at the interface - and hence the $I_C R_N$ product - cannot easily improve with gate voltage.
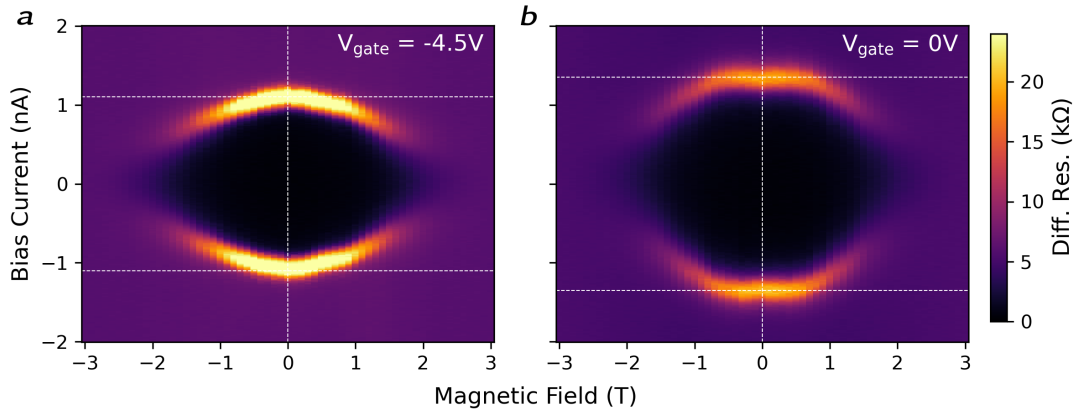
Figure 6.11: **Device 2: Differential resistance in parallel magnetic field. a** *Measured at a gate voltage of $V_G = -4.5$ V on the highest resistive peak of the gating curve (Figure 6.10a, bright green dashed line), the switching current decreases monotonically with field and the supercurrent fades out around 2 T.* **b** *At $V_G = 0$ V (bright yellow dashed line), in a resistive dip of the gating curve, the switching current increases symmetrically in field and bias current from zero field to 0.5 T, and decreases monotonically in a similar manner. Dashed lines as guide to the eye showing the symmetry and absence of hysteresis in both directions, horizontal lines at ± 1.1 nA and ± 1.35 nA. Both measurements are swept in bias current and stepped in magnetic field both from negative to positive values.*

Figure 6.11 shows the differential resistance measured in magnetic field along the nanowire axis at two different gate voltages. The two distinct situations in the gating curve are shown by the bright green and yellow dashed lines in Figure 6.10a, on the top of the highest resistive peak within the measured gate voltage range, and inside a dip next to it. While both heatmaps show a similar monotonic decay at higher fields and the dissapearance of the Josephson current around $B_\parallel = 2$ T, their low-field behavior is different. The measurement within the resistive dip shows an increase of switching current with magnetic field below 0.5 T, which is

a rather unusual phenomenon.

An elevation of switching current with magnetic field has been observed in Al Josephson junctions on Ag, InAs and InSb nanowires [77, 131, 132] and has been attributed to quasiparticle thermalization or even topological effects, but none of the settings are applicable to the present case. The quasiparticle thermalization effect has been attributed to a change of hysteresis between switching and retrapping current [133] in a 4-probe setup, which are both not present in the measurements presented here. The white dashed lines are guides to the eye for the purpose of showing the symmetry of the measured patterns in terms of magnetic field as well as bias current.

In the present case, the increase of the switching current at low fields could have a different origin, in line with the aforementioned observations. The low-field behavior of the magnetoresistance in Figure 6.10b shows a different trend at the respective gate voltage locations, and could therefore cause a certain increase or decrease of I_C in low field. The fact, that the low-field increase is associated with a resistive dip and the monotonic decrease with a resistive peak, is somewhat counterintuitive, when compared to the commonly known simple chess-pattern-like picture of AB-like oscillations and TSS sub-bands. However, a major insight from the published work in Chapter 5 are new criteria for the association of resistance peaks in gating curves to sub-band energies. In the weak-scattering limit, a resistive peak arises whenever the chemical potential crosses a sub-band bottom edge, due to the sharp increase of scattering probability across sub-bands. Therefore, the simple picture that any resistive peak in the gating curve comes from the chemical potential being in-between of sub-band bottom edges and will therefore be lowered with magnetic field which splits the neighboring sub-bands towards conduction and vice-versa is not directly applicable here.

6.3 COMPARISON

Josephson junction on $(Bi_{1-x}Sb_x)_2Te_3$ nanowires using two different superconductors were shown, Nb and V enclosed in the stack TiVTiAl. Table 6.1 lists the

values, that were extracted from the differential resistance measurements as well as from the integrated I-V curve. On an absolute scale, the Nb junction shows a larger induced superconducting gap, which is in line with the fact that bulk Nb has a larger bulk gap than V. However, the relative value $\Delta_{\text{rel}} = \Delta_{\text{ind}}/\Delta_{\text{leads/bulk}}$, in which the induced gap is compared with the bulk value, is slightly higher for TiVTiAl. Here it must be noted, that due to the absence of cooldown data, the induced gap of TiVTiAl was compared to the literature bulk value for V, instead of the estimated gap based on the on-chip critical temperature of the leads, as it was done for Nb. If the same had been done for Nb, in a comparison with the literature bulk value, the difference between both relative induced gaps would be approximately 30 %.

Device (SC)	R_{N}	I_{c}	I_{exc}	Δ_{ind}	T	$\Delta_{\text{ind}}/\Delta_{\text{leads/bulk}}$
1 (Nb)	2.53 kΩ	6.1 nA	49.1 nA	0.45 mV	0.547	0.375
2 (TiVTiAl)	5.33 kΩ	1.34 nA	21.3 nA	0.33 mV	0.571	0.398

Table 6.1: ***Comparison between the extracted values of the shown devices, characterizing the proximitization of Bi$_2$(Te$_x$Se$_{1-x}$)$_3$ nanowires by Nb and TiVTiAl.*** *The absolute values of the induced gap are larger for Nb, but on a relative scale, TiVTiAl lies slightly above. It must be noted, that in the TiVTiAl case, the induced gap was compared to the literature bulk value, while the Nb values were only compared to the gap calculated from critical temperature of the fabricated leads, which is lower than the literature bulk value. In terms of transparency, the TiVTiAl junction also shows a slightly higher number.*

In terms of OTBK transparency, the value calculated for TiVTiAl lies again above the result for Nb, but the difference is much smaller. Since none of these transparencies are particularly high, from a qualitative perspective they are both in the same regime, and for a more reliable comparison, more devices would need to be measured.

6.4 TUNNELING SPECTROSCOPY ON PROXIMITIZED TI NANOWIRES

For the following series of experiments, more elaborate device architectures were conceived, for the purpose of directly measuring the density of states in the proximitized TI nanowires. The devices shown are the two first working generations of such devices and are therefore a proof of principle and the first steps towards reliably fabricating such devices. Here, the Nb-BST Josephson junction devices are capped with a thin layer of Al_2O_3, and normal metal tunneling electrodes from Pt/Au are defined. These are made narrow and placed as close as possible to the superconducting leads. For a more detailed description of the fabrication see Section 3.2.8.

Figure 6.12 shows tunneling spectroscopy at the edge of two Josephson junctions in magnetic field parallel to the nanowire axis, along with SEM images of the devices. Within certain field ranges, reduced densities of states around zero bias voltage was measured. In the case of panels a and c, this is only observed with a field in the range of $2 - 4.5$ T. The linecuts at 0 T and 6 T only show a number of unidentified features at a sub-millivolt scale, which seem to shift with increasing field in individual directions roughly by the same order of magnitude. These are unlikely linked to any TSS sub-band physics, since the expected energy spacing of the sub-bands is of the order of 15 meV, see Section 2.2.1.

The line cut at 3.2 T however, which passes through the middle of the trench in tunneling conductance, shows a clearly visible dip around zero bias voltage, which is also its global minimum. On both sides it rises into two roughly symmetric shoulders that are approximately 350 mV apart. In the Nb-nanowire Josephson junction devices, an induced superconducting gap of $\Delta_{induced} \approx 0.45$ meV was estimated (Section 6.1.2). Such narrowed dips (compared to the induced gap) with faint shoulders is have been observed in tunneling electrodes on proximitized conductors at macroscopic distances of the proximitizing superconductor [134].
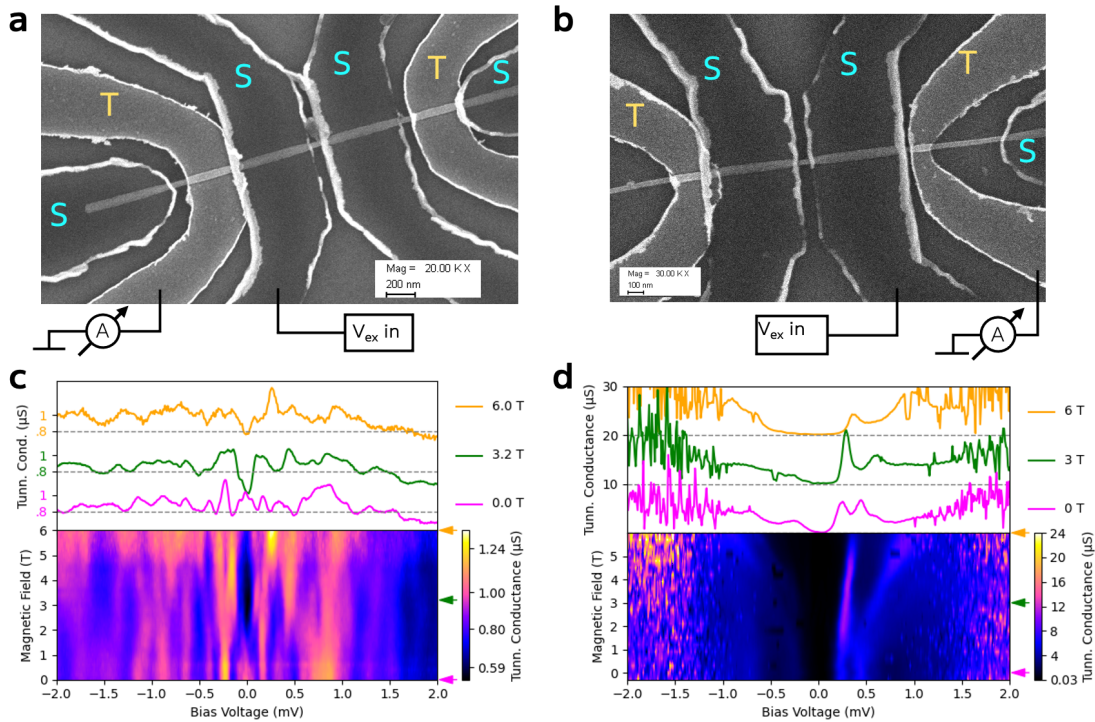
Figure 6.12: **Tunneling spectroscopy on proximitized BST nanowires in parallel magnetic field, devices 3 and 4. a, b** *SEM images of Device 3 and Device 4, with the respective tunneling measurements shown in* **c** *and* **d**. *S denotes superconductor (Nb) and T tunneling contact (Pt/Au). The fabrication from* **a** *was improved and narrower tunneling contacts were obtained in* **b**, *that are as close as possible to the S lead, if possible without direct contact.* **c** *Lower plot: Tunneling spectroscopy in magnetic field up to* 6 T *parallel to the nanowire axis. Upper plot: Linecuts at zero, intermediate and highest field, with individual offset for visibility and dashed lines as guide to the eye at 0.8 μS, each. Around zero bias, a dip of reduced density of states forms in intermediate field and closes again towards maximum field. The field scale of roughly* 6 T *equals the expected periodicity of AB-like subband physics.* **d** *With the much narrower tunneling electrode, a vanishing density of states is measured around zero bias. Note that the tunneling electrode is visibly not in direct contact with the superconducting lead. Strangely, the valley of suppressed density of states widens successively with increasing field without stagnation within the measured range. Curves offset by 10 μS for visibility.*

Given the reasonable suspicion, that the majority of the tunneling current could flow through one or a few pinholes in the tunneling barrier, the relevant length scales involved can be estimated. Using the provided relationship of the characteristic energy scale at distances x from the superconductor $E_{\text{char}} \approx \hbar D/x^2$ [134], and the lower and upper bounds for the mean free path used for the coherence length estimation in Section 6.2.1 of $l_e \approx 2 - 50\,\text{nm}$ for the diffusion constant D, the energy scale of the observed shoulders could correspond to a distance in the range of $30 - 300\,\text{nm}$ from the superconducting electrode. This is in line with the device layout, which can be seen in panel a, showing a tunneling electrode (bright grey) that extends over a distance of approximately $300\,\text{nm}$ from the Nb contact. Although the induced superconductivity in the nanowire is unlikely to persist above a longitudinal field of $3\,\text{T}$, and furthermore, the depth of the dip in tunneling conductance is also expected to become more shallow with field [134], this dip in the density of states could still arise because of a significant increase of the coherence length and mean free path in the surface states with half a flux quantum through the nanowire cross section around a field of $3\,\text{T}$, since the observed signal could be highly sensitive on the distance.

Keeping in mind the required periodicity of roughly $6\,\text{T}$ for any AB-like physics in TI nanowires of this diameter, it is tempting to interpret the appearance, the vertical extent and the disappearance of the trench as a periodic effect. This however is hardly verifiable, on the one hand due to $6\,\text{T}$ being the maximum field of the cryostat, and on the other hand because at higher fields, superconductivity is unlikely to persist anymore.

Panel c of Figure 6.12 displays the tunneling spectroscopy through a much more narrow tunneling electrode, as can be seen in panel b. At zero bias, a clearly vanishing tunneling conductance can be seen, with a reduction of more than $99\,\%$ in comparison with the curve average. Visibly, the tunneling electrode is not in direct contact with the junction lead, meaning that the tunneling current must be flowing through the nanowire instead of directly tunneling into the Nb electrode. Thus, the valley may to stem from a vanishing density of states in the nanowire. Whether the adjacent shoulders give information about the magnitude of the

induced superconducting gap is unclear, because the positive side is overlaid with two higher peaks which could be caused by impurities.

With increasing field the valley broadens, which again raises the question whether AB-like physics are involved. However, the fact that up to 6 T, it is successively becoming wider with increasing field without a visible stagnation within this range, does not fit into that picture. It catches the eye how all curves suddenly become much noisier at positive and negative bias voltages larger than 1 mV. It is unclear whether there are hidden coherence peaks of the Nb leads behind, or whether the sudden onset of the noise itself is caused by the Nb electrodes turning normal conducting.

7

CONCLUSION AND OUTLOOK

In this work, TI nanowires were grown, optimized, and successfully proximitized by two superconductors. Low-temperature electronic transport was studied in the normally conducting as well as in the superconducting state, leading to the following main achievements.

- Nanowires out of two ternary TI materials, $(Bi_{1-x}Sb_x)_2Te_3$ and $Bi_2(Te_xSe_{1-x})_3$, were grown reproducibly in bulk-insulating compositions in shapes exhibiting circumferential size-quantization of the topological surface states (TSS) into sub-bands.

- The resulting transport properties were studied at low temperatures in the normally conducting state, exhibiting Aharonov-Bohm-like oscillations in magnetic field as well as resistance oscillations during changing the chemical potential, of which the latter were not observed and associated to the sub-band index before, to the best knowledge of the author.

- TI nanowires were made superconducting by the proximity effect with the

help of two different superconductors, Nb and V. Transport was studied at ultra-low temperatures, exhibiting similar effects as in the normal state and suggesting that the topological surface state sub-bands are proximitized by the superconductor.

- First attempts of tunneling spectroscopy were successfully made on devices specifically developed for that purpose, paving the way towards more precisely resolving the density of states in proximitized TI nanowires by tunneling spectroscopy.

Vapor-Liquid-Solid growth has proven to be one of the methods of choice for growing nanocrystals in a variety of shapes. For this work, bulk-insulating nanowires with diameters of roughly $30 - 40\,\mathrm{nm}$ were needed, such that the circumferential direction of motion is quantized with an energy spacing large enough to perform sub-band-sensitive transport experiments, while at the same time, the nanowire cross section can be penetrated by more than half a magnetic flux quantum, whithout destroying superconductivity in the respective devices. Furthermore, the composition of the ternary TIs needed to be bulk-insulating and as constant as possible between different nanowires from the same growth and across each individual nanowire individually, such that the TSS physics can be measured in a meaningful way in fabricatably sized devices. To achieve this, a number of stable sets of VLS-growth-parameters have been found and fine-tuned, out of which three are presented in particular, two for $(\mathrm{Bi}_{1-x}\mathrm{Sb}_x)_2\mathrm{Te}_3$ and one for $\mathrm{Bi}_2(\mathrm{Te}_x\mathrm{Se}_{1-x})_3$.

Nanowire devices for transport measurements are difficult to fabricate and can have a particularly low yield. Hence, a reliable fabrication protocol was established including specifically creating software for device fabrication from randomly transferred naturally grown crystal samples, which is suitable for the entire range between simple and very elaborate device architectures. Most devices in this work were fabricated in this way, within a fraction of the time needed for and with a fraction of the errors usually made during manual device design.

At liquid He temperature and below, electronic transport was measured in normally conducting nanowire devices. Upon changing the chemical potential in

the TI by electrostatic gating, reproducible oscillations arise in the resistance that could be traced back to originate from two adverse effects. On the one hand, the diverging density of states at each TSS sub-band causes conductance boosts to arise that are super-linear, almost entirely quadratic, in gate voltage. On the other hand, each newly available sub-band enhances scattering and therewith decreases conductance, in the same gate voltage pattern. In the weak scattering limit, which can be generally assumed for these nanowire dimensions, scattering outweighs the density of states contribution which leads to resistive peaks whenever the chemical potential is pushed past a sub-band bottom edge. These findings should be investigated further, especially with respect to magnetic field. If the resistive peaks appear when the chemical potential crosses a sub-band bottom edge instead of in-between, then the expected magnetoresistance effect might be contrary to the picture up to now, as it was observed in the TiVTiAl Josephson junctions on $(Bi_{1-x}Sb_x)_2Te_3$ nanowires.

In magnetic fields parallel to the nanowire axis, the topological surface state sub-bands can be shifted in energy, due to their characteristic property of spin-momentum locking. As a result, the so-called Aharonov-Bohm-like oscillations can be measured, which were observed in nanowires out of both materials. These AB-like oscillations could be identified and distinguished from other types of resistance oscillations by periodically phase-shifting between 0- and π-phase through change of the chemical potential. They are a key signature of resolving and manipulating the quantum-confined topological surface state sub-band spectrum, a crucial step towards realizing Majorana fermions in TI nanowires.

As a next step, superconductivity was induced in the $(Bi_{1-x}Sb_x)_2Te_3$ nanowires through the proximity effect in Josephson junction devices from two different superconductors, Nb and V (in the stack TiVTiAl). In both cases, the topological surface state sub-band signatures measured in the normal state reappeared under superconductivity as follows. The critical current oscillates with the gate voltage, following the normal state conductivity oscillations measured in the same Josephson junction at bias currents above the critical current. These oscillations are likely to originate from the topological surface state sub-band physics, suggest-

ing that the topological surface state is proximitized, another crucial ingredient for superconducting TI nanowire devices, especially for the purpose of generating Majorana fermions.

Measuring the critical current in magnetic fields perpendicular to the nanowire axis showed further signatures of quasi-one-dimensional transport, supporting the preceding conclusions. A decay of the critical current with increasing field was observed instead of the typically emerging Fraunhofer pattern, an interference pattern that is commonly used to characterize Josephson junctions with nonzero cross-sectional area. These observations are consistent with the picture in which the nanowires are wrapped by a one-dimensional superconducting surface states in which the perpendicular direction of motion is quantized in angular momentum.

The comparison between the proximitation by Nb and V yields the following results. The calculated OTBK transparencies of the Nb and TiVTiAl Josephson junctions are not particularly high and roughly similar with 0.547 and 0.571, respectively. However, comparing the induced superconducting gaps on a relative scale shows, that a slightly higher percentage of the bulk energy gap was induced in the case of TiVTiAl. Although these differences and the number of measured devices are too small to draw a clear conclusion about which superconductor proximitizes the nanowires better, TiVTiAl has shown to be a promising candidate and could be investigated further.

Lastly, tunneling spectroscopy was done through thin insulating barriers and contacts fabricated as close as possible to the superconducting Nb leads on the $(Bi_{1-x}Sb_x)_2Te_3$ nanowires. Serving as the first attempts towards precisely resolving the densities of states in the normal and the superconducting state, fabrication protocols were established that enable the successful fabrication of TI nanowire devices featuring Josephson junctions with narrow and closely placed tunneling electrodes. The tunneling current was measured in dependence of bias voltage across the barrier, and indications of significantly reduced densities of states around zero bias were observed in close proximity to the Nb leads. Changing the chemical potential by electrostatic gating was however not successful in these samples, and an effect of the magnetic field was observed, but no conclu-

sive observations could be made yet. The established fabrication protocol can be applied for further tuning of the tunnel barrier and tunnel electrode placement. This kind of measurement should be made on varying locations on the nanowire, in the normally conducting and in the proximitized regions, as well as at different distances from the superconducting electrodes. Scanning tunneling spectroscopy measurements would be a very suitable follow-up endeavor as well.

With respect to nanowire Josephson junctions, the reported measurements should be continued as well in dependence of temperature. Different contributions of the bulk and the surface states to the Josephson current could be identified. Furthermore, the interface transparencies must be improved, such that the $I_C R_N$ product increases and that multiple Andreev reflections can be observed. Furthermore, larger nanowire diameters might be of benefit, because more sub-bands may be observed with respect to gate voltage and magnetic field strength, making the association with theory more feasible. Furthermore, the relevant magnetic field scales would be more compatible with superconductivity.

Finally, the VLS growth of nanowires has a vast parameter space and it may be possible to significantly improve the quality of the nanowires presented in this thesis. The proximitization of $Bi_2(Te_xSe_{1-x})_3$ nanowires should be investigated as well, because of the suspicion that they are less affected by oxidization and related degradation. If the growth of the $(Bi_{1-x}Sb_x)_2Te_3$ nanowires can be further improved, the charge instabilities might be further reduced which could offer a much higher performance in device measurements.

A
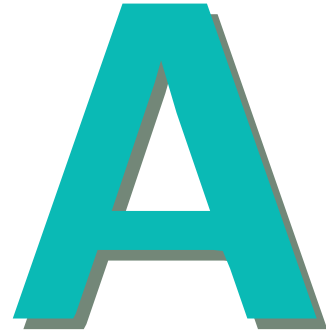
Appendix: Additional measurement information

A.1 Nanowire diameters

For the device generations featuring only Josephson junctions, no SEM images were taken of the nanowires or of the devices prior to transport measurements (as described in 3.2.4) to prevent any related damage. Due to the peculiarities of such measurements, devices frequently burn during electrostatic gating, which unfortunately happend as well with the Nb and the TiVTiAl device batch presented in Sections 6.1 and 6.2. However, during the numerous preceding fabrication and measurement cycles, expertise was acquired to consistently pick nanowires with diameters between 30 nm and 40 nm for device fabrication.

The missing device images are not a significant drawback, because the nanowire diameter is not precisely measureable with scanning electron microscopy, due to the following factors. Firstly, the accuracy of the image itself is of the order of several nanometers. Secondly, the native oxide of the nanowires is approximately 5 nm thick (Section 5) and thirdly, the finite penetration depth of the surface state is to be taken into account [2]. Lastly, the thickness of a nanowire

cannot be inferred from an SEM image, and the Josephson junction electrodes are too narrow to permit a sufficiently precise atomic force microscopy measurement in between. In that sense, a better measurement is made with AB-like oscillations which reveal the cross-sectional area through their periodicity in magnetic field. If available, this information is made use of in the data intepretation.

In the case of Device 1, a diameter of 30 nm was assumed. In the data analysis, this value is used for the estimation of the expected periodicity of a Fraunhofer pattern, and no usable AB-like oscillation data could be recorded. Choosing the lowest possible nanowire diameter yields the highest possible periodicity and therefore loosens the condition for a possible Fraunhofer pattern, which makes the hypothesis absence of Fraunhofer only harder to prove.

In the case of Device 2, a diameter of 30 nm was assumed because it is consistent with the magnetoresistance measurements in Section 6.2.3, showing probable signatures of AB-like oscillations of a periodicity of approximately 6 T and overlaid AAS oscillations of half the periodicity.

A.2 TRANSITION TEMPERATURE OF NB LEADS

The measurement of Device 1 included also four other similar devices with Nb Josephson junctions on $(Bi_{1-x}Sb_x)_2Te_3$ nanowires, two of which had a broken contact lead. Thus, one Nb lead had to be measured in series with each of these devices, which makes the superconducting Nb transition visible in the resitance curves. Figure A.1 shows all five R-T cooldown curves. The curve of Device 1 (green) is labelled as well as the Devices with a missing lead (red and purple). The Nb transition occurs at

$$T_{C,Nb,leads} = 8.0\,K, \tag{A.1}$$

which was used for the estimation of the superconducting gap of the Nb leads for the Nb device data analysis, used in Equation 6.1 and Sections 6.1.2 and 6.3.

A.3 DEVICE 1
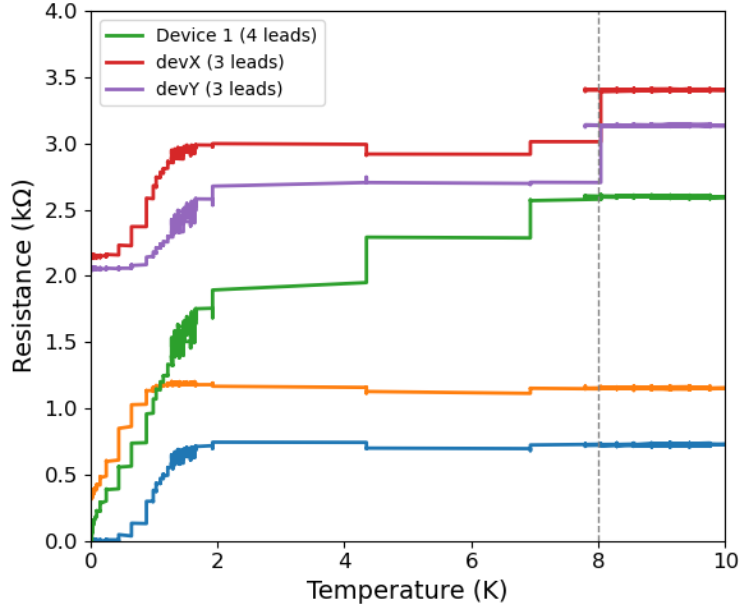
Figure A.1: ***Device 1: Cooldown measurement of multiple $(Bi_{1-x}Sb_x)_2Te_3$ nanowire Josephson junction devices.*** *Devices 1b, 1c, and 1d are connected through 3 leads only, meaning that the voltage measurement includes one current carrying lead, which is why the superconducting transition of the Nb leads can be seen in the measurement, occuring at $T_{C,Nb,leads} = 8.1\,K$.*

A.3.1 DIFFERENTIAL CONDUCTANCE AND TRANSPARENCY ERROR

Figure A.2 shows the differential conductance of Device 1, calculated by taking the derivative of the I-V data (shown in Figure 6.3) with respect to voltage. It can be seen, that the choice of 900 µV for the onset of the linear regime is reasonable, since the curve shows a visible kink between a negative slope and a horizontal regime. Additionally, the half and the third of this voltage are marked with grey arrows on top of the curve, coinciding with two humps which are possible weak signatures of multiple Andreev reflections. Not much shall be concluded from that, but their presence supports the estimate of $2\Delta_{induced} = 900\,\mu eV$ within the limitations of their faint appearance, which is also consistent with the estimated transparency of only 0.547.

The brisk up and down turn of the curve within $50 - 70\,\mu V$ is of unknown

origin. This type of features occasionally show up in such measurements and are usually attributed to Josephson self-radiation. Calculating the respective wavelength with the Josephson constant yields $\lambda \approx 8 - 12\,\text{mm}$. This matches the edge lengths of the device substrate, roughly corresponds to the diameter of four rods within the sample space and lies close to the thickness of the sample carrier.
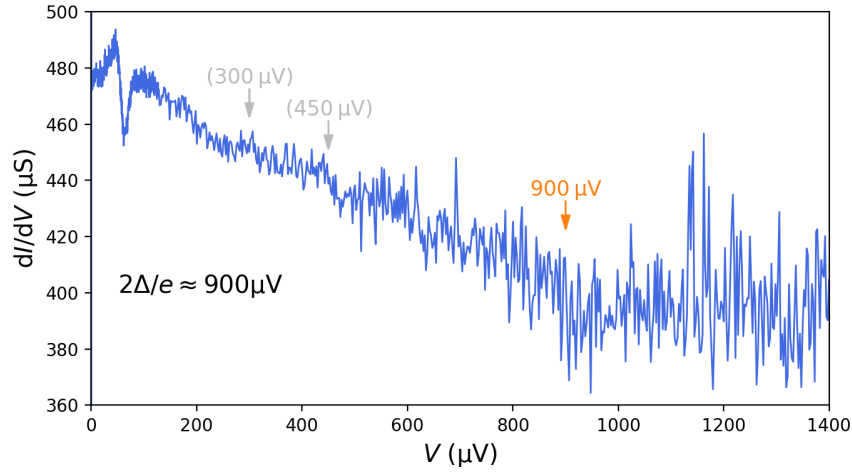
Figure A.2: **Device 1: Differential conductance.** *Differential conductance as a function of bias voltage. The data is calculated from differential resistance via integration and taking the derivative with respect to voltage. Above 900 µV the curve is approximately constant, hence $\Delta_{\text{induced}} \approx 450\,\text{µeV}$. The half and a third (grey arrows) of this voltage coincide with faint humps which could be weak multiple Andreev reflection signatures.*

To estimate the error margin of the calculated transparency, it has been calculated with a 10 % variation of $2\Delta_{\text{induced}} = 810\,\text{µV}, 900\,\text{µV}, 990\,\text{µV}$, to account for the possible error in choosing the linear onset of the I-V curve. The resulting transparencies amount to 0.5376, 0.5463 and 0.5566, averaging to 0.5468 with a min-max error of 0.0095, hence $T = 0.547 \pm 0.010$. The resulting error margins for the barrier height Z and the fraction $\frac{e I_{\text{exc}} R_{\text{N}}}{\Delta_{\text{induced}}}$ are included in the text Section 6.1.2.

For the subsequent devices, the error margin is not specified further, because the transparencies are of similar magnitude and the error calculation has shown to yield no qualitative difference of the transparency at such moderate values.

Bibliography

[1] F. Münning, O. Breunig, H. F. Legg, S. Roitsch, D. Fan, M. Rößler, A. Rosch, and Y. Ando, "Quantum confinement of the Dirac surface states in topological-insulator nanowires", Nature Communications **12**, 10 . 1038 / s41467 – 021 – 21230 – 3 (2021) 10 . 1038/s41467 – 021 – 21230 – 3 (cit. on pp. 3–4, 65, 92, 102, 109).

[2] F. Münning, O. Breunig, H. F. Legg, S. Roitsch, D. Fan, M. Rößler, A. Rosch, and Y. Ando, "Supplementary Information for "Quantum confinement of the Dirac surface states in topological-insulator nanowires"", Nature Communications **12**, 10 . 1038/s41467 – 021 – 21230 – 3 (2021) 10 . 1038/s41467 – 021 – 21230 – 3 (cit. on pp. 97, 102, 125).

[3] A Cook and M Franz, "Majorana fermions in a topological-insulator nanowire proximity-coupled to an s -wave superconductor", **201105**, 1–4 (2011) 10 . 1103/PhysRevB.84.201105 (cit. on pp. 1, 9, 18, 67).

[4]Y. Ando, "Topological insulator materials", J. Phys. Soc. Jpn. **82**, `10.7566/JPSJ.82.102001` (2013) `10.7566/JPSJ.82.102001` (cit. on pp. 1–2, 5–6, 17, 51–52, 63).

[5]C. W. J. Beenakker, "Search for Majorana Fermions in Superconductors", Annual Review of Condensed Matter Physics **4**, 113–136 (2013) `10.1146/annurev-conmatphys-030212-184337` (cit. on pp. 1, 17).

[6]J. Alicea, "New directions in the pursuit of Majorana fermions in solid state systems", Reports on Progress in Physics **75**, 76501 (2012) `10.1088/0034-4885/75/7/076501` (cit. on pp. 1, 5, 17).

[7]S. D. Sarma, M. Freedman, and C. Nayak, "Majorana zero modes and topological quantum computation", npj Quantum Information **1**, `10.1038/NPJQI.2015.1` (2015) `10.1038/NPJQI.2015.1` (cit. on p. 1).

[8]R. Aguado, "Majorana quasiparticles in condensed matter", Rivista del Nuovo Cimento **40**, 523–593 (2017) `10.1393/ncr/i2017-10141-9` (cit. on p. 1).

[9]V. Mourik, K. Zuo, S. M. Frolov, S. R. Plissard, E. P. Bakkers, and L. P. Kouwenhoven, "Signatures of majorana fermions in hybrid superconductor-semiconductor nanowire devices", Science **336**, 1003–1007 (2012) `10.1126/science.1222360` (cit. on p. 1).

[10]A. M. Cook, M. M. Vazifeh, and M. Franz, "Stability of Majorana fermions in proximity-coupled topological insulator nanowires", Physical Review B - Condensed Matter and Materials Physics **86**, 1–17 (2012) `10.1103/PhysRevB.86.155431` (cit. on pp. 1, 17–18).

[11]J. R. Powell, "The quantum limit to Moore's law", Proceedings of the IEEE **96**, 1247–1248 (2008) `10.1109/JPROC.2008.925411` (cit. on p. 2).

[12]J. Wu, Y.-L. Shen, K. Reinhardt, H. Szu, and B. Dong, "A Nanotechnology Enhancement to Moore's Law", Applied Computational Intelligence and Soft Computing **2013**, 1–13 (2013) `10.1155/2013/426962` (cit. on p. 2).

[13]T. Hoefler, T. Häner, and M. Troyer, "Disentangling Hype from Practicality: On Realistically Achieving Quantum Advantage", Communications of the ACM **66**, 82–87 (2023) `10.1145/3571725` (cit. on p. 2).

[14]M. Z. Hasan and C. L. Kane, "Colloquium: Topological insulators", Reviews of Modern Physics **82**, 3045–3067 (2010) `10.1103/RevModPhys.82.3045` (cit. on pp. 2, 5, 17).

[15]J. Alicea, Y. Oreg, G. Refael, F. Von Oppen, and M. P. Fisher, "Non-Abelian statistics and topological quantum information processing in 1D wire networks", Nature Physics **7**, 412–417 (2011) `10.1038/nphys1915` (cit. on p. 2).

[16]O. Breunig and Y. Ando, "Opportunities in topological insulator devices", Nature Reviews Physics **4**, 184–193 (2022) `10.1038/s42254-021-00402-6` (cit. on pp. 2, 5).

[17]M. Rößler, D. Fan, F. Münning, H. F. Legg, A. Bliesener, G. Lippertz, A. Uday, R. Yazdanpanah, J. Feng, A. A. Taskin, and Y. Ando, "Top-Down Fabrication of Bulk-Insulating Topological Insulator Nanowires for Quantum Devices", Nano Letters **23**, 2846–2853 (2023) `10.1021/acs.nanolett.3c00169` (cit. on pp. 2–3, 5, 11, 22, 110).

[18]M. Rößler, "Development and Electronic Phenomena of Etched Bulk-Insulating Topological Insulator Nanowires", PhD thesis (University of Cologne, 2023) (cit. on pp. 2–3, 22, 97).

[19]H. F. Legg, M. Rößler, F. Münning, D. Fan, O. Breunig, A. Bliesener, G. Lippertz, A. Uday, A. A. Taskin, D. Loss, J. Klinovaja, and Y. Ando, "Giant magnetochiral anisotropy from quantum-confined surface states of topological insulator nanowires", Nature Nanotechnology **17**, 696–700 (2022) `10.1038/s41565-022-01124-1` (cit. on pp. 2, 5).

[20]M. Bai, X.-K. Wei, J. Feng, M. Luysberg, A. Bliesener, G. Lippertz, A. Uday, A. A. Taskin, J. Mayer, and Y. Ando, "Proximity-induced superconductivity in $(Bi_{1-x}Sb_x)_2Te_3$ topological-insulator nanowires", Communications Materials **3**, 20 (2022) `10.1038/s43246-022-00242-6` (cit. on pp. 2–3).

[21]P. Schüffelgen, D. Rosenbach, C. Li, T. W. Schmitt, M. Schleenvoigt, A. R. Jalil, S. Schmitt, J. Kölzer, M. Wang, B. Bennemann, U. Parlak, L. Kibkalo, S. Trellenkamp, T. Grap, D. Meertens, M. Luysberg, G. Mussler, E. Berenschot, N. Tas, A. A. Golubov, A. Brinkman, T. Schäpers, and D. Grützmacher, "Selec-

tive area growth and stencil lithography for in situ fabricated quantum devices", Nature Nanotechnology **14**, 825–831 (2019) 10.1038/s41565-019-0506-y (cit. on pp. 2, 51).

[22]D. Rosenbach, N. Oellers, A. R. Jalil, M. Mikulics, J. Kölzer, E. Zimmermann, G. Mussler, S. Bunte, D. Grützmacher, H. Lüth, and T. Schäpers, "Quantum Transport in Topological Surface States of Selectively Grown Bi2Te3 Nanoribbons", Advanced Electronic Materials **6**, 2000205 (2020) 10.1002/aelm.202000205 (cit. on pp. 2, 11).

[23]D. Rosenbach, T. W. Schmitt, P. Schüffelgen, M. P. Stehno, C. Li, M. Schleenvoigt, A. R. Jalil, G. Mussler, E. Neumann, S. Trellenkamp, A. A. Golubov, A. Brinkman, D. Grützmacher, and T. Schäpers, "Reappearance of first Shapiro step in narrow topological Josephson junctions", Science Advances **7**, 1–10 (2021) 10.1126/sciadv.abf1854 (cit. on pp. 2–3, 22, 51, 99, 101).

[24]D. Rosenbach, K. Moors, A. R. Jalil, J. Kölzer, E. Zimmermann, J. Schubert, S. Karimzadah, G. Mussler, P. Schüffelgen, D. Grützmacher, H. Lüth, and T. Schäpers, "Gate-induced decoupling of surface and bulk state properties in selectively-deposited Bi2Te3 nanoribbons", SciPost Physics Core **5**, 1–18 (2022) 10.21468/SciPostPhysCore.5.1.017 (cit. on pp. 2, 11).

[25]H. Peng, K. Lai, D. Kong, S. Meister, Y. Chen, X.-L. Qi, S.-C. Zhang, Z.-X. Shen, and Y. Cui, "Aharonov-Bohm interference in topological insulator nanoribbons", Nat. Mater. **9**, 225 (2009) 10.1038/nmat2609 (cit. on p. 2).

[26]S. S. Hong, J. J. Cha, D. Kong, and Y. Cui, "Ultra-low carrier concentration and surface-dominant transport in antimony-doped Bi2Se3 topological insulator nanoribbons", Nature Communications **3**, 757 (2012) 10.1038/ncomms1771 (cit. on pp. 2, 51).

[27]B. Hamdou, J. Gooth, A. Dorn, E. Pippel, and K. Nielsch, "Surface state dominated transport in topological insulator Bi 2Te3 nanowires", Applied Physics Letters **103**, 10.1063/1.4829748 (2013) 10.1063/1.4829748 (cit. on pp. 2, 11, 51, 97).

[28]S. S. Hong, Y. Zhang, J. J. Cha, X.-L. Qi, and Y. Cui, "One-dimensional helical transport in topological insulator nanowire interferometers", Nano Lett. **14**, 2815–2821 (2014) 10.1021/nl500822g (cit. on p. 2).

[29]L. A. Jauregui, M. T. Pettes, L. P. Rokhinson, L. Shi, and Y. P. Chen, "Magnetic field-induced helical mode and topological transitions in a topological insulator nanoribbon", Nature Nanotechnology **11**, 345–351 (2016) 10.1038/nnano.2015.293 (cit. on pp. 2, 11).

[30]D. Van Delft and P. Kes, "The discovery of superconductivity", Europhysics News **42**, 21–25 (2011) 10.1051/epn/2011104 (cit. on p. 2).

[31]V. Kozhevnikov, *Meissner Effect: History of Development and Novel Aspects*, Vol. 34, 8 (Springer US, 2021), pp. 1979–2009, 10.1007/s10948-021-05925-8 (cit. on p. 2).

[32]T. M. Klapwijk, "Proximity Effect From an Andreev Perspective", Journal of Superconductivity **17**, 593–611 (2004) 10.1007/s10948-004-0773-0 (cit. on pp. 2, 16).

[33]M. Bai, F. Yang, M. Luysberg, J. Feng, A. Bliesener, G. Lippertz, A. A. Taskin, J. Mayer, and Y. Ando, "Novel self-epitaxy for inducing superconductivity in the topological insulator $(Bi_{1-x}Sb_x)_2Te_3$", Physical Review Materials **4**, 94801 (2020) 10.1103/PhysRevMaterials.4.094801 (cit. on p. 3).

[34]S. Ghatak, O. Breunig, F. Yang, Z. Wang, A. A. Taskin, and Y. Ando, "Anomalous Fraunhofer Patterns in Gated Josephson Junctions Based on the Bulk-Insulating Topological Insulator BiSbTeSe2", Nano Letters **18**, 5124–5131 (2018) 10.1021/acs.nanolett.8b02029 (cit. on pp. 3, 18, 21, 99, 110).

[35]N. Zapata, "Fabrication and characterization of Josephson junctions on topological insulating nanowires", PhD thesis (University of Cologne, 2021) (cit. on pp. 3, 94, 97).

[36]A. P. Surendran, D. Montemurro, G. Kunakova, X. Palermo, K. Niherysh, E. Trabaldo, D. S. Golubev, J. Andzane, D. Erts, F. Lombardi, and T. Bauch, "Current-phase relation of a short multi-mode Bi2Se3 topological insulator

nanoribbon Josephson junction with ballistic transport modes", Superconductor Science and Technology **36**, 64003 (2023) `10.1088/1361-6668/accf40` (cit. on p. 3).

[37] B. Bhattacharyya, V. P. Awana, T. D. Senguttuvan, V. N. Ojha, and S. Husale, "Proximity-induced supercurrent through topological insulator based nanowires for quantum computation studies", Scientific Reports **8**, 2–13 (2018) `10.1038/s41598-018-35424-1` (cit. on pp. 3, 94, 110).

[38] S. Charpentier, L. Galletti, G. Kunakova, R. Arpaia, Y. Song, R. Baghdadi, S. M. Wang, A. Kalaboukhov, E. Olsson, F. Tafuri, D. Golubev, J. Linder, T. Bauch, and F. Lombardi, "Induced unconventional superconductivity on the surface states of Bi2Te3 topological insulator", Nature Communications **8**, 6–13 `10.1038/s41467-017-02069-z` (cit. on pp. 3, 97).

[39] M. Sato and Y. Ando, "Topological superconductors: A review", Reports on Progress in Physics **80**, `10.1088/1361-6633/aa6ac7` (2017) `10.1088/1361-6633/aa6ac7` (cit. on p. 3).

[40] M. Leijnse and K. Flensberg, "Introduction to topological superconductivity and Majorana fermions", Semiconductor Science and Technology **27**, 124003 (2012) `10.1088/0268-1242/27/12/124003` (cit. on pp. 5, 17).

[41] J. H. Bardarson and R. Ilan, "Transport in Topological Insulator Nanowires", in *Springer series in solid-state sciences*, Vol. 190 (2019), pp. 93–114, `10.1007/978-3-319-76388-0_4` (cit. on p. 5).

[42] L. Fu, C. L. Kane, and E. J. Mele, "Topological Insulators in Three Dimensions", Physical Review Letters **98**, 106803 (2007) `10.1103/PhysRevLett.98.106803` (cit. on pp. 5–6).

[43] Y Xia, D Qian, D Hsieh, L Wray, A Pal, H Lin, A Bansil, D Grauer, Y. S. Hor, R. J. Cava, and M. Z. Hasan, "Observation of a large-gap topological-insulator class with a single Dirac cone on the surface", Nature Physics **5**, 398–402 (2009) `10.1038/nphys1274` (cit. on pp. 5, 50).

[44] H. F. Legg, D. Loss, and J. Klinovaja, "Metallization and proximity superconductivity in topological insulator nanowires", Phys. Rev. B **105**, 155413 (2022) `10.1103/PhysRevB.105.155413` (cit. on pp. 5, 22).

[45] S.-c. Zhang, "Topological states of quantum matter", Physics **1**, `10.1103/physics.1.6` (2008) `10.1103/physics.1.6` (cit. on p. 6).

[46] L. Fu and C. L. Kane, "Topological insulators with inversion symmetry", Physical Review B - Condensed Matter and Materials Physics **76**, 1–17 (2007) `10.1103/PhysRevB.76.045302` (cit. on pp. 6, 11, 49).

[47] J. H. Bardarson, P. W. Brouwer, and J. E. Moore, "Aharonov-Bohm oscillations in disordered topological insulator nanowires", Physical Review Letters **105**, 156803 (2010) `10.1103/PhysRevLett.105.156803` (cit. on p. 8).

[48] S. Washburn and R. A. Webb, "Aharonov-Bohm effect in normal metal quantum coherence and transport", Advances in Physics **35**, 375–422 (1986) `10.1080/00018738600101921` (cit. on p. 8).

[49] H. Peng, K. Lai, D. Kong, S. Meister, Y. Chen, X.-L. Qi, S.-C. Zhang, Z.-X. Shen, and Y. Cui, "Aharonov–Bohm interference in topological insulator nanoribbons", Nature Materials **9**, 225–229 (2010) `10.1038/nmat2609` (cit. on pp. 11, 51).

[50] S. Cho, B. Dellabetta, R. Zhong, J. Schneeloch, T. Liu, G. Gu, M. J. Gilbert, and N. Mason, "Aharonov-Bohm oscillations in a quasi-ballistic three-dimensional topological insulator nanowire", Nature Communications **6**, 1–5 (2015) `10.1038/ncomms8634` (cit. on pp. 11, 51, 97).

[51] T.-H. Hwang, H.-S. Kim, Y. Hou, D. Yu, and Y.-J. Doh, "Gate-Modulated Quantum Interference Oscillations in Sb-Doped Bi2Se3 Topological Insulator Nanoribbon", Journal of the Korean Physical Society **77**, 797–801 (2020) `10.3938/jkps.77.797` (cit. on p. 11).

[52] H.-S. Kim, T.-H. Hwang, N.-H. Kim, Y. Hou, D. Yu, H.-S. Sim, and Y.-J. Doh, "Adjustable Quantum Interference Oscillations in Sb-Doped Bi2Se3 Topological Insulator Nanoribbons", ACS Nano **14**, 14118–14125 (2020) `10.1021/acsnano.0c06892` (cit. on p. 11).

[53] J. Ziegler, R. Kozlovsky, C. Gorini, M. H. Liu, S. Weishäupl, H. Maier, R. Fischer, D. A. Kozlov, Z. D. Kvon, N. Mikhailov, S. A. Dvoretsky, K. Richter, and D. Weiss, "Probing spin helical surface states in topological HgTe nanowires", Physical Review B **97**, 1–12 (2018) 10.1103/PhysRevB.97.035157 (cit. on p. 11).

[54] S. Hikami, A. I. Larkin, and Y. Nagaoka, "Spin-Orbit Interaction and Magnetoresistance in the Two Dimensional Random System", Progress of Theoretical Physics **63**, 707–710 (1980) 10.1143/ptp.63.707 (cit. on p. 11).

[55] H.-Z. Lu and S.-Q. Shen, "Weak localization and weak anti-localization in topological insulators", Spintronics VII **9167**, 91672E (2014) 10.1117/12.2063426 (cit. on p. 11).

[56] J Chen, H. J. Qin, F Yang, J Liu, T Guan, F. M. Qu, G. H. Zhang, J. R. Shi, X. C. Xie, C. L. Yang, K. H. Wu, Y. Q. Li, and L Lu, "Gate-Voltage Control of Chemical Potential and Weak Antilocalization in Bi_2Se_3", **176602**, 1–4 (2010) 10.1103/PhysRevLett.105.176602 (cit. on p. 11).

[57] L. Bao, L. He, N. Meyer, X. Kou, P. Zhang, Z. G. Chen, A. V. Fedorov, J. Zou, T. M. Riedemann, T. A. Lograsso, K. L. Wang, G. Tuttle, and F. Xiu, "Weak anti-localization and quantum oscillations of surface states in topological insulator Bi_2Se_2Te", Scientific Reports **2**, 1–7 (2012) 10.1038/srep00726 (cit. on p. 11).

[58] K. L. Scipioni, Z. Wang, Y. Maximenko, F. Katmis, C. Steiner, and V. Madhavan, "Role of defects in the carrier-tunable topological-insulator (Bi1-xSbx) 2Te3 thin films", Physical Review B **97**, 10.1103/PhysRevB.97.125150 (2018) 10.1103/PhysRevB.97.125150 (cit. on pp. 12, 97).

[59] H. Kamerlingh Onnes, "The resistance of pure mercury at helium temperatures", KNAW Proceedings **13**, 1274 (1911) (cit. on p. 13).

[60] W. Meissner and R. Ochsenfeld, "Ein neuer Effekt bei Eintritt der Supraleitfähigkeit", Die Naturwissenschaften **21**, 787–788 (1933) 10.1007/BF01504252 (cit. on p. 13).

[61] J Bardeen, L. N. Cooper, and J. R. Schrieffer, "Theory of Superconductivity", Phys. Rev. **108**, 1175–1204 (1957) `10.1103/PhysRev.108.1175` (cit. on p. 13).

[62] M Tinkham, *Introduction to Superconductivity*, Dover Books on Physics Series (Dover Publications, 2004) (cit. on p. 14).

[63] L. Fu and C. L. Kane, "Superconducting Proximity Effect and Majorana Fermions at the Surface of a Topological Insulator", Phys. Rev. Lett. **100**, 96407 (2008) `10.1103/PhysRevLett.100.096407` (cit. on p. 16).

[64] A. Y. Kitaev, "Unpaired Majorana fermions in quantum wires", Physics-Uspekhi **44**, 131–136 (2001) `10.1070/1063-7869/44/10s/s29` (cit. on pp. 17–18).

[65] B. D. Josephson, "Possible new effects in superconductive tunnelling", Physics Letters **1**, 251–253 (1962) `10.1016/0031-9163(62)91369-0` (cit. on p. 19).

[66] R Gross, A Marx, and F Deppe, *Applied Superconductivity: Josephson Effect and Superconducting Electronics*, De Gruyter Textbook Series (Walter De Gruyter Incorporated, 2016) (cit. on pp. 19–21, 106).

[67] V. M. Krasnov, "Josephson junctions in a local inhomogeneous magnetic field", Physical Review B **101**, `10.1103/PhysRevB.101.144507` (2020) `10.1103/PhysRevB.101.144507` (cit. on p. 21).

[68] S. Hart, H. Ren, T. Wagner, P. Leubner, M. Mühlbauer, C. Brüne, H. Buhmann, L. W. Molenkamp, and A. Yacoby, "Induced superconductivity in the quantum spin Hall edge", Nature Physics **10**, 638–643 (2014) `10.1038/NPHYS3036` (cit. on p. 21).

[69] V. S. Pribiag, A. J. A. Beukman, F. Qu, M. C. Cassidy, C. Charpentier, W. Wegscheider, and L. P. Kouwenhoven, "Edge-mode superconductivity in a two-dimensional topological insulator", Nature Nanotechnology **10**, 593–597 (2015) `10.1038/nnano.2015.86` (cit. on p. 21).

[70] R. Gross, A. Marx, and F. Deppe, "Chapter 2 Physics of Josephson Junctions : The Zero Voltage State", Lecture Course (2013) (cit. on p. 21).

[71] J. G. Gijsbertsen, E. P. Houwman, J. Flokstra, and H. Rogalla, "Suppression of Ic and Fiske resonances in specially shaped Josephson junctions", Physica B: Physics of Condensed Matter **194-196**, 1705–1706 (1994) `10.1016/0921-4526(94)91352-8` (cit. on p. 21).

[72] J. C. Cuevas and F. S. Bergeret, "Magnetic interference patterns and vortices in diffusive SNS junctions", Physical Review Letters **99**, 1–4 (2007) `10.1103/PhysRevLett.99.217002` (cit. on p. 21).

[73] F. S. Bergeret and J. C. Cuevas, "The vortex state and Josephson critical current of a diffusive SNS junction", Journal of Low Temperature Physics **153**, 304–324 (2008) `10.1007/s10909-008-9826-2` (cit. on p. 21).

[74] L. Angers, F. Chiodi, G. Montambaux, M. Ferrier, S. Guéron, H. Bouchiat, and J. C. Cuevas, "Proximity dc squids in the long-junction limit", Physical Review B - Condensed Matter and Materials Physics **77**, 1–12 (2008) `10.1103/PhysRevB.77.165408` (cit. on p. 21).

[75] H. J. Suominen, J Danon, M Kjaergaard, K Flensberg, J Shabani, C. J. Palmstrom, F Nichele, and C. M. Marcus, "Anomalous Fraunhofer interference in epitaxial superconductor-semiconductor Josephson junctions", Phys. Rev. B **95**, 35307 (2017) `10.1103/PhysRevB.95.035307` (cit. on p. 22).

[76] P. Perla, H. A. Fonseka, P. Zellekens, R. Deacon, Y. Han, J. Kölzer, T. Mörstedt, B. Bennemann, A. Espiari, K. Ishibashi, D. Grützmacher, A. M. Sanchez, M. I. Lepsa, and T. Schäpers, "Fully in situ Nb/InAs-nanowire Josephson junctions by selective-area growth and shadow evaporation", Nanoscale Advances **3**, 1413–1421 (2021) `10.1039/d0na00999g` (cit. on p. 22).

[77] A. Murani, S. Sengupta, A. Kasumov, R. Deblock, C. Celle, J. P. Simonato, H. Bouchiat, and S. Gueron, "Long- To short-junction crossover and field-reentrant critical current in Al/Ag-nanowires/Al Josephson junctions", Physical Review B **102**, 1–9 (2020) `10.1103/PhysRevB.102.214506` (cit. on pp. 22, 112).

[78]B. K. Nikolić, J. K. Freericks, and P. Miller, "Equilibrium properties of double-screened dipole-barrier SINIS Josephson junctions", Physical Review B - Condensed Matter and Materials Physics **65**, 1–11 (2002) `10.1103/PhysRevB.65.064529` (cit. on pp. 22, 98, 110).

[79]M. Kjaergaard, H. J. Suominen, M. P. Nowak, A. R. Akhmerov, J. Shabani, C. J. Palmstrøm, F. Nichele, and C. M. Marcus, "Transparent Semiconductor-Superconductor Interface and Induced Gap in an Epitaxial Heterostructure Josephson Junction", Physical Review Applied **7**, 1–9 (2017) `10.1103/PhysRevApplied.7.034029` (cit. on pp. 22, 24).

[80]K Flensberg, J. B. Hansen, and M Octavio, "Subharmonic energy-gap structure in superconducting weak links", Phys. Rev. B **38**, 8707–8711 (1988) `10.1103/PhysRevB.38.8707` (cit. on pp. 24–25, 97).

[81]H. Kroemer, C. Nguyen, and E. L. Hu, "Electronic interactions at superconductor-semiconductor interfaces", Solid-State Electronics **37**, 1021–1025 (1994) `https://doi.org/10.1016/0038-1101(94)90349-2` (cit. on p. 24).

[82]G. Johansson, P. Samuelsson, and Å. Ingerman, "Full counting statistics of multiple andreev reflection", Physical Review Letters **91**, `10.1103/PhysRevLett.91.187002` (2003) `10.1103/PhysRevLett.91.187002` (cit. on pp. 24, 97).

[83]G. E. Blonder, M Tinkham, and T. M. Klapwijk, "Transition from metallic to tunneling regimes in superconducting microconstrictions: Excess current, charge imbalance, and supercurrent conversion", Phys. Rev. B **25**, 4515–4532 (1982) `10.1103/PhysRevB.25.4515` (cit. on p. 25).

[84]M Octavio, M Tinkham, G. E. Blonder, and T. M. Klapwijk, "Subharmonic energy-gap structure in superconducting constrictions", Phys. Rev. B **27**, 6739–6746 (1983) `10.1103/PhysRevB.27.6739` (cit. on p. 25).

[85]G. Niebler, G. Cuniberti, and T. Novotný, "Analytical calculation of the excess current in the Octavio–Tinkham–Blonder–Klapwijk theory", Superconductor Science and Technology **22**, 85016 (2009) `10.1088/0953-2048/22/8/085016` (cit. on p. 25).

[86]A. N. Cleland, "Superconductivity: Tunneling", in *Encyclopedia of condensed matter physics*, edited by F. Bassani, G. L. Liedl, and P. Wyder (Elsevier, Oxford, 2005), pp. 105–112, `10.1016/B0-12-369401-9/00704-X` (cit. on p. 27).

[87]R. F. Egerton, P Li, and M Malac, "Radiation damage in the TEM and SEM", Micron **35**, 399–409 (2004) `10.1016/j.micron.2004.02.003` (cit. on p. 37).

[88]Oxford Instruments, "Heliox Sorption Pumped 3 He Refrigerator", 1–23 (2013) (cit. on p. 43).

[89]Oxford Instruments, *Principles of dilution refrigeration*, 2015 (cit. on p. 44).

[90]H London, G. R. Clarke, and E Mendoza, "Osmotic Pressure of He^3 in Liquid He^4, with Proposals for a Refrigerator to Work below 1 K", Phys. Rev. **128**, 1992–2005 (1962) `10.1103/PhysRev.128.1992` (cit. on p. 45).

[91]V. P. P. K. N. Zinov'eva, "Phase diagram for liquid He3 - He4 solutions", J. Exptl. Theoret. Phys. **37**, 33–37 (1959) (cit. on p. 45).

[92]J. C. Wheatley, "Liquid He3, liquid mixtures of He3 and He4, and dilution refrigeration", J. Phys. Colloques **31**, 109–118 (1970) (cit. on p. 45).

[93]C. R. Cosens, "A balance-detector for alternating-current bridges", Proceedings of the Physical Society **46**, 818 (1934) `10.1088/0959-5309/46/6/310` (cit. on p. 46).

[94]D Hsieh, D Qian, L Wray, Y Xia, Y. S. Hor, R. J. Cava, and M. Z. Hasan, "A topological Dirac insulator in a quantum spin Hall phase", Nature **452**, 970–974 (2008) `10.1038/nature06843` (cit. on p. 49).

[95]H. Zhang, C.-X. Liu, X.-L. Qi, X. Dai, Z. Fang, and S.-C. Zhang, "Topological insulators in Bi2Se3, Bi2Te3 and Sb2Te3 with a single Dirac cone on the surface", Nature Physics **5**, 438–442 (2009) `10.1038/nphys1270` (cit. on p. 49).

[96]W. Zhang, R. Yu, H. J. Zhang, X. Dai, and Z. Fang, "First-principles studies of the three-dimensional strong topological insulators Bi2Te3, Bi2Se3and Sb 2Te3", New Journal of Physics **12**, 10.1088/1367-2630/12/6/065013 (2010) 10.1088/1367-2630/12/6/065013 (cit. on p. 50).

[97]Y. L. Chen, J. G. Analytis, J Chu, Z. K. Liu, S Mo, X. L. Qi, H. J. Zhang, D. H. Lu, X Dai, Z Fang, S. C. Zhang, I. R. Fisher, Z Hussain, and Z Shen, "Experimental Realization of a Three-Dimensional Topological Insulator, Bi2Te3", Science **325**, 178–181 (2009) 10.1126/`science.1173034` (cit. on p. 50).

[98]D Hsieh, Y Xia, D Qian, L Wray, J. H. Dil, F Meier, J Osterwalder, L Patthey, J. G. Checkelsky, N. P. Ong, A. V. Fedorov, H Lin, A Bansil, D Grauer, Y. S. Hor, R. J. Cava, and M. Z. Hasan, "A tunable topological insulator in the spin helical Dirac transport regime", Nature **460**, 1101–1105 (2009) 10.1038/`nature08234` (cit. on p. 50).

[99]M. Z. Hasan and J. E. Moore, "Three-Dimensional Topological Insulators", Annual Review of Condensed Matter Physics **2**, 55–78 (2011) 10.1146/`annurev-conmatphys-062910-140432` (cit. on p. 50).

[100]J. Zhang, C. Z. Chang, Z. Zhang, J. Wen, X. Feng, K. Li, M. Liu, K. He, L. Wang, X. Chen, Q. K. Xue, X. Ma, and Y. Wang, "Band structure engineering in $(Bi_{1-x}Sb_x)_2Te_3$ ternary topological insulators", Nature Communications **2**, 574 (2011) 10.1038/`ncomms1588` (cit. on pp. 51, 92).

[101]Z. Ren, A. A. Taskin, S. Sasaki, K. Segawa, and Y. Ando, "Observations of two-dimensional quantum oscillations and ambipolar transport in the topological insulator Bi2Se3 achieved by Cd doping", Physical Review B - Condensed Matter and Materials Physics **84**, 1–6 (2011) 10.1103/`PhysRevB.84.075316` (cit. on p. 51).

[102]Y. S. Hor, A Richardella, P Roushan, Y Xia, J. G. Checkelsky, A Yazdani, M. Z. Hasan, N. P. Ong, and R. J. Cava, "*p*-type B_2Se_3 for topological insulator and low-temperature thermoelectric applications", Phys. Rev. B **79**, 195208 (2009) 10.1103/`PhysRevB.79.195208` (cit. on p. 51).

[103]V. M. Pereira, C. N. Wu, L. H. Tjeng, and S. G. Altendorf, "Modulation of surface states in Sb2 Te3/ Bi2 Te3 topological insulator heterostructures: The crucial role of the first adlayers", Physical Review Materials **5**, 1–8 (2021) `10.1103/PhysRevMaterials.5.034201` (cit. on p. 51).

[104]K. Holtgrewe, C. Hogan, and S. Sanna, "Evolution of topological surface states following Sb layer adsorption on Bi_2Se_3", Materials **14**, 1–16 (2021) `10.3390/ ma14071763` (cit. on p. 51).

[105]A. A. Taskin, Z. Ren, S. Sasaki, K. Segawa, and Y. Ando, "Observation of Dirac Holes and Electrons in a Topological Insulator", Physical Review Letters **107**, 016801–016804 (2011) `10.1103/PhysRevLett.107.016801` (cit. on p. 51).

[106]A. Bliesener, "Molecular beam epitaxy growth of topological materials", PhD thesis (University of Cologne, 2020), `http://kups.ub.uni-koeln.de/id/ eprint/46896` (cit. on pp. 51, 92).

[107]A. A. Volykhov, J. Sánchez-Barriga, A. P. Sirotina, V. S. Neudachina, A. S. Frolov, E. A. Gerber, E. Y. Kataev, B. Senkovsky, N. O. Khmelevsky, A. Y. Aksenenko, N. V. Korobova, A. Knop-Gericke, O. Rader, and L. V. Yashina, "Rapid Surface Oxidation of Sb2Te3 as Indication for a Universal Trend in the Chemical Reactivity of Tetradymite Topological Insulators", Chemistry of Materials **28**, 8916–8923 (2016) `10.1021/acs.chemmater.6b03325` (cit. on p. 51).

[108]A. A. Volykhov, J. Sánchez-Barriga, M. Batuk, C. Callaert, J. Hadermann, A. P. Sirotina, V. S. Neudachina, A. I. Belova, N. V. Vladimirova, M. E. Tamm, N. O. Khmelevsky, C. Escudero, V. Pérez-Dieste, A. Knop-Gericke, and L. V. Yashina, "Can surface reactivity of mixed crystals be predicted from their counterparts? A case study of (Bi1-xSbx)2Te3 topological insulators", Journal of Materials Chemistry C **6**, 8941–8949 (2018) `10.1039/c8tc02235f` (cit. on p. 51).

[109] Z. Wang, R. L. J. Qiu, C. H. Lee, Z. Zhang, and X. P. A. Gao, "Ambipolar surface conduction in ternary topological insulator $Bi_2(Te_{1-x}Se_x)_3$ nanoribbons", ACS Nano **7**, 2126–2131 (2013) 10.1021/nn304684b (cit. on p. 52).

[110] Z. Ren, A. A. Taskin, S. Sasaki, K. Segawa, and Y. Ando, "Large bulk resistivity and surface quantum oscillations in the topological insulator Bi_2Te_2Se", Phys. Rev. B **82**, 241306 (2010) 10.1103/PhysRevB.82.241306 (cit. on p. 52).

[111] D. O. Scanlon, P. D. C. King, R. P. Singh, A de la Torre, S. M. Walker, G Balakrishnan, F Baumberger, and C. R. A. Catlow, "Controlling Bulk Conductivity in Topological Insulators: Key Role of Anti-Site Defects", Advanced Materials **24**, 2154–2158 (2012) 10.1002/adma.201200187 (cit. on p. 52).

[112] R. J. Cava, H. Ji, M. K. Fuccillo, Q. D. Gibson, and Y. S. Hor, "Crystal structure and chemistry of topological insulators", Journal of Materials Chemistry C **1**, 3176–3189 (2013) 10.1039/c3tc30186a (cit. on pp. 52, 63).

[113] L. V. Yashina, J. Sánchez-Barriga, M. R. Scholz, A. A. Volykhov, A. P. Sirotina, V. Neudachina S., M. E. Tamm, A. Varykhalov, D. Marchenko, G. Springholz, G. Bauer, A. Knop-Gericke, and O. Rader, "Negligible Surface Reactivity of Topological Insulators Bi_2Se_3 and Bi_2Te_3 towards Oxygen and Water", ACS Nano **7**, 5181–5191 (2013) 10.1021/nn400908b (cit. on p. 52).

[114] K. W. Kolasinski, "Catalytic growth of nanowires: Vapor-liquid-solid, vapor-solid-solid, solution-liquid-solid and solid-liquid-solid growth", Current Opinion in Solid State and Materials Science **10**, 182–191 (2006) 10.1016/j.cossms.2007.03.002 (cit. on p. 52).

[115] N. Wang, Y. Cai, and R. Q. Zhang, "Growth of nanowires", Materials Science and Engineering R: Reports **60**, 1–51 (2008) 10.1016/j.mser.2008.01.001 (cit. on p. 52).

[116] R. S. Wagner and W. C. Ellis, "VAPOR-LIQUID-SOLID MECHANISM OF SINGLE CRYSTAL GROWTH", Applied Physics Letters **4**, 89–90 (1964) 10.1063/1.1753975 (cit. on p. 52).

[117] Z Boncheva-Mladenova, A. S. Pashinkin, and A. V. Novoselova, "Investigation of the Evaporation of Antimony and Bismuth Tellurides and of Bismuth Selenide", in *Chemical bonds in solids: volume 3: x-ray and thermodynamic investigations*, edited by N. N. Sirota (Springer US, Boston, MA, 1972), pp. 151–158, `10.1007/978-1-4684-1686-2_26` (cit. on p. 62).

[118] Y. Blum, A. Tsukernik, M. Karpovski, and A. Palevski, "Critical current in Nb-Cu-Nb junctions with nonideal interfaces", Physical Review B - Condensed Matter and Materials Physics **70**, 1–4 (2004) `10.1103/PhysRevB.70.214501` (cit. on p. 94).

[119] J. Andzane, G. Kunakova, S. Charpentier, V. Hrkac, L. Kienle, M. Baitimirova, T. Bauch, F. Lombardi, and D. Erts, "Catalyst-free vapour-solid technique for deposition of Bi_2Te_3 and Bi_2Se_3 nanowires/nanobelts with topological insulator properties", Nanoscale **7**, 15935–15944 (2015) `10.1039/c5nr04574f` (cit. on p. 97).

[120] G. Kunakova, L. Galletti, S. Charpentier, J. Andzane, D. Erts, F. Léonard, C. D. Spataru, T. Bauch, and F. Lombardi, "Bulk-free topological insulator Bi_2Se_3 nanoribbons with magnetotransport signatures of dirac surface states", Nanoscale **10**, 19595–19602 (2018) `10.1039/C8NR05500A` (cit. on p. 97).

[121] G. Kunakova, T. Bauch, X. Palermo, M. Salvato, J. Andzane, D. Erts, and F. Lombardi, "High-Mobility Ambipolar Magnetotransport in Topological Insulator Bi2Se3 Nanoribbons", Physical Review Applied **16**, 1 (2021) `10.1103/PhysRevApplied.16.024038` (cit. on p. 97).

[122] F. Xiu, L. He, Y. Wang, L. Cheng, L.-T. Chang, M. Lang, G. Huang, X. Kou, Y. Zhou, X. Jiang, Z. Chen, J. Zou, A. Shailos, and K. L. Wang, "Manipulating surface states in topological insulator nanoribbons", Nat. Nanotechnol. **6**, 216–221 (2011) `10.1038/nnano.2011.19` (cit. on p. 97).

[123] J. L. Xia, F. Chen, P. Wiktor, D. K. Ferry, and N. J. Tao, "Effect of top dielectric medium on gate capacitance of graphene field effect transistors: Implications in mobility measurements and sensor applications", Nano Letters **10**, 5060–5064 (2010) `10.1021/nl103306a` (cit. on p. 97).

[124]Y. Cui, X. Duan, J. Hu, and C. M. Lieber, "Doping and electrical transport in silicon nanowires", Journal of Physical Chemistry B **104**, 5215–5216 (2000) 10.1021/jp0009305 (cit. on p. 97).

[125]Y. J. Doh, J. A. Van Dam, A. L. Roest, E. P. Bakkers, L. P. Kouwenhoven, and S. De Franceschi, "Applied physics: Tunable supercurrent through semiconductor nanowires", Science **309**, 272–275 (2005) 10.1126/science.1113523 (cit. on pp. 97, 110).

[126]I. O. Kulik and A. N. Omel'yanchuk, *Contribution to the microscopic theory of the Josephson effect in superconducting bridges*, 1975 (cit. on pp. 98, 110).

[127]P. Dubos, H. Courtois, B. Pannetier, F. K. Wilhelm, A. D. Zaikin, and G. Schön, "Josephson critical current in a long mesoscopic S-N-S junction", Physical Review B - Condensed Matter and Materials Physics **63**, 1–5 (2001) 10.1103/PhysRevB.63.064502 (cit. on pp. 98, 110).

[128]J. P. Heida, "Josephson currents in two dimensional mesoscopic ballistic conductors", PhD thesis (University of Groningen, 1998), pp. 57–78 (cit. on pp. 98, 110).

[129]J. B. Oostinga, L. Maier, P. Schüffelgen, D. Knott, C. Ames, C. Brüne, G. Tkachov, H. Buhmann, and L. W. Molenkamp, "Josephson Supercurrent through the Topological Surface States of Strained Bulk HgTe", Phys. Rev. X **3**, 21007 (2013) 10.1103/PhysRevX.3.021007 (cit. on p. 99).

[130]I. N. Khlyustikov, "Surface Superconductivity of Vanadium", Journal of Experimental and Theoretical Physics **132**, 453–456 (2021) 10.1134/S1063776121030043 (cit. on p. 106).

[131]H. A. Nilsson, P. Samuelsson, P. Caroff, and H. Q. Xu, "Supercurrent and multiple Andreev reflections in an InSb nanowire Josephson junction", Nano Letters **12**, 228–233 (2012) 10.1021/nl203380w (cit. on pp. 110, 112).

[132]J. Tiira, E. Strambini, M. Amado, S. Roddaro, P. San-Jose, R. Aguado, F. S. Bergeret, D. Ercolani, L. Sorba, and F. Giazotto, "Magnetically-driven colossal supercurrent enhancement in InAs nanowire Josephson junctions", Nature Communications **8**, 1–9 (2017) 10.1038/ncomms14984 (cit. on p. 112).

[133]H. Courtois, M. Meschke, J. T. Peltonen, and J. P. Pekola, "Origin of hysteresis in a proximity josephson junction", Physical Review Letters **101**, 1–4 (2008) `10.1103/PhysRevLett.101.067002` (cit. on p. 112).

[134]S Guéron, H Pothier, N. O. Birge, D Esteve, and M. H. Devoret, "Superconducting Proximity Effect Probed on a Mesoscopic Length Scale", Physical Review Letters **77**, 3027–3028 (1996) `https://doi.org/10.1103/PhysRevLett.77.3025` (cit. on pp. 114, 116).

Erklärung zur Dissertation

Hiermit versichere ich an Eides statt, dass ich die vorliegende Dissertation selbstständig und ohne die Benutzung anderer als der angegebenen Hilfsmittel und Literatur angefertigt habe. Alle Stellen, die wörtlich oder sinngemäß aus veröffentlichten und nicht veröffentlichten Werken dem Wortlaut oder dem Sinn nach entnommen wurden, sind als solche kenntlich gemacht. Ich versichere an Eides statt, dass diese Dissertation noch keiner anderen Fakultät oder Universität zur Prüfung vorgelegen hat; dass sie - abgesehen von unten angegebenen Teilpublikationen und eingebundenen Artikeln und Manuskripten - noch nicht veröffentlicht worden ist sowie, dass ich eine Veröffentlichung der Dissertation vor Abschluss der Promotion nicht ohne Genehmigung des Promotionsausschusses vornehmen werde. Die Bestimmungen dieser Ordnung sind mir bekannt. Darüber hinaus erkläre ich hiermit, dass ich die Ordnung zur Sicherung guter wissenschaftlicher Praxis und zum Umgang mit wissenschaftlichem Fehlverhalten der Universität zu Köln gelesen und sie bei der Durchführung der Dissertation zugrundeliegenden Arbeiten und der schriftlich verfassten Dissertation beachtet habe und verpflichte mich hiermit, die dort genannten Vorgaben bei allen wissenschaftlichen Tätigkeiten zu beachten und umzusetzen. Ich versichere, dass die eingereichte elektronische Fassung der eingereichten Druckfassung vollständig entspricht.

Felix Münning
Köln, 05.02.2024

Teilpublikationen (*equal contributions):

F. Münning*, O. Breunig*, H. F. Legg*, S. Roitsch, D. Fan, M. Rößler, A. Rosch, and Y. Ando, "Quantum confinement of the Dirac surface states in topological-insulator nanowires", Nature Communications 12, 10.1038/s41467-021-21230-3